Development of Photothermal Optical Coherence Tomography for Retinal Imaging

By

Maryse Lapierre-Landry

Dissertation

Submitted to the Faculty of the

Graduate School of Vanderbilt University

in partial fulfillment of the requirements

for the degree of

DOCTOR OF PHILOSOPHY

in

Biomedical Engineering

August 31st 2018

Nashville, Tennessee

Approved by

Yuankai Tao, PhD

Melissa Skala, PhD

Craig Duvall, PhD

E. Duco Jansen, PhD

Rizia Bardhan, PhD

Brett Byram, PhD

ACKNOWLEGMENTS

Thank you to my advisor Dr. Skala for her support, her knowledge of the field, her numerous advices, and her time throughout the years. Under her mentorship I was able to make the most out of my years spent both at Vanderbilt University and the Morgridge Institute for Research.

Thank you to my committee members Dr. Tao, Dr. Byram, Dr. Jansen, Dr. Bardhan and Dr. Duvall for their complementary perspectives, numerous ideas and the many insightful conversations.

Thank you to my numerous collaborators and co-authors: Allison Huckenpahler, Dr. Joseph Carroll, Dr. Thomas Connor, Dr. Ross Collery, Andrew Gordon and Dr. John Penn without whom the work presented in this dissertation would not have been possible.

Thank you to the members of my lab, past and present, for making my time as a PhD student so enjoyable. Thank you to Dr. Jason Tucker-Schwartz for teaching me everything I needed to know about PT-OCT. Thank you to Daniel Gil for all the conversations, all the brainstorming sessions, and for always being there. Thank you to Tiffany, Peter, Liz, Joe, Amani, Rupsa and Kayvan for making Madison such an enjoyable place to be.

Thank you to Dr. Jing Xu for her advices and encouragements throughout the years. Without her words, I am not sure I would have applied to a PhD program in the first place.

Thank you to my parents for their constant support from the very first day I stepped into a physics lab and until now, eleven years later. *Merci pout tout.*

Thank you to my partner Steven for his support, his patience and his encouragements. Thank you for being by my side, every single day.

TABLE OF CONTENTS

LIST OF TABLES

Table

LIST OF FIGURES

Figure

CHAPTER 1

Introduction

1.1 Motivation

Imaging is an essential part of ophthalmic care, both at the preclinical and clinical level. In the clinic, different imaging tools are routinely used to diagnose eye conditions, monitor disease progression, evaluate treatment response and guide surgery. In the laboratory, *in vivo* imaging techniques are used to understand disease pathophysiology, identify early markers of diseases, and develop new therapies. Over the years, multiple techniques have been developed for both two- and three-dimensional imaging of the eye. White light fundus cameras are commonly used to look at morphological changes of the eye in 2D and to assess changes in vasculature (fluorescein or indocyanine green angiography)[1, 2]. Scanning laser ophthalmoscopy (SLO) similarly produces 2D images of the retina, including fluorescence and autofluorescence images (lipofuscin and melanin), and provides some depth-sectioning with the addition of a pinhole[3-5]. SLO can also be combined with adaptive optics (AO-SLO) to produce high resolution images of the photoreceptor mosaic[6, 7]. Whole-body three-dimensional imaging techniques, such as ultrasound imaging[8], photoacoustic imaging[9], computed tomography (CT) or magnetic resonance imaging (MRI)[10] are also used to image the eye. These tools provide greater imaging depth and can capture the whole eye and surrounding structures. However, whole-body techniques have a limited resolution and individual cellular layers of the retina are not distinguishable. As a result, images whole-body techniques cannot be compared directly to histology when studying disease progression.

Optical coherence tomography (OCT) fills the niche between high resolution, two-dimensional imaging techniques such as fundus and SLO, and whole-body techniques such as ultrasound and MRI. OCT is a non-invasive, three-dimensional, high-resolution (< 5μm axial resolution) technique that has become a standard-of-care for eye imaging[11-13]. OCT is sensitive to tissue backscattering and thus can distinguish between different tissue layers in the retina. The thickness of those layers can be measured and compared

to what is seen on histology[14]. Both layer integrity and thickness as seen on OCT can be related to different diseases states. In the clinic, OCT is used to screen, diagnose and monitor diseases such as age-related macular degeneration, macular hole or glaucoma, with more than 16 million OCT procedures in the US per year[13]. In the laboratory, OCT is used to understand how diseases affect the eye over time[15], and to evaluate new therapies *in vivo*. Commercial OCT systems are designed to enable imaging in patients but also in multiple animal eye models, such as mice and rabbits, which has resulted in OCT being widely used throughout the eye and vision research community.

The OCT signal is produced by changes in the refractive index of the tissue and thus provides structural information about the tissue. However, this signal does not provide functional or molecular contrast. Many OCT-based techniques have thus been developed to provide co-registered functional information, in addition to the structural information. OCT angiography (vasculature)[16] or OCT elastography (biomechanical properties)[17] for example, can be used in parallel to traditional OCT without the need for a separate instrument or to co-register images after acquisition. There is thus significant interest in developing new functional OCT modalities to add contrast to OCT images.

The goal of this dissertation is to develop photothermal OCT (PT-OCT)[18, 19] for retinal imaging. PT-OCT is a functional OCT technique that detects optical absorbers in the OCT field-of-view. An additional laser is coupled to the OCT system and the light from this laser creates a small temperature change in the sample after being absorbed. This temperature change then leads to tissue expansion and a change in the refractive index of the tissue, both of which are then detected as a shift in the OCT phase signal. PT-OCT has never been performed in the eye before, and no other clinical eye technique specifically detects optical absorbers. This work aims to 1) create a theoretical model of PT-OCT to improve image quality, 2) demonstrate PT-OCT for retinal imaging at the pre-clinical level in different animal models and using different contrast agents, and 3) highlight the potential of PT-OCT for clinical applications. PT-OCT can be a novel tool for researchers to detect both endogenous and exogenous absorbers in the eye, especially for those researchers who have already adopted OCT for their ophthalmic imaging needs.

1.2 Specific Aims

Aim 1: Assemble a comprehensive theoretical model of PT-OCT to predict signal intensity with depth. Existing theoretical models describing different parts of the photothermal heat generation and OCT signal detection were grouped to form a complete representation of photothermal signal generation, detection, and processing. The model predictions were validated experimentally in phantoms. The model was also used to create the PT-CLEAN algorithm to improve image quality and remove artifacts in *in vivo* PT-OCT images.

Aim 2: Image gold nanorods and melanin *in vivo* in animal eye models using PT-OCT. In a first study, PT-OCT was demonstrated for the first time for *in vivo* eye imaging. Images of gold nanorods in the eyes of black mice with neovascular lesions (a model of macular degeneration) were obtained. PT-OCT images of melanin in the mouse eye were also obtained and validated by comparing wild-type animals with albino animals. A follow-up study used PT-OCT to image melanin in the zebrafish eye, where light-driven melanosome translocation was observed. This Aim demonstrates the versatility of PT-OCT for pre-clinical *in vivo* imaging of the eye.

Aim 3: Increase contrast of the inner limiting membrane using PT-OCT and indocyanine green. During surgery, the inner limiting membrane (ILM) is often stained with indocyanine green (ICG) to increase contrast and facilitate peeling. Such procedure can be imaged with OCT to improve depth-perception. However, OCT does not have a contrast mechanism to detect ICG. In this study, PT-OCT sensitivity to sub-clinical concentrations of ICG was demonstrated using laser powers below the ANSI standards in phantoms. Additionally, an ILM-peel was performed and imaged with PT-OCT in *ex vivo* pig eyes following ICG staining as a proof of concept. This was the first time PT-OCT was performed using laser powers within clinically acceptable levels for the eye, and a first effort into translating PT-OCT toward the clinic.

1.3 Dissertation Outline

This dissertation has been organized in the following manner:

Chapter 1 consists of the motivation for the dissertation and an overview of the Specific Aims.

Chapter 2 provides background information on the topic of pre-clinical and clinical imaging in the eye with an overview of the different imaging techniques, and more specifically an overview of OCT, functional OCT techniques and PT-OCT.

Chapter 3 describes a theoretical model of PT-OCT and an algorithm to correct for phase accumulation and shadowing, two artifacts that are present in PT-OCT images. This work was validated experimentally and can be used as a tool to model different instruments, samples or imaging parameters. The algorithm described in this project was also used in a subsequent project (described in Chapter 5) to correct PT-OCT images acquired in the eye. This project was published in *Biomedical Optics Express* (2016)[20].

Chapter 4 contains a first demonstration of a pre-clinical application of PT-OCT in the eye: *in vivo* imaging of gold nanorods and melanin in the mouse eye. A laser-induced neovascularization lesion model was used and gold nanorods were injected systemically through the tail vein. The gold nanorods then accumulated in the neovascular lesion and imaged with PT-OCT. Signal from melanin was also detected in the retinal pigment epithelium. This study was the first demonstration of PT-OCT in the eye and was published in *Scientific Reports* (2017)[21].

Chapter 5 describes a second example of pre-clinical applications of PT-OCT in the eye and is a follow-up on the study presented in Chapter 4. A more robust validation of PT-OCT of melanin was performed in tyrosinase-mosaic zebrafish, where pigmented and non-pigmented areas of the retina are present within each eye. Intracellular pigment migration was also observed with PT-OCT by imaging light-driven melanosome translocation. This study demonstrates the potential of PT-OCT for quantitative

imaging of melanin in animal models such as the zebrafish. This study is to be published in *Translational Vision Science and Technology* (2018).

Chapter 6 describes a potential clinical application of PT-OCT: imaging the inner limiting membrane (ILM) after indocyanine green (ICG) staining. In this study, a range of ICG concentrations were used to evaluate the sensitivity of PT-OCT to this small molecule dye, using multiple photothermal laser powers in phantoms. An ILM stain was then performed in *ex vivo* pig eyes and imaged with PT-OCT to demonstrate this technique. This work was published in *Optics Letters* (2018)[22].

Chapter 7 contains concluding remarks, including a summary of the work presented in this dissertation, a discussion of future directions and a description of the scientific contributions of this work.

1.4 References

[1] H. Bartlett and F. Eperjesi, "Use of fundus imaging in quantification of age-related macular change," *Survey of ophthalmology,* vol. 52, no. 6, pp. 655-671, 2007.

[2] N. Panwar *et al.*, "Fundus photography in the 21st century—a review of recent technological advances and their implications for worldwide healthcare," *Telemedicine and e-Health,* vol. 22, no. 3, pp. 198-208, 2016.

[3] R. H. Webb, G. W. Hughes, and F. C. Delori, "Confocal scanning laser ophthalmoscope," *Applied optics,* vol. 26, no. 8, pp. 1492-1499, 1987.

[4] M. A. Mainster, G. T. Timberlake, R. H. Webb, and G. W. Hughes, "Scanning laser ophthalmoscopy: clinical applications," *Ophthalmology,* vol. 89, no. 7, pp. 852-857, 1982.

[5] C. N. Keilhauer and F. o. C. Delori, "Near-Infrared Autofluorescence Imaging of the Fundus: Visualization of Ocular Melanin," vol. 47, no. 8, pp. 3556-3564, 2006.

[6] A. Roorda, F. Romero-Borja, W. J. Donnelly III, H. Queener, T. J. Hebert, and M. C. Campbell, "Adaptive optics scanning laser ophthalmoscopy," *Optics express,* vol. 10, no. 9, pp. 405-412, 2002.

[7] D. Merino and P. Loza-Alvarez, "Adaptive optics scanning laser ophthalmoscope imaging: technology update," *Clinical ophthalmology (Auckland, NZ),* vol. 10, p. 743, 2016.

[8] B. A. Kilker, J. M. Holst, and B. Hoffmann, "Bedside ocular ultrasound in the emergency department," *European Journal of Emergency Medicine,* vol. 21, no. 4, pp. 246-253, 2014.

[9] S. Jiao *et al.*, "Photoacoustic ophthalmoscopy for in vivo retinal imaging," *Optics express,* vol. 18, no. 4, pp. 3967-3972, 2010.

[10] A. Simha, A. Irodi, and S. David, "Magnetic resonance imaging for the ophthalmologist: A primer," *Indian journal of ophthalmology,* vol. 60, no. 4, p. 301, 2012.

[11] M. R. Hee *et al.*, "Optical coherence tomography of the human retina," *Archives of ophthalmology,* vol. 113, no. 3, pp. 325-332, 1995.

[12] J. G. Fujimoto, C. Pitris, S. A. Boppart, and M. E. Brezinski, "Optical coherence tomography: an emerging technology for biomedical imaging and optical biopsy," *Neoplasia,* vol. 2, no. 1, pp. 9-25, 2000.

[13] J. Fujimoto and E. Swanson, "The development, commercialization, and impact of optical coherence tomography," *Investigative ophthalmology & visual science,* vol. 57, no. 9, pp. OCT1-OCT13, 2016.
[14] R. F. Spaide and C. A. Curcio, "Anatomical correlates to the bands seen in the outer retina by optical coherence tomography: literature review and model," *Retina,* vol. 31, no. 8, p. 1609, 2011.
[15] A. Giani, "In vivo evaluation of laser-induced choroidal neovascularization using spectral-domain optical coherence tomography," *Investigative ophthalmology visual science,* vol. 52, no. 6 SRC - GoogleScholar, pp. 3880-3887, 2011.
[16] S. S. Gao *et al.,* "Optical coherence tomography angiography," *Investigative ophthalmology & visual science,* vol. 57, no. 9, pp. OCT27-OCT36, 2016.
[17] S. Wang and K. V. Larin, "Optical coherence elastography for tissue characterization: a review," *Journal of biophotonics,* vol. 8, no. 4, pp. 279-302, 2015.
[18] D. C. Adler, S. W. Huang, R. Huber, and J. G. Fujimoto, "Photothermal detection of gold nanoparticles using phase-sensitive optical coherence tomography," *Optics Express,* vol. 16, no. 7 SRC - GoogleScholar, pp. 4376-4393, 2008.
[19] M. C. Skala, M. J. Crow, A. Wax, and J. A. Izatt, "Photothermal optical coherence tomography of epidermal growth factor receptor in live cells using immunotargeted gold nanospheres," *Nano letters,* vol. 8, no. 10, pp. 3461-3467, 2008.
[20] M. Lapierre-Landry, J. M. Tucker-Schwartz, and M. C. Skala, "Depth-resolved analytical model and correction algorithm for photothermal optical coherence tomography," *Biomedical optics express,* vol. 7, no. 7, pp. 2607-2622, 2016.
[21] M. Lapierre-Landry, A. Y. Gordon, J. S. Penn, and M. C. Skala, "In vivo photothermal optical coherence tomography of endogenous and exogenous contrast agents in the eye," *Scientific reports,* vol. 7, p. 9228, 2017.
[22] M. Lapierre-Landry, T. B. Connor, J. Carroll, Y. K. Tao, and M. C. Skala, "Photothermal optical coherence tomography of indocyanine green in ex vivo eyes," *Optics letters,* vol. 43, no. 11, pp. 2470-2473, 2018.

CHAPTER 2

Background

2.1 Clinical and pre-clinical imaging in the eye

2.1.1 Pre-clinical imaging for age-related macular degeneration research

Multiple animal eye models have been developed to study different developmental stages of the eye and study different diseases. More specifically vertebrate animals such as mice, rats, rabbits, pigs and primates have all been used in eye research[1-3]. Many genetically modified lines have also been developed, especially in mice[4]. Although many of these models were initially developed to be studied *ex vivo* with fixing and staining of the eye, researchers are now characterizing many of them using *in vivo* techniques, such as fundus imaging[5], scanning laser ophthalmoscopy (SLO)[6] and optical coherence tomography (OCT)[7]. Non-invasive imaging methods have many advantages such as repeated imaging over multiple time points in the same animal, and the ability to observe how different structures of the eye interact in a living system. This way, disease progression can be studied *in vivo* and over time in the same animal, which can lead to the identification of new disease markers. Additionally, animal imaging can be a step toward clinical translation, with the same imaging technologies used for both animals and patients[8]. Image interpretation can also be facilitated in patients based on previous work that compared images acquired in animals to corresponding histology[9]. Alternatively, new drug delivery vehicles can be dynamically evaluated based on the images acquired over time in animal models, which should lead to faster screening of new vehicles and faster clinical translation in the future.

Experiments involving animal models of age-related macular degenerations[10] are good examples of the different ways non-invasive imaging can play an important role in pre-clinical research. Age-related macular degeneration (AMD) is the most important cause of vision loss in adults above 65 years old in the US[11]. To this day, there is no cure for AMD and vision loss cannot be reversed, although anti-VEGF treatment can slow down or stop disease progression[12-14]. At early stages of the disease, AMD is usually characterized by changes in pigmentation and the presence of drusens. At later stages, “dry” AMD is

characterized by regions of atrophy of the retinal pigment epithelium (RPE) and photoreceptors, while in "wet" AMD neovascular lesions invade the retina from the choroid and lead to vascular leakage, scaring and vision loss[15]. The RPE, which is located between the photoreceptors and the choriocapillaris, is thought to play a central role in AMD[15]. In dry AMD, hyperpigmentation in the RPE (dysfunction in the RPE cells) followed by hypopigmentation (from the loss of RPE cells) could appear before dysfunction in the photoreceptors or choriocapillaris and could be predictive for the progression of the disease. In wet AMD, it is possible that loss of the choriocapillaris causes the RPE cells to become hypoxic and to produce angiogenic substances, resulting in neovascular lesions to form. Many animal models have been developed to reproduce different aspects of dry or wet AMD, including pigmentation changes, photoreceptor atrophy and neovascular lesions[10, 16]. *In vivo* imaging can be used to study those different facets of the disease while reducing the number of animals sacrificed for each experiment. For example, fundoscopy has been used to monitor changes in pigmentation in the RPE over time in a new mouse model of AMD[17] and to characterize drusen in rhesus macaques[18]. Fundoscopy, fundus fluorescein angiography and OCT have been used to optimize the size and placement of laser-induced neovascular lesions on the mouse retina to ensure uniform lesions across animals [19] and OCT has been used to characterize how neovascular lesions evolve over time in the same animal[20].

Novel imaging techniques are still being developed to study animal models, including models of AMD. For example, there are no standard *in vivo* techniques at the moment to quantify melanin levels in the eye, even though many pigmentation changes are observed in AMD. Melanin content can be quantified using spectrophotometry *in vitro*, but this is destructive for the cells[21]. Standard methods such as autofluorescence imaging have been used to look at melanin but are not quantitative[22]. Thus, there is a need for a non-invasive imaging technique able to quantify melanin *in vivo* to better study diseases such as AMD where pigmented cells are at the center of disease progression.

Additionally, there is a need for new imaging techniques to assess drug delivery strategies *in vivo*, especially for new drug delivery vectors such as metallic nanoparticles. Gold nanoparticles have been

investigated as a potential inhibitor to retinal neovascularization[23], however, there are still few studies discussing the pharmacodynamics of nanoparticles in the eye[24] and more are needed to really understand their potential. Standard techniques to detect gold nanoparticles in tissue are performed *ex situ* and are destructive to the sample. *In vivo* imaging techniques would allow for longitudinal studies in the same animal to observe the distribution of nanoparticles over time. Such technique would provide complimentary information to the current *ex vivo* methods.

In summary, *in vivo* imaging plays an essential role in pre-clinical ophthalmic research for its ability to non-invasively observe the healthy or diseased eye over time in multiple animal models, leading to a better understanding of eye pathologies such as AMD. Additionally, there is a need for new imaging technologies at the pre-clinical level. The development of an *in vivo* imaging technique that could detect and quantify natural pigments such as melanin, and novel drug carriers such as gold nanoparticles is at the center of the work presented in this dissertation.

2.1.2 Clinical eye imaging of age-related macular degeneration

In parallel to pre-clinical imaging, clinical imaging is used today in patients to screen and diagnose eye conditions, plan and monitor ocular surgeries and evaluate treatment response[25, 26]. The earliest ophthalmic imaging technique in the clinic was 35mm-film fundus photography and focused on documenting the appearance of diseases as they progressed[26]. In later iterations, fundus photography was combined with fluorescein or indocyanine green to provide images of the microvasculature of the retina and choroid[27]. However, fundus photography had a limited field-of-view and was qualitative in nature. The introduction of SLO in 1981 and OCT in 1991 enabled imaging with increased resolution and larger field-of-views. In the case of OCT, three-dimensional images could also be acquired. More recently, the introduction of digital fundus photography has made newer imaging systems more affordable and more portable, with images that can more easily be stored, shared and analyzed[28, 29].

Today, all of these techniques are part of the clinical imaging toolset and are used for screening and diagnosis of diseases such as AMD. Fundus imaging (35mm-film or digital) can be used in combination

with a manual grading system to diagnose early stages (age-related maculopathy) and late stages of the disease based on the presence, size and distribution of drusen, presence of hyperpigmentation, presence of geographic atrophy and presence of neovascular lesions[30]. In AMD, drusen are lipid deposits that form below the RPE and have a yellow appearance on fundus images (Fig. 2.1). Drusens do not seem to cause AMD, but presence of drusens is correlated with a patient's risk to develop the disease. For this reason, detecting the presence of drusen is central to screening and diagnosing early stages of AMD. To diagnose later stages (wet AMD in particular), fluorescein angiography or indocyanine green angiography are commonly used to detect the presence of neovascular lesions and leakage of the retinal and choroidal blood vessels[30]. Automatic grading systems are being developed to analyze digital fundus images, especially to quantify vessels and detect microaneurysms based on the angiography images, but also to detect and count drusen from fundus photographs[30].

Figure 2.1. Digital fundus photography of drusenoid lesions in rhesus macaques. Color photograph presented with grid template to estimate drusen size and area. Modified and reprinted from [18] under Creative Commons license (https://creativecommons.org/licenses/by/4.0/).

Similar to fundus photography, SLO is used to acquire two-dimensional images of the retina in order to detect and count drusen and detect macular edema[30, 31]. Contrary to fundus photography, SLO uses a laser as a light source. Thus, the wavelength of the laser can be chosen to optimize contrast. In the clinic, SLO uses a confocal pinhole to collect light from a specific retinal layer and greatly reduce the background signal. The increased sensitivity enables autofluorescence imaging of lipofuscin and melanin using SLO. In dry AMD, low melanin and lipofuscin fluorescence is seen in regions of geographic atrophy

(loss of RPE cells)[22], which facilitates an automated detection and segmentation of the zone of atrophy[32].

Developed in 1991 and first demonstrated in the eye in 1995, OCT is an imaging technique that can rapidly acquire high-resolution image volumes of the eye to see the different layers of the retina[33, 34]. OCT can be used to image drusen similarly to fundus and SLO. However, the depth-resolved images of OCT have enabled a more detailed characterization of the different types of drusen, depending on size and location within the retina[35]. OCT could also enable automated measurement of drusen diameter and volume, which are correlated with progression to later stages of AMD[36, 37]. Qualitative changes in pigmentation can also be seen as a change in layer reflectivity on OCT images at early stages of AMD. At later stages of the disease, geographic atrophy can also be seen as a change in RPE and choroid reflectivity. In wet AMD, neovascular lesions can be seen at different stages, from a detachment of the RPE, to accumulation of sub- and intra-retinal fluid, to hemorrhage[35]. For this reason, OCT is used (in combination with fluorescein angiography) to diagnose AMD, but also to monitor response to anti-VEGF injections (ranibizumab[14] and bevacizumab[13]) for patients with neovascular lesions. Those treatments were initially recommended as monthly injections, but using OCT the injection schedule can be personalized to each patient and based on the presence of macular edema, subretinal fluid, and/or pigment epithelial detachment[38]. As a result, anti-VEGF injections can be given less frequently, which has reduced health-care cost and improved the patient's quality of life[39].

In summary, clinical imaging in the eye is used to facilitate diagnosis, evaluate treatment response and possibly reduce the need for repeated treatment in AMD. However, changes in pigmentations are still difficult to quantify, and both hyper and hypo-pigmentation can be seen in early stages of the disease. A technique enabling specific and quantitative imaging of melanin could be an important clinical tool to manage this disease, and one such technique is presented in this dissertation.

2.1.3 Imaging for ocular surgery

In addition to disease screening and diagnosis, clinical imaging plays a crucial role in planning and guiding ocular surgery. Macular surgeries are sometimes recommended in cases of macular hole, epiretinal

membrane, and some forms of chronic diabetic macular edema[40]. A surgical white-light microscope is the standard imaging technique and allows surgeons to visualize the retina during the procedure. Dyes, such as indocyanine green or Trypan Blue can be used in combination with the microscope to improve the contrast of certain structures in the eye[41]. However, surgical microscopes provide limited depth-perception, and image quality can be degraded by the presence of opacities in the eye. Optical coherence tomography is now being added to the surgical suite, first to image the eye pre- and post-intervention, but also to guide surgery in real time as image acquisition speed increases and new OCT systems are developed[42]. OCT systems have been integrated to surgical microscopes to provide surgeons with both the white-light surgical microscope image and the OCT image (either 2D depth-resolved images, or 3D volumes)[43, 44]. OCT systems have also been integrated into hand-held probes that the surgeon can hold above the eye[45] or hand-held surgical tools that can be inserted into the eye[46]. OCT can thus be used to guide tissue-instrument interaction in three-dimensions and allow the surgeon to evaluate surgical results in real-time.

However, OCT lacks a contrast mechanism to detect the dyes that are commonly used during some surgeries. The development of an OCT-based imaging technique that could detect dyes such as indocyanine green and increase contrast during macular surgery is one of the projects presented in this dissertation.

2.2 Ophthalmic imaging modalities

Multiple imaging techniques have been developed to image the living eye. Some modalities, such as fundoscopy and SLO were developed specifically for the eye, while other modalities such as MRI and ultrasound imaging were adopted from other fields of medicine. Finally, modalities like OCT have first been introduced as an eye imaging technique but have since found applications in other fields such as cardiology and dermatology. Herein are described the most common imaging techniques to study the eye: fundus imaging, SLO, fluorescence and autofluorescence imaging, ultrasound, CT, MRI and OCT.

2.2.1 Fundus imaging

Fundus imaging produces a two-dimensional, *en face* color image of the retina where the optic nerve head, macula and major blood vessels can be seen. Most modern table-top fundus systems have a field-of-view of ~45° and do not require pupil dilation[29]. Fundus images can be recorded on 35mm-film or with a digital camera[26]. The basic components of a fundus system are a white light source to illuminate the retina, a central obscuration in the illumination path (annular aperture), an objective lens to form an image using the reflected light from the retina, a zoom lens to correct for the patient's refractive error, and a camera to detect the image[47]. This results in an annular illumination pattern at the pupil, a circular illumination pattern at the retina and a circular image detected at the camera. The annular illumination pattern at the pupil reduces the back reflection from the cornea and allow for a better detection of the reflected light from the retina. The illumination and collection paths can be combined with a beam splitter, or a mirror with a central hole to deflect the illumination path while letting through the collected light[47]. Most clinical fundus systems are "table-top" systems, but new handheld and smartphone-based fundus systems are being commercialized for use in the developing world[29].

2.2.2 Scanning laser ophthalmoscopy (SLO)

An alternative to fundus photography is scanning laser ophthalmoscopy (SLO)[48]. SLO also produces two-dimensional *en face* images of the retina. However, a pinhole can be used to selectively collect light from a specific layer of the retina (~300μm axial resolution[49]), which is not possible using a fundus camera[31]. Instead of a white light source, SLO uses a laser source focused onto a point and raster-scanned across the retina to build an image. This enables a small portion of the eye's pupil to be used for illumination, while the rest of the pupil is used for light collection[31]. In comparison, fundus imaging requires most of the pupil to be used for illumination (annular illumination pattern) with only the center of the pupil used for collection. As a result, SLO is performed with illumination powers that are much lower than those required for fundus imaging[48]. The wavelength of the laser source can be changed to highlight different structures of the eye or recreate a false colored image similar to fundus imaging. Additionally,

lens or mirrors can be added to the light path to focus the laser source at a wide range of angles, which has led to high resolution SLO systems with field-of-views up to 200°[50, 51].

Adaptive optics has been combined to SLO (AO-SLO) to correct for the aberration introduced by the cornea and lens and increase the imaging resolution[52, 53]. A sensor is used to detect the laser light returning from the retina and dynamically measure the optical aberrations. The wavefront sensing is then used to control a deformable mirror that corrects the aberrations for the light going to and from the retina. This way the illumination beam is tightly focused onto the retina, and the returning diffuse light is refocused as a compact spot as it reaches the confocal pinhole and the detector. As a result, the axial sectioning and lateral resolution have been improved from 5μm lateral and 300μm axial resolution for confocal SLO to 2.5μm lateral and 100μm axial resolution for AO-SLO[52]. With this improved resolution AO-SLO can image individual cone and rod photoreceptors at different depths in the living eye (Fig. 2.2), which is a significant improvement compared to SLO. However, because of the increased resolution, AO-SLO also has a limited field-of-view and individual images are usually a few degrees in size[54]. To circumvent this issue, many AO-SLO images can be acquired in a mosaic pattern to create larger field-of-view. However, this process requires eye tracking or eye fixation during image acquisition. While commercial "table-top" SLO systems are available for clinical use, AO-SLO systems are large in size and are still mostly considered research tools[55].

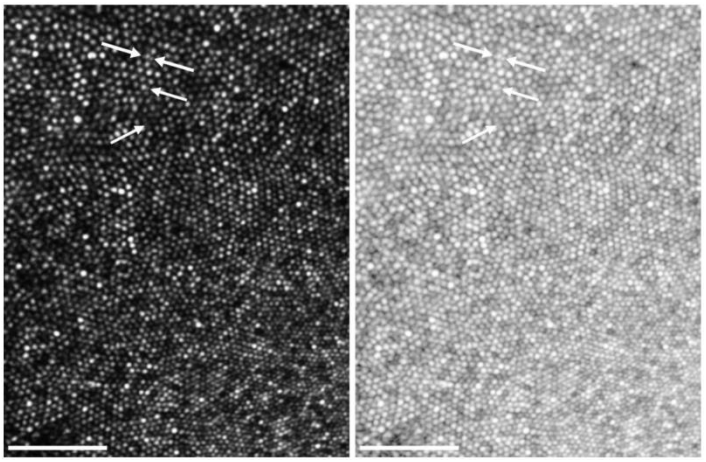

Figure 2.2. Adaptive-optics scanning laser ophthalmoscopy of the human photoreceptor mosaic. Image displayed with linear (left) and logarithmic (right) gray scale mapping. Arrows point to individual rod photoreceptors. Scale bar: 50μm. Reprinted with permission from [56]. Copyright 2011 Optical Society of America.

2.2.3 Fluorescence and autofluorescence imaging

Both fundus imaging and SLO have been adapted to perform fluorescence imaging[27]. For fluorescence fundus imaging, appropriate excitation and emission filters can be placed in front of the white light source and camera. For fluorescence SLO imaging, a laser of the appropriate excitation wavelength is chosen for illumination, and an emission filter is placed in front of the detector. Fluorescein angiography (excitation: 488nm, emission: 500-700nm) and indocyanine green angiography (excitation: 790nm, emission: >810nm) are the most common type of fluorescence imaging in the eye[57]. Repeated images are taken after intravenous injection of the fluorophore to assess retinal circulation and the integrity of the blood-retinal barrier[30]. SLO is sensitive to lower levels of emitted light than fundus photography, and thus lower concentrations of fluorophores can be used[58]. For the same reason, it is also possible to perform autofluorescence imaging with SLO since it is sensitive to the low signal intensity (Fig. 2.3). Two endogenous fluorophores are most commonly imaged with SLO: lipofuscin (excitation: 488nm, emission: >500nm) and melanin (excitation: 787nm, emission: >800nm)[22, 49]. In the case of lipofuscin and melanin, the choices of excitation and emission wavelengths are often dictated by the wavelengths used for fluorescein and indocyanine green because of the design of commercial instruments. SLO enables a qualitative assessment of both pigments and their distribution within the RPE can be indicative of different disease states[59].

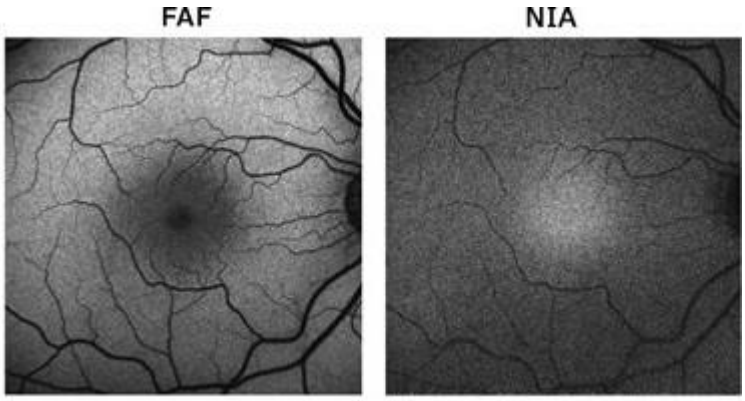

Figure 2.3. Fundus autofluorescence (FAF) and near-infrared autofluorescence (NIA) in the healthy human eye. FAF is performed with excitation at 488nm and detects lipofuscin autofluorescence. NIA is performed with excitation at 787nm and detects melanin autofluorescence. Reprinted with permission from Springer Nature Eye [59]. Copyright 2008.

2.2.4 Whole-body imaging techniques

Multiple whole-body techniques, such as ultrasound imaging and MRI are routinely used in the clinic to study other organs systems but have also been used to image the eye. Those techniques produce three-dimensional images and benefit from large imaging depth and field-of-view. Ultrasound imaging is used to image the cornea and anterior chamber with high resolution[60]. Ultrasound can also visualize structures deep into the eye, including the vitreous, retina and optic nerve[61]. However, lower ultrasound frequencies are used to achieve larger depths which results in images of a lower resolution. Contrary to the imaging modalities presented in previous sections, ultrasound imaging is not limited to optically transparent regions of the eye, and thus can image past structures such as the iris or sclera, or through opacities caused by cataracts or blood[60]. Photoacoustic ophthalmoscopy is an ultrasound-based modality with similar resolution and penetration depth to ultrasound imaging that uses a pulsed laser and an ultrasound transducer to image absorbers such as blood[62] and melanin[63] in the eye. However, photoacoustic ophthalmoscopy has yet to be demonstrated in the human eye and has the same resolution limits as ultrasound. Finally, both CT and MRI are whole-body techniques used when images of the whole eye, optic nerve, and surrounding structures are desired[64]. CT is more widely used in practice, but MRI has the advantage of not exposing the patient to ionizing radiation. Both modalities are used to look at eye trauma (due to fractures or penetrating objects), tumors, and pathologies that might affect the optic nerve.

2.2.5 Optical coherence tomography (OCT)

Between the three-dimensional, low-resolution, large field-of-view imaging techniques such as MRI and ultrasound, and the two-dimensional, high resolution, small field-of-view imaging techniques such as fundoscopy and AO-SLO, OCT provides three-dimensional, high resolution images of the different tissue structures of the eye over a large field-of-view. First commercialized in 1996, OCT is now a standard imaging technique both for pre-clinical and clinical eye imaging[34, 65-67]. OCT uses low-coherence interferometry to measure the echo time delay and intensity of the backscattered light as it penetrates the tissue. Light is sent into a Michelson interferometer composed of a beam splitter, a sample arm (ending at

the sample) and a reference arm (ending with a reflective surface). The light backscattered from different structures in the sample will interfere with the light reflected in the reference arm, leading to an interference pattern $I(\Delta z, \omega)$ dependent on both the path difference between the two arms Δz, and the frequency of the light source ω [68]. Information about the structure of the sample can thus be measured either by changing the reference arm length over time and measuring the resulting light intensity for each position (time-domain OCT) or keeping the length of the reference arm constant but measuring the resulting light intensity for each wavelength (frequency-domain OCT). Time-domain OCT can be implemented using a motor to move the reference arm mirror back and forth[33], although this severely limits the acquisition speed of the system. Frequency-domain OCT can be implemented in two ways: spectral-domain OCT[69], which uses a broadband light source and a spectrometer in front of the camera, and swept-source OCT[70], which uses a laser that rapidly sweeps across a range of wavelengths and a photodiode detector. Both spectral-domain and swept-source OCT allow for higher acquisition speeds since no moving parts are required.

In spectral-domain OCT as used in this dissertation, the interference signal is dispersed by the spectrometer into its different wavelengths and is then recorded by a charge-coupled device (CCD). The raw signal as a function of wavelength (λ) is then rescaled to be linear as a function of wavenumber k, where $k=2\pi/\lambda$. A Fourier Transform is then used to obtain the OCT signal as a function of depth from the raw signal as a function of wavenumber. The processed OCT signal is thus a complex signal where both the signal magnitude and phase vary as a function of depth. A single one-dimensional OCT scan (intensity as a function of depth) is called an A-scan, following the terminology from ultrasound imaging. Two-dimensional images are acquired by acquiring multiple A-scans along a line (B-scans), and three-dimensional images (C-scans) are constructed from multiple B-scans acquired at different locations. Multiple A-scans can also be acquired over time at the same sample location (M-scan).

The axial and lateral resolutions of OCT are independent from each other[68]. The lateral resolution is mostly dependent on the objective's numerical aperture and is often between 1.5μm and 9μm. The axial resolution is determined by the source wavelength and bandwidth, where small wavelengths and large

bandwidth lead to better resolution. Ophthalmic OCT systems will often be centered around 850-860nm with a 50 to 100nm bandwidth (axial resolution: ~3μm to 6μm), although swept-sources centered around 1050nm and 1310nm are also used for their high speed[42]. The central wavelength for the source is also chosen to maximize tissue penetration and increase imaging depth when needed, with 1310nm light usually penetrating deeper in scattering tissue than 860nm light. With such high axial resolution and imaging depth, different tissue layers can be distinguished on OCT images. Neither whole-body imaging techniques, which lack the resolution, nor SLO or fundus-based methods, which only acquire *en face* images, can produce those types of *in vivo* images.

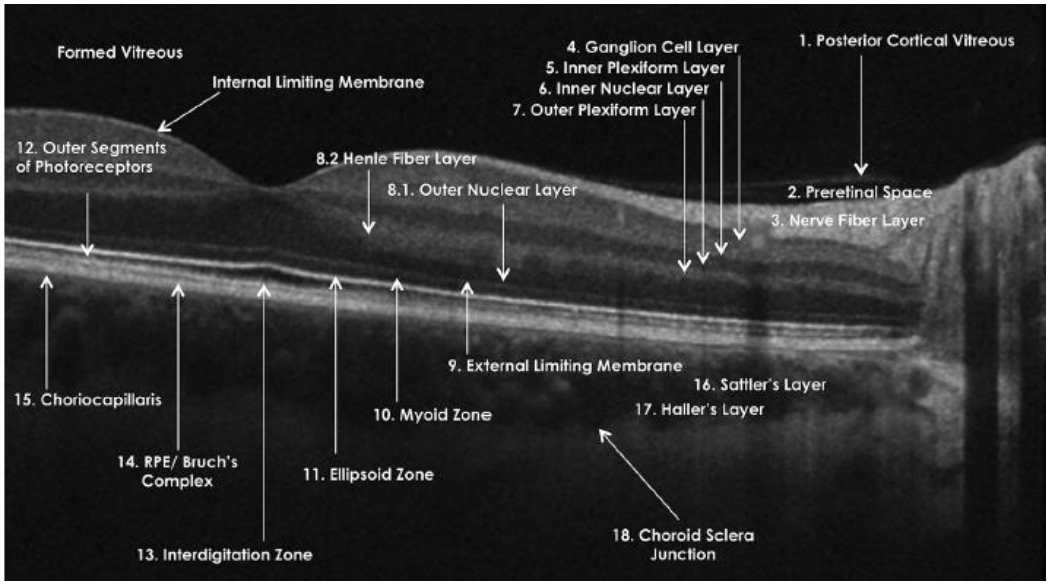

Figure 2.4. OCT intensity image of the healthy human retina. Retinal structures are labeled according to the International Nomenclature for Optical Coherence Tomography Panel. Reprinted with permission from [71]. Copyright 2014 American Academy of Ophthalmology.

The OCT signal is a complex signal and images can be formed based on the magnitude or phase of this signal. In most clinical applications, only the intensity (magnitude) information is used, and images are displayed as the logarithm in base ten of the signal magnitude. On a typical retinal OCT image, different tissue layers will appear as hyporeflective (low scattering) or hyperreflective (high scattering) on the intensity image. Tissue layers containing nuclei will usually appear as hyporeflective (outer nuclear layer and inner nuclear layer, see Fig. 2.4), and layers containing scattering structures will appear as hyperreflective (nerve bundles in the nerve fiber layer, melanin in the RPE, see Fig. 2.4). OCT intensity

images can be heavily speckled. Averaging multiple frames is a common method to reduce the speckle and improve the signal-to-noise ratio[72].

The phase of the OCT signal can also be used to extract sub-resolution information from the sample. For a given sample location, a change in phase over time can be interpreted as a sub-resolution change in optical path length, even when the OCT intensity image does not change[73]. The OCT phase signal is thus more sensitive to motion than the OCT intensity signal, and can be used to detect blood flow, tissue expansion or changes in refractive index. The smallest change in optical path length that can be detected from the phase signal is inversely proportional to the square root of the image signal-to-noise ratio (SNR). As a result, regions with high SNR will have a higher phase stability, and small changes in phase can be detected. Conversely, regions with low SNR will have poor phase stability and even large changes in phase might be undetectable due to noise. Functional OCT methods have been developed to enhance the OCT intensity images commonly used in clinical practice, and many of these methods have used the phase information to do so. In this dissertation, a method that uses the phase signal to detect absorbers in the OCT field-of-view is presented.

2.3 Functional OCT techniques

As previously mentioned, high-resolution, depth-resolved images can be created from the OCT intensity signal. However, the main source of contrast on OCT images is tissue backscattering, which provides limited functional information. Techniques such as OCT angiography (OCTA) and polarization-sensitive OCT (PS-OCT) have been demonstrated in human eyes, and in the case of OCTA, have now been included into commercial imaging systems to add functional contrast to OCT intensity images. Other techniques such as optical coherence elastography (OCE), enhanced-backscattering OCT, and spectroscopic OCT have also been recently demonstrated in the eye. Finally, additional functional OCT techniques such as pump-probe OCT, magnetomotive OCT, and photothermal OCT (PT-OCT) have been

developed to add contrast to OCT images, but have yet to be demonstrated in the eye. Herein is a description of the different functional OCT techniques and their application to the eye.

2.3.1 Optical coherence tomography angiography (OCTA)

OCTA is used to detect vasculature in the eye without the need for contrast agents[74]. OCTA is an alternative to fluorescein angiography or indocyanine green angiography, which require the injection of contrast agents and do not provide depth information. Multiple techniques have been developed to best detect blood flow using the OCT signal. They can be grouped as methods using the Doppler shift, or methods using speckle variance or decorrelation. In techniques using the Doppler shift, the phase change between repeated A-scans or B-scans due to moving blood cells is measured and used to calculate the flow velocity. However, this measurement is dependent on the angle between the blood vessels and the OCT beam, and in practice the Doppler shift can only measure the axial component of the blood velocity in relationship with the beam[75]. Additionally, Doppler shift methods use the phase information of the OCT signal which requires phase stability and the removal of background phase noise due to bulk tissue motion. As an alternative, speckle variance is a method that was initially developed to detect blood flow based on the OCT intensity signal alone[76]. In its simplest implementation, multiple OCT intensity images are used to calculate the variance of the speckle pattern over time. In static tissue the speckle pattern is relatively constant over time which leads to low pixel intensity variance between successive images. In comparison, the speckle pattern in blood vessels will vary over time due to the motion of blood cells (scatterers) and lead to a high variance in pixel intensity. A similar method, speckle decorrelation, is based on the cross-correlation of the OCT signal over time, with the OCT signal in static tissue staying correlated over a longer time period and blood vessels decorrelating more quickly. Since their introduction, different speckle variance and speckle decorrelation algorithms have been introduced to incorporate the OCT phase signal in addition to the intensity signal[74]. OCTA has been included in commercial OCT systems and can provide *en face* or depth-resolved views of the microvasculature in the retina and choroid.

2.3.2 Polarization-sensitive optical coherence tomography (PS-OCT)

While OCTA provides similar information as other commonly used angiography techniques, other functional OCT techniques such as PS-OCT are providing entirely new methods of contrast to better understand the eye. PS-OCT provides information about the birefringence of a sample and has been used to image the cornea and retina[77-79]. To perform PS-OCT, the incoming OCT light is circularly polarized. After passing through the sample, the outgoing light will then be in an arbitrary ellipsoid polarization pattern determined by the composition of the sample[80]. From there, individual detectors are used to measure the vertical and horizontal components of the polarized light. Depth-resolved images of the sample birefringence are then created and can be superimposed on the OCT intensity images. PS-OCT has been used to image the retina, especially to look at melanin and segment the RPE[81-83]. Melanosomes depolarize light much more than surrounding tissues, and this property can be extracted from the PS-OCT signal to identify the RPE. However, it is unclear whether the melanin itself, or the shape, size or number of melanosomes causes the depolarization, and scattering properties seem to be linked to depolarization [82]. It is thus difficult to quantify the melanin content based on the PS-OCT signal, especially since the PS-OCT signal is not always proportional to melanin concentration[82]. However, the PS-OCT signal does correlate with pigment distribution in the eye, which has been demonstrated in patients and animal models[78, 83].

2.3.3 Functional OCT techniques with emerging eye applications

As new functional OCT methods are being developed, new applications for eye imaging have been explored. This is the case of OCE which can be used to measure the biomechanical properties (elastic modulus) of tissue and has been used to study the cornea[84]. Deformation provided by direct contact, air-puff or a pulsed laser is used to compress the cornea while being imaged by OCT[85]. Small deformations (<1µm) and elastic wave propagation can be imaged with the phase signal of the OCT image. This method can also provide a measure of corneal stiffness. Different iterations of this technique have been demonstrated *ex vivo*[86] and *in vivo*[87] in animal models, and larger mechanical deformations have also been used in humans[88]. Other functional OCT techniques, such as enhanced-backscattering OCT and

spectroscopic OCT have also been demonstrated in the eye. Enhanced-backscattering OCT uses highly scattering contrast agents such as gold nanoparticles to increase scattering in tissues with low-scattering background. This technique was performed *in vivo* in mice to detect gold nanorods in the eye anterior chamber[89] and in retinal blood vessels[90]. Spectroscopic OCT is another technique that has recently been used to image the eye. It was used to identify and differentiate between types of blood cells after accumulation in the eye anterior chamber[91]. Spectroscopic OCT takes advantage of the large bandwidth of the OCT source to obtain wavelength dependent information on the sample. In past applications, this technique was used to highlight melanocytes in tadpoles [92] and differentiate between oxy- and deoxy-hemoglobin in the mouse skin[93]. Those advancements in OCE, enhanced back-scattering OCT and spectroscopic OCT are thus examples of how novel eye applications are continuously being investigated.

2.3.4 Other functional OCT techniques

Multiple functional OCT techniques have been developed for *in vitro* and *in vivo* applications in cells, cancerous tumors and drug delivery without yet being adapted for eye imaging. Pump-probe OCT was created to detect molecules such as methylene blue to add contrast to OCT[94]. This technique was the first OCT-based technique to detect such contrast agents. Pump-probe OCT uses a pump beam to excite the contrast agent to a different energy state which would then have an absorption peak in the OCT bandwidth. For example, methylene blue in its ground state absorbs in the visible range, but while excited in a higher energetic state, it absorbs around 830nm, which overlaps with the bandwidth of most 860nm-centered OCT systems[94]. By comparing A-scans with a without the pump, the presence and location of the dye can be calculated. Pump-probe OCT has mostly been demonstrated on exogenous dyes but it has been used once to detect melanin in an *ex vivo* eye[95].

Magnetomotive OCT, diffusion-sensitive OCT and photothermal OCT are three methods that have mostly been demonstrated with metallic nanoparticles as contrast agents. Magnetomotive OCT uses an electromagnet to move magnetic nanoparticles embedded in the tissue. The motion creates a change in optical path length that can then be detected in the phase of the OCT signal. This technique has been

demonstrated in cells[96] and *in vivo* in a rat tumor model[97]. Diffusion-sensitive OCT measures the diffusion of gold nanorods through phase decorrelation as a way to measure fluid viscosity. To this day, it has mainly been used to measure pulmonary mucus hydration[98]. Finally, photothermal OCT (PT-OCT) is a technique that detects optical absorbers by illuminating them with an additional laser combined to an OCT system[99, 100]. The temperature change caused by light absorption can then be detected as a phase change in the OCT signal.

To our knowledge, magnetomotive, pump-probe or photothermal OCT have not yet been performed in the living eye. The goal of this dissertation is to be the first demonstration of PT-OCT for retinal applications.

2.4 Photothermal OCT

PT-OCT is a type of functional OCT technique that detects optical absorbers in scattering tissues, with similar resolution and imaging depth as OCT. PT-OCT takes advantage of the photothermal effect, where photons absorbed by the contrast agent are re-emitted as heat. To perform PT-OCT, an additional laser is combined to a phase-sensitive OCT system, with the wavelength of this additional laser corresponding to the absorption peak of the contrast agent. The increase in temperature following photon absorption will cause a thermoelastic expansion surrounding the absorber, and a change in the refractive index of the tissue. The OCT signal and especially the OCT phase signal is sensitive to changes in optical path length[73], where the optical path length is defined as distance z multiplied by the refractive index n. An increase in temperature of <1°C in the tissue can thus be detected as a change in optical path length of <1nm. To facilitate the detection of the PT-OCT signal, the photothermal laser is amplitude-modulated over time at frequency f_0, so that the sample is repeatedly heated and left to cool down. The sample is then imaged in M-scan mode (repeated A-scans over time) to detect multiple heating cycles for each sample location. In the absence of an absorber or photothermal laser, the signal is constant over time (see Fig. 2.5a-i) except for small variations over time due to noise and phase decorrelation. When the contrast agent is present,

oscillations at frequency f_0 are observed in the OCT phase signal over time (see Fig. 2.5a-ii). The average amplitude of those oscillations is then defined as the PT-OCT signal. Basic PT-OCT instrumentation is composed of an additional photothermal laser that is amplitude-modulated and coupled to a standard spectral domain OCT system (see Fig. 2.5b).

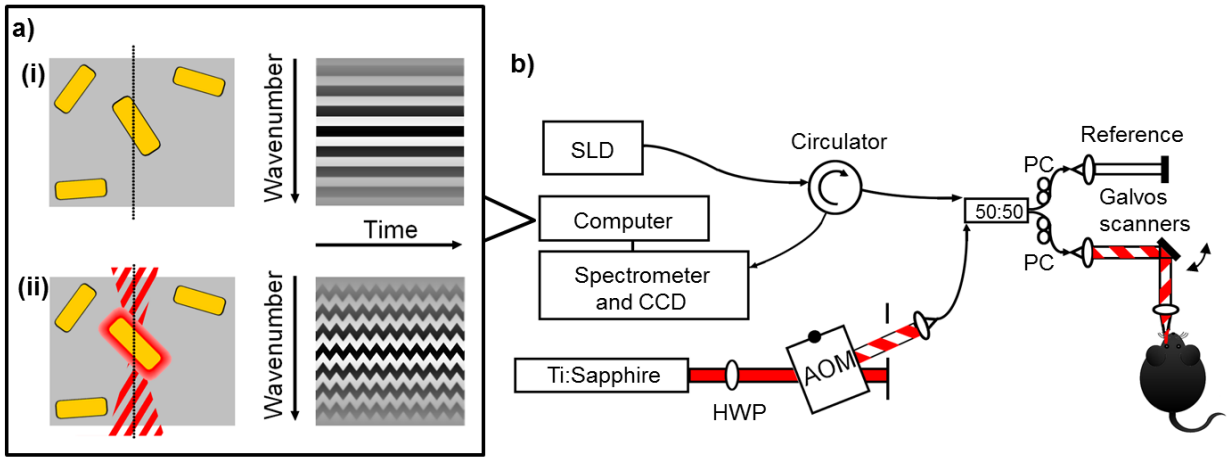

Fig. 2.5. Photothermal OCT principle and instrumentation. (A) Illustration of the OCT raw signal over time (i) in the absence of a photothermal beam and (ii) in the presence of an amplitude-modulated photothermal beam for a sample containing some gold nanorods (yellow). (B) PT-OCT instrumentation. Imaging beam (SLD) centered at λ=860 nm is divided between the reference and sample arm using a 50:50 fiber coupler. The photothermal beam (Ti:Sapphire, λ=750 nm) is amplitude modulated with an acousto-optic modulator (AOM), and coupled to the sample arm. A circulator redirects the light from the sample to the detector. HWP: Half-wave plate. PC: polarization controller. Reprinted from [101].

Multiple parameters can affect the oscillation amplitude[102]: the power of the photothermal laser, the frequency f_0 and duty-cycle of the laser modulation, the absorption coefficient of the sample (and the concentration of the contrast agent), the photothermal laser beam diameter, the thermal expansion coefficient of the sample, etc. However, the PT-OCT signal does increase linearly with the absorption coefficient of the sample and, keeping all other imaging parameters constant, enables quantitative imaging of absorbers[100, 103].

The PT-OCT signal is obtained in post-processing after image acquisition. First the raw data is processed similarly to ordinary OCT images: the interference signal as a function of wavelength λ is resampled to be linear in wavenumber k, the effect of the dispersion mismatch between the sample arm and the reference arm is corrected numerically[104], the DC reference spectrum and fixed pattern noise are

removed from the image, and a Fourier transform from wavenumber to depth is performed, from which the magnitude and phase of the OCT signal are obtained. The magnitude signal is used to create the traditional OCT intensity image showing the tissue structure, while the phase signal is further processed to obtain the PT-OCT signal. First, the derivative of the phase signal over time is taken at each sample depth to reduce the effect of phase wrapping[105]. Then, a Fourier transform in the temporal direction is taken to obtain the frequency spectrum of the OCT phase signal. At this stage, if both the photothermal laser and optical absorber were present at this sample location, a frequency peak should appear at f_0. The average amplitude of the noise floor (signal around f_0 but excluding f_0) is then subtracted from the amplitude of the peak at f_0, which is then defined as the PT-OCT signal. This signal is then transformed from units of milliradians (change in phase) to be expressed in units of nanometers of change in optical path length.

PT-OCT was first demonstrated *in vitro* in cells using gold nanospheres as a contrast agent[100], then in phantoms using gold nanoshells[99]. Gold nanoparticles were at first a popular contrast agent since they have a narrow, well-defined absorption peak that can be tuned based on particle geometry. Gold nanoparticles have also been investigated as potential drug delivery vehicles[106]. In further studies, gold nanoshells in breast tissue [107], gold nanorose in macrophage[108], gold nanorods in sentinel lymph nodes[109] and gold nanorings in tissue[110] were imaged *ex vivo*. PH-sensitive gold nanorods and gold nanodiscs[111] were also investigated in cells[112]. The first *in vivo* demonstration of PT-OCT was of gold nanorods in the mouse skin[102], followed by an *in vivo* study of gold nanorods accumulation in tumors after systemic injection in a mouse xenograft model[113]. Many other contrast agents were also tested in phantoms, such as blood[114], carbon nanotubes[115], ink[116] and indocyanine green[103]. Studies also imaged melanin *in vivo* in the human skin[117] and indocyanine green in the mouse lymphatics[118]. Some efforts were also made to accelerate PT-OCT image acquisition by using an optical lock-in method[111, 118].

OCT is an established eye imaging technique both at the research and clinical levels, and provides high-resolution, three-dimensional images of the eye structure. As previously described, functional OCT

techniques such as OCTA and PS-OCT have been performed in humans and provide perfectly co-registered functional contrast to OCT intensity images. At the moment, there is no standard eye imaging technique that specifically detects absorbers, especially not with the resolution and field-of-view unique to OCT. More specifically, there are no imaging technique that can quantify melanin *in vivo*, even though changes in pigmentations are observed in disease such as AMD. As previous studies have shown[100, 102, 113], PT-OCT can quantify absorbers in OCT images. PT-OCT has also never been performed in the *ex vivo* or *in vivo* eye. The development of PT-OCT for retinal imaging is thus the focus of the work presented in this dissertation.

2.5 References

[1] P. A. Tsonis, *Animal models in eye research*. Academic Press, 2011.

[2] I. Sanchez, R. Martin, F. Ussa, and I. Fernandez-Bueno, "The parameters of the porcine eyeball," *Graefe's Archive for Clinical and Experimental Ophthalmology*, vol. 249, no. 4, pp. 475-482, 2011.

[3] C. F. Burgoyne, "The non-human primate experimental glaucoma model," *Experimental eye research*, vol. 141, pp. 57-73, 2015.

[4] J. G. Fox, S. Barthold, M. Davisson, C. E. Newcomer, F. W. Quimby, and A. Smith, *The mouse in biomedical research: normative biology, husbandry, and models*. Elsevier, 2006.

[5] D. DiLoreto, D. A. Grover, C. del Cerro, and M. del Cerro, "A new procedure for fundus photography and fluorescein angiography in small laboratory animal eyes," *Current eye research*, vol. 13, no. 2, pp. 157-161, 1994.

[6] M. Paques *et al.*, "High resolution fundus imaging by confocal scanning laser ophthalmoscopy in the mouse," *Vision research*, vol. 46, no. 8-9, pp. 1336-1345, 2006.

[7] M. Ruggeri *et al.*, "In vivo three-dimensional high-resolution imaging of rodent retina with spectral-domain optical coherence tomography," *Investigative ophthalmology & visual science*, vol. 48, no. 4, pp. 1808-1814, 2007.

[8] O. Carrasco-Zevallos *et al.*, "Real-time 4D visualization of surgical maneuvers with 100kHz swept-source Microscope Integrated Optical Coherence Tomography (MIOCT) in model eyes," *Investigative Ophthalmology & Visual Science*, vol. 55, no. 13, pp. 1633-1633, 2014.

[9] E. M. Anger *et al.*, "Ultrahigh resolution optical coherence tomography of the monkey fovea. Identification of retinal sublayers by correlation with semithin histology sections," *Experimental eye research*, vol. 78, no. 6, pp. 1117-1125, 2004.

[10] M. E. Pennesi, M. Neuringer, and R. J. Courtney, "Animal models of age related macular degeneration," *Molecular aspects of medicine*, vol. 33, no. 4, pp. 487-509, 2012.

[11] (2015, 05/25/2018). *Common Eye Disorders*. Available: https://www.cdc.gov/visionhealth/basics/ced/index.html

[12] E. W. Ng, D. T. Shima, P. Calias, E. T. Cunningham Jr, D. R. Guyer, and A. P. Adamis, "Pegaptanib, a targeted anti-VEGF aptamer for ocular vascular disease," *Nature reviews drug discovery*, vol. 5, no. 2, p. 123, 2006.

[13] R. L. Avery, D. J. Pieramici, M. D. Rabena, A. A. Castellarin, A. N. Ma'an, and M. J. Giust, "Intravitreal bevacizumab (Avastin) for neovascular age-related macular degeneration," *Ophthalmology,* vol. 113, no. 3, pp. 363-372. e5, 2006.
[14] P. J. Rosenfeld *et al.*, "Ranibizumab for neovascular age-related macular degeneration," *New England Journal of Medicine,* vol. 355, no. 14, pp. 1419-1431, 2006.
[15] I. Bhutto and G. Lutty, "Understanding age-related macular degeneration (AMD): relationships between the photoreceptor/retinal pigment epithelium/Bruch's membrane/choriocapillaris complex," *Molecular aspects of medicine,* vol. 33, no. 4, pp. 295-317, 2012.
[16] P. E. Rakoczy, J. Meaghan, S. Nusinowitz, B. Chang, and J. R. Heckenlively, "Mouse models of age-related macular degeneration," *Experimental eye research,* vol. 82, no. 5, pp. 741-752, 2006.
[17] P. E. Rakoczy *et al.*, "Progressive age-related changes similar to age-related macular degeneration in a transgenic mouse model," *The American journal of pathology,* vol. 161, no. 4, pp. 1515-1524, 2002.
[18] G. Yiu *et al.*, "In Vivo Multimodal Imaging of Drusenoid Lesions in Rhesus Macaques," *Scientific reports,* vol. 7, no. 1, p. 15013, 2017.
[19] Y. Gong *et al.*, "Optimization of an image-guided laser-induced choroidal neovascularization model in mice," *PloS one,* vol. 10, no. 7, p. e0132643, 2015.
[20] A. Giani, "In vivo evaluation of laser-induced choroidal neovascularization using spectral-domain optical coherence tomography," *Investigative ophthalmology visual science,* vol. 52, no. 6 SRC - GoogleScholar, pp. 3880-3887, 2011.
[21] D. N. Hu, "Methodology for evaluation of melanin content and production of pigment cells in vitro," *Photochemistry and photobiology,* vol. 84, no. 3, pp. 645-649, 2008.
[22] C. N. Keilhauer and F. o. C. Delori, "Near-Infrared Autofluorescence Imaging of the Fundus: Visualization of Ocular Melanin," vol. 47, no. 8, pp. 3556-3564, 2006.
[23] J. H. Kim, M. H. Kim, D. H. Jo, Y. S. Yu, T. G. Lee, and J. H. Kim, "The inhibition of retinal neovascularization by gold nanoparticles via suppression of VEGFR-2 activation," *Biomaterials,* vol. 32, no. 7, pp. 1865-1871, 2011.
[24] J. H. Kim, J. H. Kim, K.-W. Kim, M. H. Kim, and Y. S. Yu, "Intravenously administered gold nanoparticles pass through the blood–retinal barrier depending on the particle size, and induce no retinal toxicity," *Nanotechnology,* vol. 20, no. 50, p. 505101, 2009.
[25] Z. Nadler, G. Wollstein, H. Ishikawa, and J. S. Schuman, "Clinical application of ocular imaging," *Optometry and Vision Science,* vol. 89, no. 5, p. E543, 2012.
[26] T. Ilginis, J. Clarke, and P. J. Patel, "Ophthalmic imaging," *British medical bulletin,* vol. 111, no. 1, 2014.
[27] H. R. Novotny and D. L. Alvis, "A method of photographing fluorescence in circulating blood in the human retina," *Circulation,* vol. 24, no. 1, pp. 82-86, 1961.
[28] R. Bernardes, P. Serranho, and C. Lobo, "Digital ocular fundus imaging: a review," *Ophthalmologica,* vol. 226, no. 4, pp. 161-181, 2011.
[29] N. Panwar *et al.*, "Fundus photography in the 21st century—a review of recent technological advances and their implications for worldwide healthcare," *Telemedicine and e-Health,* vol. 22, no. 3, pp. 198-208, 2016.
[30] H. Bartlett and F. Eperjesi, "Use of fundus imaging in quantification of age-related macular change," *Survey of ophthalmology,* vol. 52, no. 6, pp. 655-671, 2007.
[31] R. H. Webb, G. W. Hughes, and F. C. Delori, "Confocal scanning laser ophthalmoscope," *Applied optics,* vol. 26, no. 8, pp. 1492-1499, 1987.
[32] S. Schmitz-Valckenberg, J. Jorzik, K. Unnebrink, and F. G. Holz, "Analysis of digital scanning laser ophthalmoscopy fundus autofluorescence images of geographic atrophy in advanced age-related macular degeneration," *Graefe's archive for clinical and experimental ophthalmology,* vol. 240, no. 2, pp. 73-78, 2002.
[33] D. Huang *et al.*, "Optical coherence tomography," *Science (New York, NY),* vol. 254, no. 5035, p. 1178, 1991.

[34] M. R. Hee *et al.*, "Optical coherence tomography of the human retina," *Archives of ophthalmology,* vol. 113, no. 3, pp. 325-332, 1995.
[35] P. A. Keane, P. J. Patel, S. Liakopoulos, F. M. Heussen, S. R. Sadda, and A. Tufail, "Evaluation of age-related macular degeneration with optical coherence tomography," *Survey of ophthalmology,* vol. 57, no. 5, pp. 389-414, 2012.
[36] S. R. Freeman *et al.*, "Optical coherence tomography-raster scanning and manual segmentation in determining drusen volume in age-related macular degeneration," *Retina,* vol. 30, no. 3, pp. 431-435, 2010.
[37] Q. Chen *et al.*, "Automated drusen segmentation and quantification in SD-OCT images," *Medical image analysis,* vol. 17, no. 8, pp. 1058-1072, 2013.
[38] H. Oubraham *et al.*, "Inject and extend dosing versus dosing as needed: a comparative retrospective study of ranibizumab in exudative age-related macular degeneration," *Retina,* vol. 31, no. 1, pp. 26-30, 2011.
[39] M. A. Windsor, S. J. Sun, K. D. Frick, E. A. Swanson, P. J. Rosenfeld, and D. Huang, "Estimating Public and Patient Savings From Basic Research—A Study of Optical Coherence Tomography in Managing Antiangiogenic Therapy," *American journal of ophthalmology,* vol. 185, pp. 115-122, 2018.
[40] F. Semeraro, F. Morescalchi, S. Duse, E. Gambicorti, A. Russo, and C. Costagliola, "Current trends about inner limiting membrane peeling in surgery for epiretinal membranes," *Journal of ophthalmology,* vol. 2015, 2015.
[41] R. G. Schumann, A. Gandorfer, S. G. Priglinger, A. Kampik, and C. Haritoglou, "Vital dyes for macular surgery: a comparative electron microscopy study of the internal limiting membrane," *Retina,* vol. 29, no. 5, pp. 669-676, 2009.
[42] O. M. Carrasco-Zevallos *et al.*, "Review of intraoperative optical coherence tomography: technology and applications," *Biomedical Optics Express,* vol. 8, no. 3, pp. 1607-1637, 2017.
[43] Y. K. Tao, J. P. Ehlers, C. A. Toth, and J. A. Izatt, "Intraoperative spectral domain optical coherence tomography for vitreoretinal surgery," *Optics letters,* vol. 35, no. 20, pp. 3315-3317, 2010.
[44] O. Carrasco-Zevallos *et al.*, "Live volumetric (4D) visualization and guidance of in vivo human ophthalmic surgery with intraoperative optical coherence tomography," *Scientific reports,* vol. 6, p. 31689, 2016.
[45] P. N. Dayani, R. Maldonado, S. Farsiu, and C. A. Toth, "Intraoperative use of handheld spectral domain optical coherence tomography imaging in macular surgery," *Retina (Philadelphia, Pa.),* vol. 29, no. 10, p. 1457, 2009.
[46] K. M. Joos and J.-H. Shen, "Miniature real-time intraoperative forward-imaging optical coherence tomography probe," *Biomedical optics express,* vol. 4, no. 8, pp. 1342-1350, 2013.
[47] E. DeHoog and J. Schwiegerling, "Fundus camera systems: a comparative analysis," *Applied optics,* vol. 48, no. 2, pp. 221-228, 2009.
[48] R. H. Webb and G. W. Hughes, "Scanning laser ophthalmoscope," *IEEE Transactions on Biomedical Engineering,* no. 7, pp. 488-492, 1981.
[49] A. Von Rückmann, F. Fitzke, and A. Bird, "Distribution of fundus autofluorescence with a scanning laser ophthalmoscope," *British Journal of Ophthalmology,* vol. 79, no. 5, pp. 407-412, 1995.
[50] A. Manivannan, J. Plskova, A. Farrow, S. Mckay, P. F. Sharp, and J. V. Forrester, "Ultra-wide-field fluorescein angiography of the ocular fundus," *American journal of ophthalmology,* vol. 140, no. 3, pp. 525-527, 2005.
[51] G. Staurenghi, F. Viola, M. A. Mainster, R. D. Graham, and P. G. Harrington, "Scanning laser ophthalmoscopy and angiography with a wide-field contact lens system," *Archives of Ophthalmology,* vol. 123, no. 2, pp. 244-252, 2005.

[52] A. Roorda, F. Romero-Borja, W. J. Donnelly III, H. Queener, T. J. Hebert, and M. C. Campbell, "Adaptive optics scanning laser ophthalmoscopy," *Optics express,* vol. 10, no. 9, pp. 405-412, 2002.
[53] D. Merino and P. Loza-Alvarez, "Adaptive optics scanning laser ophthalmoscope imaging: technology update," *Clinical ophthalmology (Auckland, NZ),* vol. 10, p. 743, 2016.
[54] S. A. Burns, R. Tumbar, A. E. Elsner, D. Ferguson, and D. X. Hammer, "Large-field-of-view, modular, stabilized, adaptive-optics-based scanning laser ophthalmoscope," *JOSA A,* vol. 24, no. 5, pp. 1313-1326, 2007.
[55] J. Zhang, Q. Yang, K. Saito, K. Nozato, D. R. Williams, and E. A. Rossi, "An adaptive optics imaging system designed for clinical use," *Biomedical optics express,* vol. 6, no. 6, pp. 2120-2137, 2015.
[56] A. Dubra *et al.*, "Noninvasive imaging of the human rod photoreceptor mosaic using a confocal adaptive optics scanning ophthalmoscope," *Biomedical optics express,* vol. 2, no. 7, pp. 1864-1876, 2011.
[57] F. G. Holz, C. Bellmann, K. Rohrschneider, R. O. Burk, and H. E. Voölcker, "Simultaneous confocal scanning laser fluorescein and indocyanine green angiography," *American journal of ophthalmology,* vol. 125, no. 2, pp. 227-236, 1998.
[58] M. A. Mainster, G. T. Timberlake, R. H. Webb, and G. W. Hughes, "Scanning laser ophthalmoscopy: clinical applications," *Ophthalmology,* vol. 89, no. 7, pp. 852-857, 1982.
[59] U. Kellner, S. Kellner, B. H. Weber, B. Fiebig, S. Weinitz, and K. Ruether, "Lipofuscin-and melanin-related fundus autofluorescence visualize different retinal pigment epithelial alterations in patients with retinitis pigmentosa," *Eye,* vol. 23, no. 6, p. 1349, 2009.
[60] R. H. Silverman, "High-resolution ultrasound imaging of the eye–a review," *Clinical & experimental ophthalmology,* vol. 37, no. 1, pp. 54-67, 2009.
[61] B. A. Kilker, J. M. Holst, and B. Hoffmann, "Bedside ocular ultrasound in the emergency department," *European Journal of Emergency Medicine,* vol. 21, no. 4, pp. 246-253, 2014.
[62] S. Jiao *et al.*, "Photoacoustic ophthalmoscopy for in vivo retinal imaging," *Optics express,* vol. 18, no. 4, pp. 3967-3972, 2010.
[63] X. Shu, H. Li, B. Dong, C. Sun, and H. F. Zhang, "Quantifying melanin concentration in retinal pigment epithelium using broadband photoacoustic microscopy," *Biomedical optics express,* vol. 8, no. 6, pp. 2851-2865, 2017.
[64] A. Simha, A. Irodi, and S. David, "Magnetic resonance imaging for the ophthalmologist: A primer," *Indian journal of ophthalmology,* vol. 60, no. 4, p. 301, 2012.
[65] D. Huang *et al.*, "Optical coherence tomography," *science,* vol. 254, no. 5035, pp. 1178-1181, 1991.
[66] J. G. Fujimoto, C. Pitris, S. A. Boppart, and M. E. Brezinski, "Optical coherence tomography: an emerging technology for biomedical imaging and optical biopsy," *Neoplasia,* vol. 2, no. 1, pp. 9-25, 2000.
[67] J. Fujimoto and E. Swanson, "The development, commercialization, and impact of optical coherence tomography," *Investigative ophthalmology & visual science,* vol. 57, no. 9, pp. OCT1-OCT13, 2016.
[68] P. H. Tomlins and R. Wang, "Theory, developments and applications of optical coherence tomography," *Journal of Physics D: Applied Physics,* vol. 38, no. 15, p. 2519, 2005.
[69] A. F. Fercher, C. K. Hitzenberger, G. Kamp, and S. Y. El-Zaiat, "Measurement of intraocular distances by backscattering spectral interferometry," *Optics communications,* vol. 117, no. 1-2, pp. 43-48, 1995.
[70] S. Chinn, E. Swanson, and J. Fujimoto, "Optical coherence tomography using a frequency-tunable optical source," *Optics letters,* vol. 22, no. 5, pp. 340-342, 1997.
[71] G. Staurenghi, S. Sadda, U. Chakravarthy, and R. F. Spaide, "Proposed lexicon for anatomic landmarks in normal posterior segment spectral-domain optical coherence tomography: the IN• OCT consensus," *Ophthalmology,* vol. 121, no. 8, pp. 1572-1578, 2014.

[72] W. Wu, O. Tan, R. R. Pappuru, H. Duan, and D. Huang, "Assessment of frame-averaging algorithms in OCT image analysis," *Ophthalmic Surgery, Lasers and Imaging Retina,* vol. 44, no. 2, pp. 168-175, 2013.
[73] M. A. Choma, A. K. Ellerbee, C. Yang, T. L. Creazzo, and J. A. Izatt, "Spectral-domain phase microscopy," *Optics Letters,* vol. 30, no. 10, pp. 1162-1164, 2005.
[74] S. S. Gao *et al.*, "Optical coherence tomography angiography," *Investigative ophthalmology & visual science,* vol. 57, no. 9, pp. OCT27-OCT36, 2016.
[75] R. A. Leitgeb, R. M. Werkmeister, C. Blatter, and L. Schmetterer, "Doppler optical coherence tomography," *Progress in retinal and eye research,* vol. 41, pp. 26-43, 2014.
[76] J. K. Barton and S. Stromski, "Flow measurement without phase information in optical coherence tomography images," *Optics express,* vol. 13, no. 14, pp. 5234-5239, 2005.
[77] M. Pircher *et al.*, "Human macula investigated in vivo with polarization-sensitive optical coherence tomography," *Investigative ophthalmology & visual science,* vol. 47, no. 12, pp. 5487-5494, 2006.
[78] M. Pircher, C. K. Hitzenberger, and U. Schmidt-Erfurth, "Polarization sensitive optical coherence tomography in the human eye," *Progress in retinal and eye research,* vol. 30, no. 6, pp. 431-451, 2011.
[79] E. Götzinger, M. Pircher, I. Dejaco-Ruhswurm, S. Kaminski, C. Skorpik, and C. K. Hitzenberger, "Imaging of birefringent properties of keratoconus corneas by polarization-sensitive optical coherence tomography," *Investigative ophthalmology & visual science,* vol. 48, no. 8, pp. 3551-3558, 2007.
[80] J. F. De Boer, T. E. Milner, M. J. van Gemert, and J. S. Nelson, "Two-dimensional birefringence imaging in biological tissue by polarization-sensitive optical coherence tomography," *Optics letters,* vol. 22, no. 12, pp. 934-936, 1997.
[81] E. Götzinger *et al.*, "Retinal pigment epithelium segmentation by polarization sensitive optical coherence tomography," *Optics express,* vol. 16, no. 21, pp. 16410-16422, 2008.
[82] B. Baumann, "Polarization sensitive optical coherence tomography of melanin provides intrinsic contrast based on depolarization," *Biomedical optics express,* vol. 3, no. 7 SRC - GoogleScholar, pp. 1670-1683, 2012.
[83] B. Baumann *et al.*, "Melanin pigmentation in rat eyes: in vivo imaging by polarization-sensitive optical coherence tomography and comparison to histology," *Investigative ophthalmology & visual science,* vol. 56, no. 12, pp. 7462-7472, 2015.
[84] M. R. Ford, W. J. Dupps, A. M. Rollins, A. S. Roy, and Z. Hu, "Method for optical coherence elastography of the cornea," *Journal of biomedical optics,* vol. 16, no. 1, pp. 016005-016005, 2011.
[85] S. Wang and K. V. Larin, "Optical coherence elastography for tissue characterization: a review," *Journal of biophotonics,* vol. 8, no. 4, pp. 279-302, 2015.
[86] S. Wang and K. V. Larin, "Noncontact depth-resolved micro-scale optical coherence elastography of the cornea," *Biomedical Optics Express,* vol. 5, no. 11, pp. 3807-3821, 2014.
[87] R. K. Manapuram *et al.*, "In vivo estimation of elastic wave parameters using phase-stabilized swept source optical coherence elastography," *Journal of biomedical optics,* vol. 17, no. 10, p. 100501, 2012.
[88] D. Alonso-Caneiro, K. Karnowski, B. J. Kaluzny, A. Kowalczyk, and M. Wojtkowski, "Assessment of corneal dynamics with high-speed swept source optical coherence tomography combined with an air puff system," *Optics express,* vol. 19, no. 15, pp. 14188-14199, 2011.
[89] A. Zerda *et al.*, "Optical coherence contrast imaging using gold nanorods in living mice eyes," *Clinical & experimental ophthalmology,* vol. 43, no. 4, pp. 358-366, 2015.
[90] D. Sen *et al.*, "High-resolution contrast-enhanced optical coherence tomography in mice retinae," *Journal of biomedical optics,* vol. 21, no. 6, pp. 066002-066002, 2016.

[91] R. Qian, R. P. McNabb, A. N. Kuo, and J. A. Izatt, "Anterior chamber blood cell differentiation using spectroscopic optical coherence tomography," in *Ophthalmic Technologies XXVIII*, 2018, vol. 10474, p. 1047411: International Society for Optics and Photonics.
[92] U. Morgner *et al.*, "Spectroscopic optical coherence tomography," *Optics letters*, vol. 25, no. 2, pp. 111-113, 2000.
[93] F. E. Robles, C. Wilson, G. Grant, and A. Wax, "Molecular imaging true-colour spectroscopic optical coherence tomography," *Nature photonics*, vol. 5, no. 12, pp. 744-747, 2011.
[94] K. D. Rao, M. A. Choma, S. Yazdanfar, A. M. Rollins, and J. A. Izatt, "Molecular contrast in optical coherence tomography by use of a pump–probe technique," *Optics letters*, vol. 28, no. 5, pp. 340-342, 2003.
[95] D. Jacob, R. L. Shelton, and B. E. Applegate, "Fourier domain pump-probe optical coherence tomography imaging of Melanin," *Optics express*, vol. 18, no. 12, pp. 12399-12410, 2010.
[96] A. L. Oldenburg, J. R. Gunther, and S. A. Boppart, "Imaging magnetically labeled cells with magnetomotive optical coherence tomography," *Optics letters*, vol. 30, no. 7, pp. 747-749, 2005.
[97] R. John *et al.*, "In vivo magnetomotive optical molecular imaging using targeted magnetic nanoprobes," *Proceedings of the National Academy of Sciences*, vol. 107, no. 18, pp. 8085-8090, 2010.
[98] R. Blackmon *et al.*, "Direct monitoring of pulmonary disease treatment biomarkers using plasmonic gold nanorods with diffusion-sensitive OCT," *Nanoscale*, vol. 9, no. 15, pp. 4907-4917, 2017.
[99] D. C. Adler, S. W. Huang, R. Huber, and J. G. Fujimoto, "Photothermal detection of gold nanoparticles using phase-sensitive optical coherence tomography," *Optics Express*, vol. 16, no. 7 SRC - GoogleScholar, pp. 4376-4393, 2008.
[100] M. C. Skala, M. J. Crow, A. Wax, and J. A. Izatt, "Photothermal optical coherence tomography of epidermal growth factor receptor in live cells using immunotargeted gold nanospheres," *Nano letters*, vol. 8, no. 10, pp. 3461-3467, 2008.
[101] M. Lapierre-Landry, A. Y. Gordon, J. S. Penn, and M. C. Skala, "In vivo photothermal optical coherence tomography of endogenous and exogenous contrast agents in the eye," *Scientific reports*, vol. 7, p. 9228, 2017.
[102] J. Tucker-Schwartz, T. Meyer, C. Patil, C. Duvall, and M. Skala, "In vivo photothermal optical coherence tomography of gold nanorod contrast agents," *Biomedical optics express*, vol. 3, no. 11, pp. 2881-2895, 2012.
[103] H. M. Subhash, H. Xie, J. W. Smith, and O. J. McCarty, "Optical detection of indocyanine green encapsulated biocompatible poly (lactic-co-glycolic) acid nanoparticles with photothermal optical coherence tomography," *Optics letters*, vol. 37, no. 5, pp. 981-983, 2012.
[104] M. Wojtkowski, V. J. Srinivasan, T. H. Ko, J. G. Fujimoto, A. Kowalczyk, and J. S. Duker, "Ultrahigh-resolution, high-speed, Fourier domain optical coherence tomography and methods for dispersion compensation," *Optics express*, vol. 12, no. 11, pp. 2404-2422, 2004.
[105] R. K. Wang and A. L. Nuttall, "Phase-sensitive optical coherence tomography imaging of the tissue motion within the organ of Corti at a subnanometer scale: a preliminary study," *Journal of biomedical optics*, vol. 15, no. 5, p. 056005, 2010.
[106] Y. Diebold and M. Calonge, "Applications of nanoparticles in ophthalmology," *Progress in retinal and eye research*, vol. 29, no. 6, pp. 596-609, 2010.
[107] C. Zhou *et al.*, "Photothermal optical coherence tomography in ex vivo human breast tissues using gold nanoshells," *Optics letters*, vol. 35, pp. 700-702, 2010.
[108] A. S. Paranjape *et al.*, "Depth resolved photothermal OCT detection of macrophages in tissue using nanorose," *Biomedical optics express*, vol. 1, no. 1, pp. 2-16, 2010.
[109] Y. Jung, R. Reif, Y. Zeng, and R. K. Wang, "Three-dimensional high-resolution imaging of gold nanorods uptake in sentinel lymph nodes," *Nano letters*, vol. 11, no. 7, pp. 2938-2943, 2011.
[110] T.-T. Chi *et al.*, "Photothermal optical coherence tomography based on the localized surface plasmon resonance of Au nanoring," *Optics express*, vol. 22, no. 10, pp. 11754-11769, 2014.

[111] C. Pache *et al.*, "Fast three-dimensional imaging of gold nanoparticles in living cells with photothermal optical lock-in Optical Coherence Microscopy," *Optics express,* vol. 20, no. 19, pp. 21385-21399, 2012.
[112] P. Xiao *et al.*, "Detection of pH-induced aggregation of "smart" gold nanoparticles with photothermal optical coherence tomography," *Optics letters,* vol. 38, no. 21, pp. 4429-4432, 2013.
[113] J. M. Tucker-Schwartz, K. R. Beavers, W. W. Sit, A. T. Shah, C. L. Duvall, and M. C. Skala, "In vivo imaging of nanoparticle delivery and tumor microvasculature with multimodal optical coherence tomography," *Biomedical optics express,* vol. 5, no. 6, pp. 1731-1743, 2014.
[114] B. Yin *et al.*, "Dual-wavelength photothermal optical coherence tomography for imaging microvasculature blood oxygen saturation," *Journal of Biomedical Optics,* vol. 18, no. 5, p. 056005, 2013.
[115] J. M. Tucker-Schwartz, T. Hong, D. C. Colvin, Y. Xu, and M. C. Skala, "Dual-modality photothermal optical coherence tomography and magnetic-resonance imaging of carbon nanotubes," *Optics letters,* vol. 37, no. 5, pp. 872-874, 2012.
[116] G. Guan, R. Reif, Z. Huang, and R. K. Wang, "Depth profiling of photothermal compound concentrations using phase sensitive optical coherence tomography," *Journal of biomedical optics,* vol. 16, no. 12, pp. 126003-1260039, 2011.
[117] S. Makita and Y. Yasuno, "In vivo photothermal optical coherence tomography for non-invasive imaging of endogenous absorption agents," *Biomedical optics express,* vol. 6, no. 5, pp. 1707-1725, 2015.
[118] J. M. Tucker-Schwartz, M. Lapierre-Landry, C. A. Patil, and M. C. Skala, "Photothermal optical lock-in optical coherence tomography for in vivo imaging," *Biomedical optics express,* vol. 6, no. 6, pp. 2268-2282, 2015.

CHAPTER 3

Depth-resolved analytical model and correction algorithm for photothermal optical coherence tomography

M. Lapierre-Landry, J. M. Tucker-Schwartz, and M. C. Skala, "Depth-resolved analytical model and correction algorithm for photothermal optical coherence tomography," *Biomedical optics express*, vol. 7, no. 7, pp. 2607-2622, 2016.

3.1 Abstract

Photothermal OCT (PT-OCT) is an emerging molecular imaging technique that occupies a spatial imaging regime between microscopy and whole-body imaging. PT-OCT would benefit from a theoretical model to optimize imaging parameters and test image processing algorithms. We propose the first analytical PT-OCT model to replicate an experimental A-scan in homogeneous and layered samples. We also propose the PT-CLEAN algorithm to reduce phase-accumulation and shadowing, two artifacts found in PT-OCT images, and demonstrate it on phantoms and *in vivo* mouse tumors.

3.2 Introduction

Photothermal optical coherence tomography (PT-OCT) is an emerging technique[1, 2] that would allow the imaging of contrast agents *in vivo* with a field-of-view (>25mm^2), imaging depth (>1mm) and resolution (<15μm transverse) comparable to traditional OCT. However, PT-OCT images are still affected by two artifacts: phase-accumulation (signal becoming brighter with depth) and shadowing below high intensity regions. A method has been proposed to correct those artifacts[3] but this method also drastically decreases the signal-to-noise ratio of the image.

A theoretical model of PT-OCT would allow for a better understanding of the photothermal signal, give indications on how to optimize the imaging procedure, and would be a tool toward solving the problem of phase accumulation and shadowing. Separate components of the photothermal process have been modeled in the past, including the sample heating through the bio-heat conduction equation [4], the change

in optical path length due to the change in temperature[3], the reflectivity of a sample with specific optical characteristics[5] and the phase sensitivity as a function of the signal-to-noise ratio in OCT[6].

We propose a model that assembles those individual components and includes the evolution of the photothermal signal with depth. This is the first model to replicate reliably a PT-OCT A-scan for a homogenous sample and for a layered heterogeneous sample. This model can be customized to the specific instrument (spectral-domain or swept-source OCT), imaging parameters, and sample characteristics. Furthermore, we have used the model to implement a variation of the CLEAN algorithm[7] which successfully eliminated the effect of phase accumulation and shadowing in phantom images and in images of heterogeneous tumors acquired *in vivo*. This paper will present the equations necessary to implement this analytical model of PT-OCT and our version of the CLEAN algorithm. Experimental validations in phantoms will also be presented in each section.

3.3 Theory

3.3.1 Model of photothermal signal generation

PT-OCT relies on photothermal heating of contrast agents by a laser illumination source. For the contrast agent to be heated, the photothermal laser light must first reach the contrast agent. The photothermal laser power *P(z)* was generated using a Monte Carlo simulation[8] that took into the absorption and scattering coefficient of the sample, respectively μ_a and μ_s (cm^{-1}) and z (μm), the distance travelled within the sample. Once the power that reaches the contrast agent is known (and the laser spot size is known), we can calculate how much heat will be emitted. The bio-heat conduction equation is used to model how the temperature will vary in the sample surrounding the contrast agent when it is illuminated. The bio-heat conduction equation with a heat source is the following[4]:

$$\frac{\partial T}{\partial t} = \frac{\varphi \mu_a}{\rho c} + \alpha \nabla^2 T \qquad (3.1)$$

where T (K) is the temperature, t (s) is the time, φ (W/m^2) is the photothermal laser fluence rate, ρ (kg/m^3) is the density of the sample, c (J/kg*K) is the specific heat of the sample and α (m^2/s) is the thermal diffusivity of the sample ($\alpha = k/\rho c$ where k (W/m*K) is the thermal conductivity of the medium). In the case where the laser spot size is small compared to the absorption depth, radial heat transfer dominates the heat conduction equation, which can then be solved in cylindrical coordinates. The temperature ΔT at the center of the laser beam ($r = 0$) will rise and fall over one modulation period ($2t_L$) of the photothermal laser in the following way[4]:

$$\Delta T(t, r=0) = \frac{P(z)\mu_a}{4\alpha\pi\rho c}\ln\left(1+\frac{t\alpha}{\omega^2(z)/8}\right), t < t_L \qquad (3.2)$$

$$\Delta T(t-t_L, r=0) = \frac{P(z)\mu_a}{4\alpha\pi\rho c}\ln\left(1+\frac{t_L\alpha}{\frac{\omega^2(z)}{8}+\alpha\left(t-t_L\right)}\right), t \geq t_L \qquad (3.3)$$

where t_L (s) is the dwell time of the photothermal laser on the sample before an acousto-optic modulator reduces the laser power to zero (square waves modulation, 50% duty cycle) and $\omega(z) = \omega_0\sqrt{1+\left(z/z_0\right)^2}$ is the 1/e^2 beam radius (ω_0 (μm) is the waist size inside the tissue estimated with a Monte Carlo simulation[9] and z_0 (μm) is the Rayleigh range of the objective). The change in temperature will cause the sample to undergo two changes: elastic expansion and change in index of refraction. Combined, these phenomena will cause a change in the optical path length (ΔOPL) detected by the OCT system. The change in OPL over a set amount of time (Δt) at each depth z can be calculated as follows[3]:

$$\Delta OPL(z) = OPL_{T_0+\Delta T} - OPL_{T_0} = \int_0^z \left(\left[n(T_0)+\frac{dn}{dT}\Delta T\right]\cdot\left[1+\beta\Delta T\right]-n(T_0)\right)dZ \qquad (3.4)$$

where T_0 (K) is the initial sample temperature, n is the index of refraction, dn/dT (K^{-1}) is the thermo-optic coefficient that is assumed to be constant for this model and β (K^{-1}) is the thermal expansion coefficient of the sample. In our sample, $dn/dT<0$ and $\beta>0$ thus both effects act against each other. Over multiple

photothermal excitation cycles, the variation in OPL will cause a change in phase $\Delta\Phi$ (mrad) in the OCT signal, which will be detected by our instrument[6]:

$$\Delta\Phi(z) = \frac{4\pi n \Delta OPL(z)}{\lambda_0} \qquad (3.5)$$

where λ_0 (nm) is the center wavelength of the OCT laser and the average index of refraction for the sample $n = n(T_0)$ is used.

3.3.2 Model of photothermal signal detection

Once the photothermal signal is generated inside a sample, the signal is detected using an OCT system. The signal $I(z)$, collected from one A-scan with a sub-resolution change in reflector position $\Delta\Phi(z)$, is calculated as[6]:

$$I(z) = \frac{\delta}{2e} S \Delta t \sqrt{R_s(z) R_R} e^{i\Delta\Phi(z)} \cdot \mathrm{sinc}(az) \qquad (3.6)$$

where δ (A/W) is the detector responsivity, e (C) is the electronic charge, S (W) is the power of the OCT laser source at the sample, Δt (μs) is the time to acquire one A-scan, $R_s(z)$ is the reflectivity at the sample as a function of depth inside the sample, and R_R is the reflectivity of the reference arm. The sinc function accounts for the spectrometer fall-off with depth, and the scaling constant a is determined experimentally. We use the following equation to calculate the reflectivity of the sample arm $R_s(z)$[5]:

$$R_s(z) = \frac{\mu_b \pi \omega^2(z) L_c e^{-2(\mu_s + \mu_a)z}}{4(nz)^2 \left[1 + \left(\frac{\pi\omega^2(z)}{4\lambda nz}\right)^2 \left(1 - \frac{nz}{n^2 f}\right)^2\right]} \qquad (3.7)$$

where μ_b (cm^{-1}) is the backscattering coefficient of the sample, L_c (μm) is the coherence length of the OCT laser and f (μm) is the focal position of the OCT beam. Reflectivity models specific for phase-sensitive detection[5, 6] were chosen over other models[10], because PT-OCT is a phase-sensitive technique.

The experimental signal also contains additive, uncorrelated Gaussian white noise, divided here into shot noise $A_{shot}(z)$[6] and environmental noise $A_{env}(z)$:

$$A_{shot}(z) = \sqrt{\frac{\delta}{e} S \Delta t R_R} e^{-i\phi_{rand}} \qquad (3.8)$$

$$A_{env}(z) = A_0 e^{-i\phi'_{rand}} \qquad (3.9)$$

where φ_{rand} and φ'_{rand} are uniformly distributed random phases between $-\pi$ and π and A_0 is an experimentally determined magnitude that includes other sources of noise (electronic, vibrational, thermal, etc.). The experimental phase change $\Delta\Phi_{exp}(z)$ is then calculated as the phase of the signal and noise terms added together.

$$\Delta\Phi_{\exp}(z) = \angle\left[I(z) + A_{shot}(z) + A_{env}(z)\right] \qquad (3.10)$$

The experimental phase change $\Delta\Phi_{exp}(z, t)$ is acquired over time (in practice 500-1000 repeated A-scans at the same location inside a sample), then a Fourier transform is used to go from the time domain to the frequency domain.

$$p(z, f) = FT(\Delta\Phi_{\exp}(z,t)) \qquad (3.11)$$

The photothermal signal is then defined as the magnitude of the signal at the laser modulation frequency f_0=500Hz. The photothermal signal is also weighted by the OCT laser wavelength λ, the average index of refraction n and the laser modulation frequency f_0 in order to have units of nm (same as ΔOPL). (See[4] for full derivation).

$$PTOCT(z) = \frac{|p(z, f_0)|\lambda}{4\pi^2 f_0 n \Delta t} \qquad (3.12)$$

The photothermal noise is calculated following the same equation but where $p(z, f_0)$ is replaced by the mean magnitude of nearby frequencies.

3.3.3 Model for heterogeneous samples

The model described in the previous sections is only valid for homogenous samples. However, quasi-heterogeneous samples can be created by superposing layers of different homogenous samples. First the power $P(z)$ is simulated for a multi-layer sample using the Monte Carlo method[8]. Then the temperature change ΔT and reflectivity $R_s(z)$ are calculated for each layer separately and combined as one continuous function vs depth. The beam waist $\omega(z)$ is again estimated using a Monte Carlo simulation of a focused Gaussian beam in a multi-layered sample[8]. The following calculation steps to obtain the PT-OCT signal are then the same as in the one-layer case.

3.3.4 PT-CLEAN algorithm to eliminate phase accumulation and shadowing

The CLEAN algorithm was invented in the 1970s with applications in radio astronomy[11] before being adapted for microwave imaging[12]. It was then adapted for OCT to reduce speckle noise, cancel coherent artifacts and improve resolution[7, 13]. The CLEAN algorithm relies on a basic procedure: deconstruct an image point-by-point using the point-spread function (PSF) proper to the instrument, then re-construct the image point-by-point using a modified PSF to improve image quality. In the case of PT-OCT, we want to correct for phase accumulation and shadowing, thus a PSF without those two artifacts will be used for reconstruction.

First, our analytical model of PT-OCT is used to create the PSF of our system. Using the theoretical model for this step is more practical than to image a thin, homogeneous absorber (<10μm) that could be approximated as a point. For the PSF, a 7μm thick absorbing and scattering layer of tissue (thickness on the order of the OCT axial resolution) is simulated and serves as a 1D PSF of PT-OCT, denoted $h(z)$. This PSF can be generated with approximated values for the scattering and absorption coefficients since it will be normalized in the next step of the algorithm. Second, the original experimental PT-OCT B-scan is considered, and the first pixel in depth to have a photothermal signal above a certain threshold (ΔOPL = 2

nm) is selected (coordinates [$x^{(1)}$, $z^{(1)}$]). Third, the following deconvolution kernel is subtracted from the original image[7]:

$$\varepsilon h\left[z - z^{(1)}\right] D_{image}\left[x^{(1)}, z^{(1)}\right] / h_{\max} \qquad (3.13)$$

where ε<1 is the loop gain, or fraction of the image that is removed at each iteration of the algorithm, $h[z-z^{(1)}]$ is the PT-OCT PSF centered at [$x^{(1)}$, $z^{(1)}$], $D_{image}[x^{(1)}, z^{(1)}]$ is the intensity of the selected pixel in the original PT-OCT B-scan and h_{max} is the maximum value of the PSF. A point of intensity $\delta[x^{(1)}, z^{(1)}] = \varepsilon \cdot D_{image}[x^{(1)}, z^{(1)}]$ at position [$x^{(1)}$, $z^{(1)}$] is then saved for the final image reconstruction.

The next iteration then starts by finding the first pixel in depth to have a photothermal signal above threshold in the remaining image (original image minus deconvolution kernel):

$$D_{image} - \varepsilon h\left[z - z^{(1)}\right] D_{image}\left[x^{(1)}, z^{(1)}\right] / h_{\max} \qquad (3.14)$$

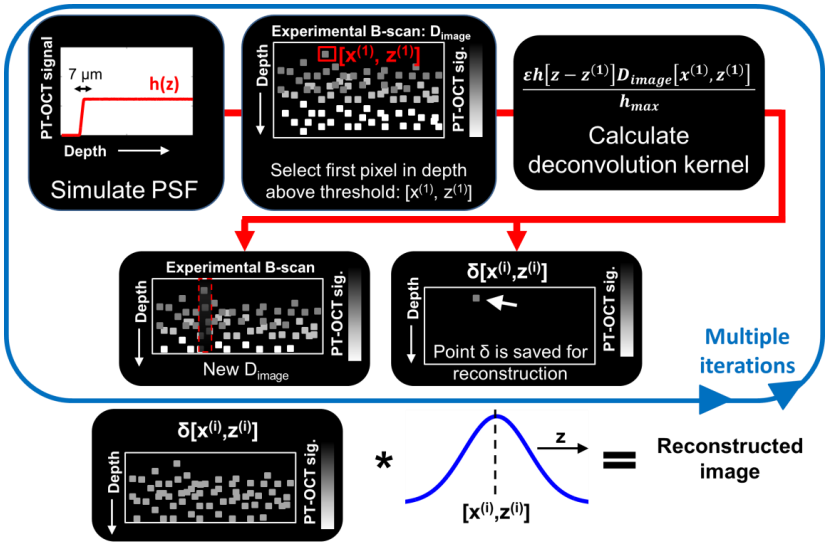

Fig. 3.1. Flow diagram of the PT-CLEAN algorithm to remove phase accumulation and shadowing. A point spread function is created using the analytical model. The first pixel in depth with a PT-OCT signal above threshold is then selected to calculate the deconvolution kernel. Two new images are created; a B-scan from which the deconvolution kernel was subtracted and a new image where the selected pixel is recorded. The final image is reconstructed by convoluting each of the individual saved pixels to a 1-D Gaussian along the depth dimension.

then we proceed as described for the previous iteration. The iterative process is stopped when the brightest pixel is below the noise floor of the original image. The final CLEANed image is obtained by convoluting each points $\delta[x^{(i)}, z^{(i)}]$ with a Gaussian function of 7μm in width at half maximum. What is left of D_{image} after the iterative process can be added to the CLEANed image to provide a realistic-looking noise floor. The PT-CLEAN algorithm takes into account the decreasing SNR of the image with depth since the PSF also has a decreasing SNR with depth. Additionally, a speckle-correction algorithm can be used if necessary in combination with the PT-CLEAN algorithm to improve data visualization.

A summary of the PT-CLEAN algorithm can be seen in Fig. 3.1

3.4 Methods and instrumentation

3.4.1 Instrumentation

A commercial spectral-domain OCT system (Bioptigen, Inc.) was altered for photothermal imaging (Fig. 3.2). A superluminescent diode imaging laser (SLD, Fig. 3.2) with λ_0=860 nm central wavelength and 40nm bandwidth (Superlum) was used as the OCT imaging beam. The light from the SLD was split between the sample and reference arms using a 50:50 fiber coupler (50:50, Fig. 3.2). Photothermal heating was provided by a wavelength tunable Titanium:Sapphire laser (Coherent). The wavelength of the PT laser was tuned to match the absorption peak of the contrast agent used (λ_{PT}=750nm for indocyanine green and brown human hair, λ_{PT}=740 nm for gold nanorods). The PT laser intensity was modulated by an acousto-optic modulator (Brimrose) (AOM, Fig. 3.2) following a square wave with frequency f_0=500 Hz. The light of the PT laser was combined to the superluminescent diode and sent to the reference and sample arms using the 50:50 fiber coupler. A telecentric lens (Bioptigen) was used to focus the light onto the sample ($1/e^2$ beam

diameter ω_0=28µm in air, 36µm simulated in tissue). The returning light was directed to the spectrometer and the CCD integrated to the Bioptigen system using a circulator (AC photonics).

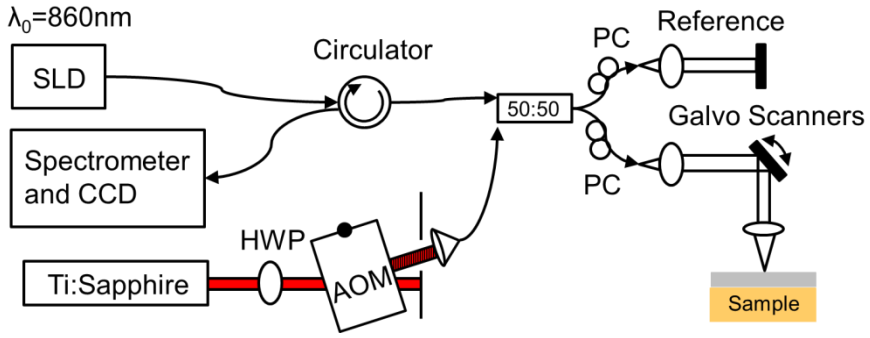

Fig. 3.2. PT-OCT instrumentation. The light from a superluminescent diode (SLD) is split between a reference and sample arm using a 50:50 fiber coupler (50:50). The photothermal excitation is provided by a Titanium:Sapphire laser (Ti:Sapphire) that is amplitude modulated by an acousto-optic modulator (AOM). HWP: Half-wave plate. PC: Polarization compensation.

3.4.2 Phantom fabrication

Clear silicone (Quantum Silicones) was used to create solid homogeneous phantoms. The silicone consists of two parts (base and curing agent) that need to be mixed in a 10:1 ratio. For all phantoms, rutile titanium dioxide (TiO_2, <5µm, Sigma Aldrich) was first added to the silicone base for a final concentration of 2.05mg/g ($\mu_s \approx 50 cm^{-1}$). The base and TiO_2 were then mixed for two minutes and degassed for two minutes using a planetary centrifugal mixer (Thinky USA). In phantoms where indocyanine green (ICG) was added, it was first dissolved into 800µL of 70% ethanol then added to the curing agent of the silicone. It was then mixed and degassed for two minutes each in the planetary centrifugal mixed (when ICG was not used, this step was skipped). Finally, the base and curing agent were mixed together and degassed. This final mixture was then poured into a petri-dish and placed under vacuum at 29 inches of Hg for five minutes with brief returns to standard pressure every minute.

To make layered phantoms, the final silicone mixture for each of the layers was poured between two glass slides with 115µm spacers attached on both sides. The layers were then cured at 70°C for 12h and superimposed after curing. For single-layer phantom the silicone mixture was poured into a petri-dish and then cured following the same procedure.

A phantom was made using a human brown hair as a thin absorbing layer. A silicone mixture was prepared as described above (no ICG). Then, a single hair was attached to both sides of the petri-dish so it would form the hypotenuse of a right triangle of known height (petri-dish depth) and length (petri-dish diameter). The silicone mixture was then poured into the petri-dish, covering part of the hair strand. Using trigonometry, it was thus possible to know the depth of the hair as it progressively penetrated the silicone. The phantom was then cured.

3.4.3 Imaging parameters and signal processing for phantom experiments

For every phantom experiment, the SLD power at the sample was 2mW, with a 36μm $1/e^2$ beam radius at the focus (in silicone). The photothermal laser power at the sample was varied in between 2mW and 16mW depending on the experiment. For each 1D depth-resolved PT-OCT A-scan, 1000 OCT A-scans were recorded over time with every OCT A-scan lasting Δt=100 μs. Each OCT-A scan was resampled from a linear wavelength space to a linear wavenumber space, then corrected for dispersion and background subtracted[4]. A Chirp-Z transform was used to convert the wavenumber data to depth-resolved data. The phase data at each point in depth was then used for the rest of the analysis. The temporal derivative of the phase at each point was calculated and a Fourier transform was taken in the temporal dimension. The data was then treated exactly like the data generated by the analytical model (see Eq. 3.13).

For each experimental validations of the model, one B-scan (4mm in length) containing 400 PT-OCT A-scans was averaged to produce one noise-reduced PT-OCT A-scan and facilitate data visualization. The same method was used with the data generated by the model.

3.4.4 *In vivo* imaging

All animal work was approved by the Vanderbilt IACUC committee, and all surgical procedures were performed using aseptic techniques. One nude female mouse ($Foxn1^{nu}$/ $Foxn1^{nu}$, The Jackson Laboratory) underwent dorsal skinfold surgery to enable imaging of MDA-MB-231 (human, breast) tumors. Following baseline (pre-injection) PT-OCT imaging (no signal detected), gold nanorods (AuNRs)

coated with methoxy-terminated poly(ethylene glycol) (PEG) were injected (200μL injection, 9nM) with a retro-orbital injection. The mouse was imaged again 17h post-injection with PT-OCT while under anesthesia (isoflurane mixed with air, 1.5-2%). The full protocol, including AuNRs synthesis and surgical procedure is described in detail in[14]. For this experiment, the photothermal laser was set to λ_{PT}=740 nm, with 70mW of power at the sample. The SLD delivered 6.6mW of power at the sample. B-scans were acquired and processed as previously described.

3.4.5 Input parameters for the analytical model

Two different samples were simulated using the PT-OCT theoretical model: a one layer, 5 mm thick silicone phantom containing TiO_2 (2mg/g) and ICG (0.09mg/g), and a silicone phantom containing TiO_2 (2mg/g) and a human brown hair. The different variables that were used to implement the theoretical model for those two samples can be seen in Table 3.1.

Table 3.1. Input parameters for PT-OCT analytical model

Optical properties	5mm ICG phantom	Human hair phantom
Scattering coefficient μ_s (cm^{-1})	50[15]	(Silicone) 50 (Hair) 55[16]
Absorption coefficient μ_a (cm^{-1})	11[17]	(Silicone) 0.005[18] (Hair) 50[16]
PT laser power P_0 (mW)	0-16	15
PT laser wavelength (nm)	750	750
Back-scattering coefficient μ_b (cm^{-1})	1*†	1*†
Thermal conductivity k (W/K)	0.18[18]	0.25[19]
Specific heat c (J/kg*K)	1200[18]	1602[19]
Density of medium ρ (kg/m^3)	1020[18]	1100[19]
Laser beam radius ω_0 (μm)	36[9]	36
Rayleigh length z_0 (μm)	1000	1000
Depth of focus z_f (μm)	400	400
Dwell time of PT laser t_L (ms)	1	1
Index of refraction n	1.44[18]	(Silicone) 1.44 (Hair) 1.55[16]
Thermo-optic coefficient dn/dT (K^{-1})	-340 x 10^{-6}[20]	-110 x 10^{-6}[3]*
Thermal expansion coefficient β (K^{-1})	275 x 10^{-6}[18]	100 x 10^{-6}[3]*
OCT wavelength λ_0 (nm)	860	860
OCT power S (mW)	2	2
OCT coherence length (μm)	15.1	15.1
Detector responsivity δ (A/W)	0.2	0.2
A-scan acquisition time Δt (μs)	100	100

*Approximate value since exact values were not found in the literature.
†If necessary, the backscattering coefficient can be more precisely determined with published methods[21].

3.5 Results

3.5.1 Demonstration of the analytical model

The parameters for a thick silicone phantom containing TiO_2 and ICG (Table 3.1, first column) were used to visualize the model output at different steps of the simulation. The first behavior illustrated by the model is the change in OPL (Eq. 3.5) which is a result of the cyclic variations in temperature caused by the photothermal laser and contrast agent. Our model simulates both the change in OPL at different depths inside the sample (Fig. 3.3a) and at a fixed depth over time (Fig. 3.3b). At this step, only the physical change in the sample is simulated. We still need to detect the change in OPL using an OCT system. This step is done using Eq. 3.11, which calculates the experimental change in phase detected by a realistic OCT system. The experimental phase change is shown over time (Fig. 3.3c) at the same sample location depicted in Fig.3.3b (z=400μm). A Fourier transform is then performed on the experimental phase change signal

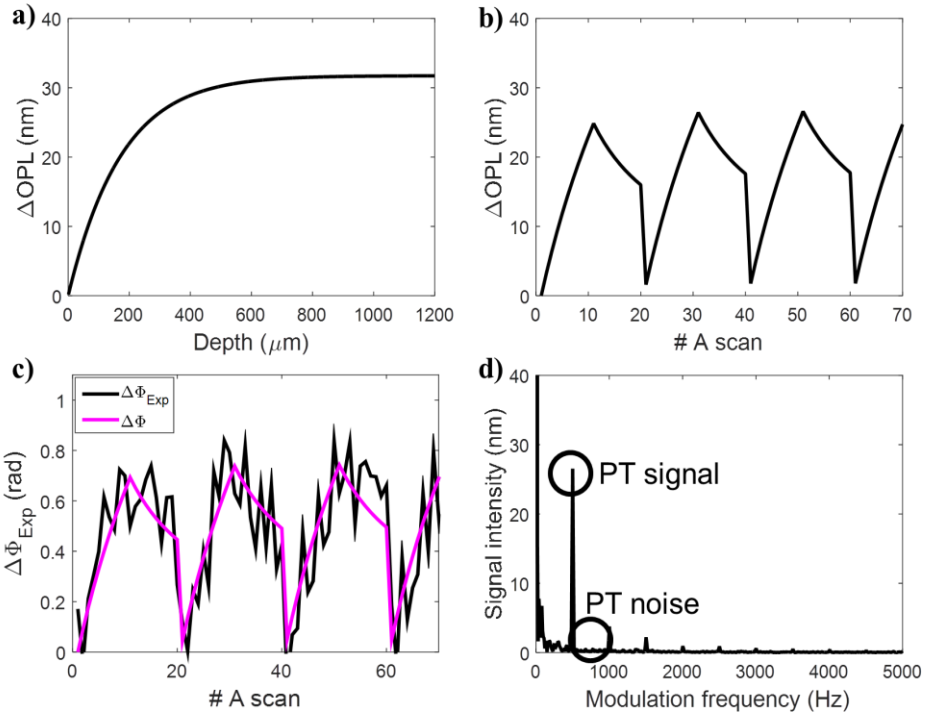

Fig. 3.3. Demonstration of the PT-OCT analytical output signal. (A) The change in optical path length produced in the sample by the photothermal effect is plotted as a function of depth and (B) at a fixed depth z=400 μm over repeated A-scans. (C) The simulated change in optical path length is detected as a noisy change in phase by the OCT system. The noiseless change in phase is overlaid in magenta to guide the eye. (D) A Fourier transform of the phase signal is taken to isolate the PT signal and PT noise.

(Eq. 3.12, 3.13) and the PT-OCT signal is taken as the amplitude of the peak at the modulation frequency f_0=500 Hz.

Two characteristics of the signal can be observed from Fig. 3.3a for ΔOPL and Eq. 3.6 for ΔΦ(z): phase accumulation and shadowing. Phase accumulation describes the fact that ΔΦ increases with depth for a homogenous sample, and thus the photothermal signal will be detected as increasing, even though the amount of contrast agent in the sample is constant with depth. Experimentally, this causes images to become brighter with depth even though the sample is homogeneous. Shadowing designates a region of high intensity in a region of the sample not containing any absorbers, simply because it is directly below a high absorbing region. Those two phenomena happen because, as seen in Eq. 3.5, when $\Delta T \geq 0$, ΔOPL can only increase or remain stable with depth. ΔΦ is a function of optical path length which integrates with depth. Since we are never cooling the sample below its initial temperature, ΔOPL and ΔΦ can never decrease with depth, which causes phase accumulation and shadowing. Both phase accumulation and shadowing are detrimental to the image quality of PT-OCT.

3.5.2 Validation of the analytical model (monolayer)

A thick one-layer silicone phantom with 90μg of ICG per gram of silicone was imaged to validate the result predicted by the theoretical model (parameters from Table 3.1, first column). The power of the photothermal laser at the sample was varied between 0mW and 16mW. The resulting average PT-OCT signal can be seen in Fig. 3.4 for both the analytical model (blue) and the experimental validation (red). The two signals overlap throughout the field of view of the OCT system, for all powers of the PT laser. In each case, both the experimental and theoretical signal initially increases with depth, a result of phase accumulation. However, the signal becomes dominated by noise between 500μm and 600μm in depth, a result of the low reflectivity of the sample. This region in depth shows poor agreement between the theoretical signal and the experimental signal. However, this region of poor agreement corresponds to a region already dominated by noise (i.e. SNR is equal to or less than 1). Thus, the model will not routinely

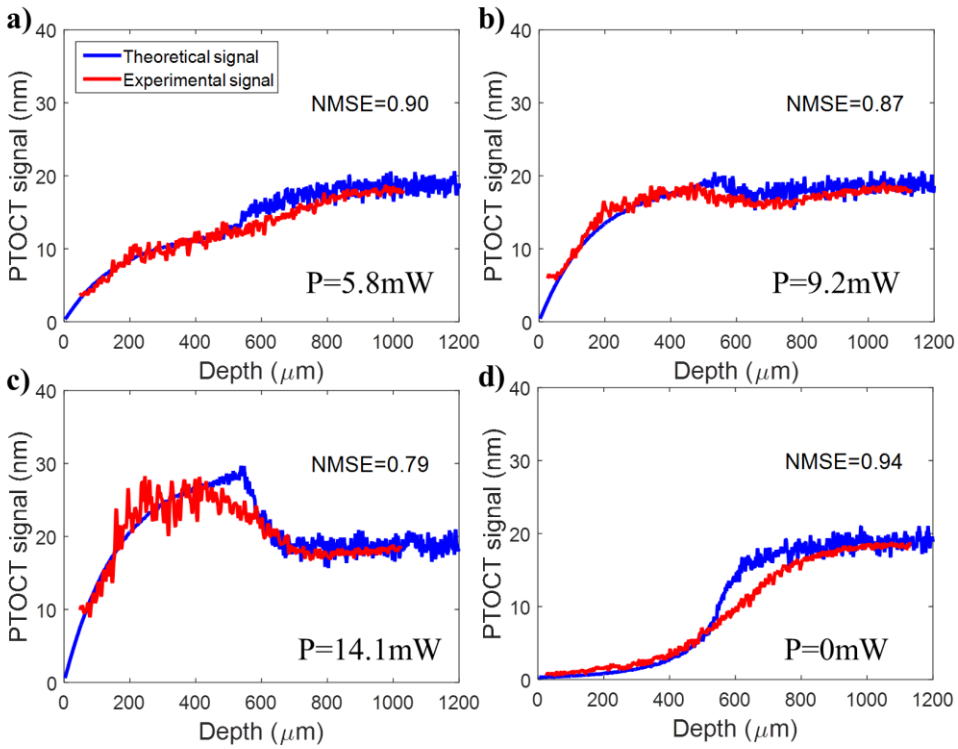

Fig. 3.4. Validation of the PT-OCT analytical model over an A-scan in a single layer homogeneous sample. The theoretical signal (blue) was generated from the model based on the optical properties listed in Table 1 (5mm ICG phantom). The experimental signal (red) is the average A-scan obtained experimentally by performing PT-OCT on a silicone phantom containing ICG as an absorber. The photothermal laser power at the sample was fixed at (A) 5.8mW, (B) 9.2mW and (C) 14.1mW to show the behavior of the signal in relation to the noise floor. The noise floor can be seen in (D) when the photothermal laser is turned off. NMSE: Normalized Mean Square Error.

be used to interpret data at these low SNR levels. Contrary to intuition, the noise floor (caused by the shot noise) is situated at 18nm in PT-OCT signal (see Fig 3.4d). This is because the noise follows a 1/f behavior and happens to have a value of 18nm at f=500Hz. When the SNR approaches one, the PT-OCT signal invariably increases or decreases to reach 18nm.

3.5.3 Validation of the analytical model (multi-layer) and PT-OCT imaging depth

A second experiment was used to investigate the maximum imaging depth of PT-OCT and validate the multi-layer model. The silicone phantom containing the human brown hair was imaged in such a way that the hair is at a different known depth (between 0 and 450μm from the surface of the phantom to the center of the hair) every B-scan. The hair was considered to be 130μm in diameter. An A-scan showing the experimental signal (Fig. 3.5a, red) from a hair at 80μm in depth and the corresponding theoretical signal

(Fig. 3.5a, blue) are shown to validate the multi-layer analytical model. The model input to generate the analytical signal can be found in Table 3.1, second column.

To observe how the PT-OCT signal intensity decreases with the absorber depth, results from multiple hair depths were compared. For each hair depth, the PT noise was subtracted from the PT signal and this resulting signal was averaged over the cross section of the hair. The result was then recorded vs

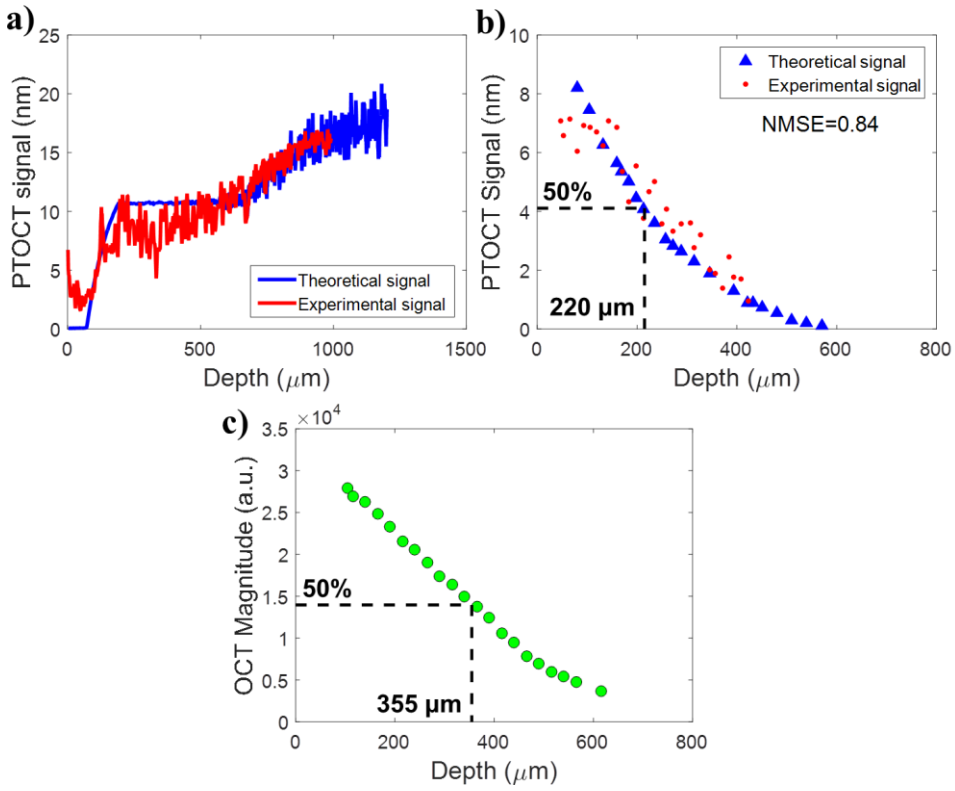

Fig. 3.5. Validation of the PT-OCT analytical model over an A-scan in a multi-layered heterogeneous sample. (A) Theoretical (blue) and experimental (red) A-scan of a human brown hair 80 μm deep inside a scattering silicone phantom. (B) Average theoretical and experimental photothermal signal for different hair depths. Each hair depth was produced by a separate simulation or recorded on a separate B-scan. The signal has decreased by 50% when the hair is 220 μm in depth inside the phantom. (C) Experimental average OCT intensity for a section of scatterer at different depths inside the sample. The signal has decreased by 50% when the scatterers are 355 μm in depth inside the phantom.

the hair depth (see Fig. 3.5b, red). The same value was generated by the analytical model (Fig. 3.5b, blue). The experimental and theoretical values overlapped for most of the hair positions. The normalized mean square error (NMSE) was calculated between theoretical and experimental values at matched depth to

quantify the agreement between the model predictions and the experimental result. (NMSE=0.84, perfect agreement when NMSE=1).

We compared the evolution of the PT signal with depth and the evolution of the OCT signal intensity with depth (Fig. 3.5c). For this we measured the average OCT intensity of an area of scatterer inside the phantom, progressively choosing areas at greater depths inside the sample. By comparing the point where the experimental PT signal and the experimental OCT signal have decreased by 50% of their initial value, it was determined that for this specific sample, the PT signal had decreased by half at 220μm inside the sample, while the OCT intensity had decreased by half at 355μm inside the sample. This indicates that PT-OCT has a smaller imaging depth than OCT, but of similar order.

3.5.4 PT-CLEAN algorithm

To demonstrate the PT-CLEAN algorithm, multi-layered silicone phantoms containing only TiO_2 (2.05mg/g) or both TiO_2 and ICG were created. First, a thin layer (115μm) of ICG phantom was deposited on top of a thick (>5 mm) phantom containing only TiO_2. The sample was imaged with 15mW of PT laser power at the sample and intensity modulated at 500Hz. A single B-scan with 400 A-scans/B-scan was acquired (see Fig. 3.6a). Some phase accumulation can be seen in the absorbing (ICG) layer. A large amount of signal is also present in the non-absorbing layer from the effect of shadowing. The PT-CLEAN algorithm was applied to the B-scan with a loop gain of 0.01 and photothermal threshold of 2nm. Those parameters were chosen experimentally to optimize accuracy, run-time and reduce speckle. The resulting B-scan is displayed in Fig. 3.6b. In the PT-CLEAN image, the signal inside the absorbing layer is more constant with depth (reduced phase accumulation) and the signal in the scattering layer decreases rapidly to the noise floor (reduced shadowing) (the row-averaged mean signal is indicated as the solid white line on Fig.3.6 a-f). The signal peak at the surface of the CLEANed image stems from the fact that the first pixels in depth are all chosen first by the PT-CLEAN algorithm before it progresses to the rest of the sample. The phantom layer location on each B-scan was determined based on the OCT B-scan that was simultaneously acquired.

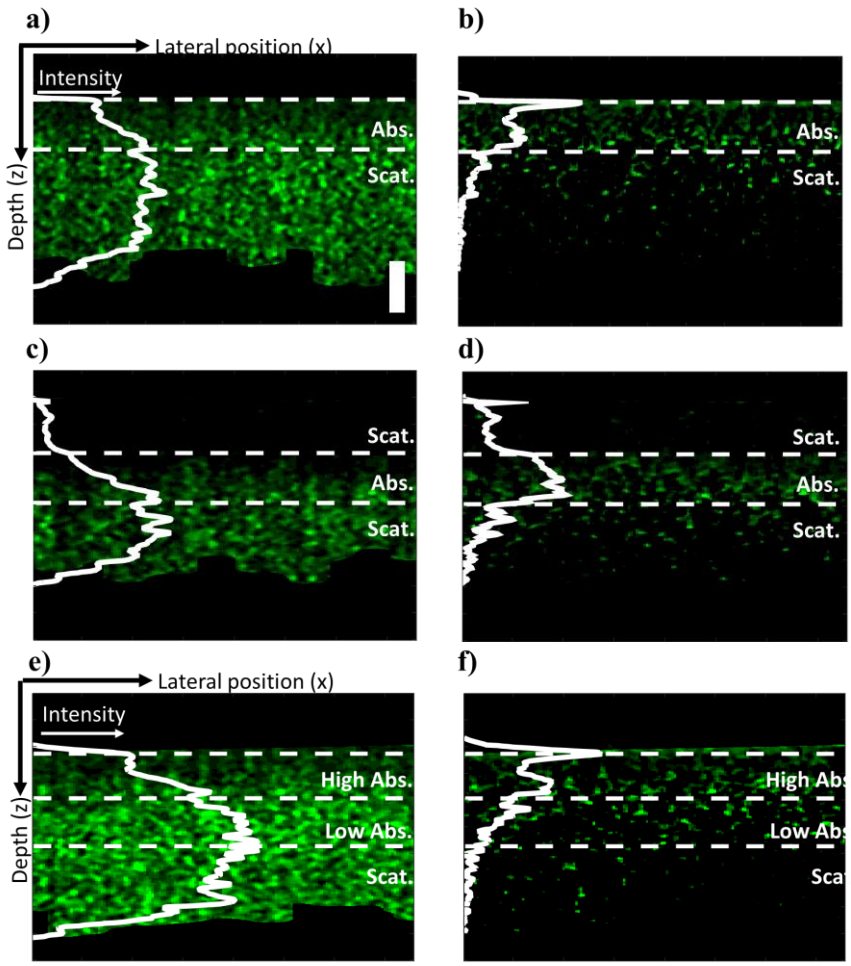

Fig. 3.6. Demonstration of the PT-CLEAN algorithm and comparison to traditional PT-OCT B-scans. (A) Thin ICG phantom on thick scattering (TiO_2) layer and (B) resulting B-scan after performing the PT-CLEAN algorithm. The horizontal dashed white lines indicate the limit of each layer. The solid white line is the average signal intensity vs. depth. (C) Thin ICG layer between a thin and a thick scattering layer and (D) after application of the PT-CLEAN algorithm. (E) Layer with a high ICG concentration, over a low ICG concentration layer, both over a scattering phantom and (F) after application of the PT-CLEAN algorithm. Scale bar: 100μm.

To test the robustness of the PT-CLEAN algorithm, a thin layer of phantom with TiO_2 and no ICG was added on top of the sample described previously and imaged with the same parameters (see Fig. 3.6c). The PT-CLEAN algorithm was applied with the same parameters and the resulting B-scan can be seen in Fig. 3.6d. Again, the PT-CLEAN signal is more constant over depth in the absorbing layer and close to the noise floor in the scattering layers.

An additional test for the PT-CLEAN algorithm is to differentiate between multiple concentrations of absorbers. Two thin layers of phantom were made with TiO_2 and respectively 11μg and 45μg of ICG per

gram of silicone. Both layers were then mounted on top of a thick phantom with only TiO_2 with the high concentration layer on top (see Fig. 3.6e). The imaging parameters and the PT-CLEAN parameters were the same as for the previous two experiments. The PT-CLEAN images can be seen in Fig. 3.6f. When the absorber concentration goes from high to low with depth (Fig. 3.6e and f), the traditional PT B-scan displays an increase in signal with depth throughout both absorbing layers, which is due to phase accumulation. However, the PT-CLEAN image shows a decreasing signal with depth that is proportional to the absorption from both layers. This shows the advantage of the PT-CLEAN algorithm over the traditional PT-OCT processing.

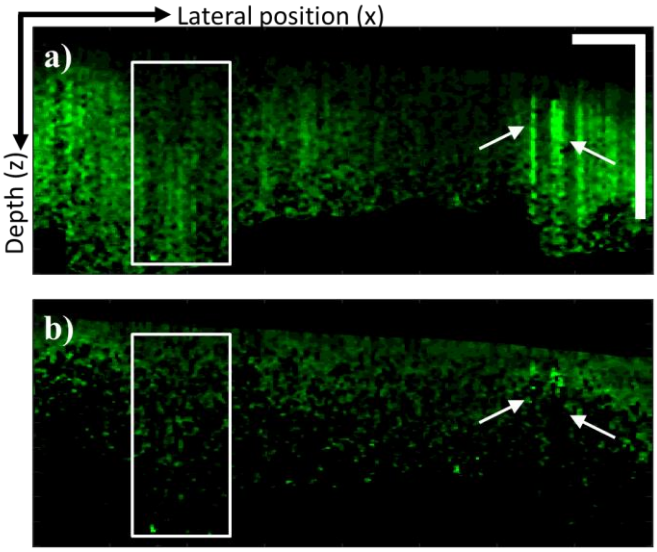

Fig. 3.7. Demonstration of the PT-CLEAN algorithm on *in vivo* tumor sample. (A) *In vivo* PT-OCT B-scan of a tumor xenograft after retro-orbital injection of gold nanorods. Both phase accumulation (boxed area) and shadowing (arrows) are visible. (B) B-scan after application of the PT-CLEAN algorithm. Both phase accumulation and shadowing are reduced. Scale bar: 500μm.

The PT-CLEAN algorithm was also applied to a true heterogeneous sample: a mouse tumor xenograft imaged *in vivo* using a dorsal window 17h after systemic injection of gold nanorods through the tail vein. Both the original PT-OCT B-scan and the PT-CLEANed scan can be seen in Figure 3.7a and b. Phase accumulation and shadowing are shown to be reduced by the PT-CLEAN algorithm even in a truly heterogeneous sample. A median filter was also applied to the original PT-OCT B-scan (Fig. 3.7a) and the PT-CLEANed B-scan (Fig. 3.7b) to demonstrate the use of a speckle-correction technique in combination with the PT-CLEAN algorithm.

3.6 Discussion

PT-OCT is an emerging technique for pre-clinical molecular imaging. It has been experimentally demonstrated *in vitro*, *ex vivo* and *in vivo* in the past and parts of its signal had been modeled. However, this is the first time that a comprehensive, customizable analytical model of a PT-OCT A-scan is presented for homogeneous and quasi-heterogeneous samples. We have validated our model against experimental data acquired in a homogeneous silicone phantom containing TiO_2 (scatterer) and ICG (absorber) at various photothermal laser powers, and in a multi-layer phantom containing TiO_2 and a human hair (absorber). Previous models of PT-OCT only described the general shape of the photothermal signal with depth and did not take into consideration the effect of noise. Our model is the first to match the data directly instead of being mathematically fitted to the experimental data points. Our model can also predict the A-scan obtained for different instrument design, imaging parameters, and sample composition.

By layering different sections of homogeneous samples, a heterogeneous sample was approximated. For *in vivo* drug delivery and molecular imaging experiments, it is expected that the contrast agent will diffuse through the sample and form a heterogeneous distribution. As a first step toward re-creating this situation, we created a three-layer phantom experiment and simulation: two large sections of scattering silicone surrounding a thin layer (130μm) of absorber. A human brown hair was used as the thin absorption layer. This choice of absorber allowed us to easily vary the position of the absorbing layer in depth inside the sample and to assure that no leaking of the absorber into the scattering layer occurred. We measured the photothermal signal as a function of the hair depth and determined that the photothermal signal decreases with depth slightly more rapidly than OCT. This experiment also validated our model for a multi-layered sample, as the experimental values agreed with the theoretical values (NMSE=0.84). The maximum imaging depth for PT-OCT is strongly dependent on the type of sample being imaged, how many absorbing layers it has and where they are located. With our analytical model, we can now predict the imaging depth that will be obtained in practice for a given sample, which could not be done theoretically before. We can also select imaging parameters (e.g. photothermal laser power, photothermal modulation

frequency, or the integration time of the detector) to maximize the signal strength in a specific sample. In the future, this model can be used to simulate a multi-layered sample that is a better approximation of a heterogeneous distribution of contrast agents inside a tissue sample.

Using our analytical model, we were able to simulate the PT-OCT signal from a homogeneous 7μm thick absorber, which would be impractical to do without a model. This provided a point-spread function for our PT-OCT system. It was then possible to implement a modification of the CLEAN algorithm, which relies on the PSF of an instrument to improve image resolution and quality. The PSF should be generated with realistic optical parameters for the sample and instrument used to re-create the most accurate PT-OCT image. With the PT-CLEAN algorithm, we have demonstrated that phase accumulation and shadowing can be reduced in different layered samples and in a heterogeneous *in vivo* tumor sample, which is an improvement over traditional photothermal B-scans. Additionally, PT-CLEAN preserves the units of change in optical path length proper to PT-OCT and does not require any assumption on the signal shape or the sample composition, which allows its application to homogeneous and heterogeneous samples. In comparison with an algorithm proposed before[3], PT-CLEAN does not assume that the change in optical path length is proportional to the geometrical depth inside the medium (as seen in Fig. 3.3a, ΔOPL levels off with depth). It is therefore appropriate for complex, heterogeneous samples, and was thus the first algorithm of its kind to be applied to *in vivo* PT-OCT B-scans. Axial resolution for PT-OCT used to be difficult to define, since a small region of absorber could create a large shadow once the B-scan was processed. With the PT-CLEAN algorithm, the shadowing is eliminated and the effective axial resolution of PT-OCT is improved.

In conclusion, we have presented and validated the first analytical model of PT-OCT that can predict signal intensity with depth in homogeneous and multi-layered samples. We have also presented the PT-CLEAN algorithm to reduce phase accumulation and shadowing, effectively improving the axial resolution of PT-OCT.

3.7 Acknowledgments

We would like to thank Daniel Gil, Antony Phipps, Kelsey Beavers, Megan Madonna and Taylor Cannon for their help on this project. We would also like to thank the generous funding from Vanderbilt University that supported this project.

3.8 References

[1] M. C. Skala, M. J. Crow, A. Wax, and J. A. Izatt, "Photothermal optical coherence tomography of epidermal growth factor receptor in live cells using immunotargeted gold nanospheres," *Nano letters*, vol. 8, no. 10, pp. 3461-3467, 2008.

[2] D. C. Adler, S. W. Huang, R. Huber, and J. G. Fujimoto, "Photothermal detection of gold nanoparticles using phase-sensitive optical coherence tomography," *Optics Express*, vol. 16, no. 7 SRC - GoogleScholar, pp. 4376-4393, 2008.

[3] G. Guan, R. Reif, Z. Huang, and R. K. Wang, "Depth profiling of photothermal compound concentrations using phase sensitive optical coherence tomography," *Journal of biomedical optics*, vol. 16, no. 12, pp. 126003-1260039, 2011.

[4] J. Tucker-Schwartz, T. Meyer, C. Patil, C. Duvall, and M. Skala, "In vivo photothermal optical coherence tomography of gold nanorod contrast agents," *Biomedical optics express*, vol. 3, no. 11, pp. 2881-2895, 2012.

[5] J. A. Izatt, E. A. Swanson, J. G. Fujimoto, M. R. Hee, and G. M. Owen, "Optical coherence microscopy in scattering media," *Optics letters*, vol. 19, no. 8, pp. 590-592, 1994.

[6] M. A. Choma, A. K. Ellerbee, C. Yang, T. L. Creazzo, and J. A. Izatt, "Spectral-domain phase microscopy," *Optics Letters*, vol. 30, no. 10, pp. 1162-1164, 2005.

[7] D. Piao, Q. Zhu, N. K. Dutta, S. Yan, and L. L. Otis, "Cancellation of coherent artifacts in optical coherence tomography imaging," *Applied optics*, vol. 40, no. 28, pp. 5124-5131, 2001.

[8] L. Wang, S. L. Jacques, and L. Zheng, "MCML—Monte Carlo modeling of light transport in multi-layered tissues," *Computer methods and programs in biomedicine*, vol. 47, no. 2, pp. 131-146, 1995.

[9] S. Jacques. (2007). *Monte Carlo Simulations*.

[10] L. Thrane, H. T. Yura, and P. E. Andersen, "Analysis of optical coherence tomography systems based on the extended Huygens–Fresnel principle," *JOSA A*, vol. 17, no. 3, pp. 484-490, 2000.

[11] J. Högbom, "Aperture synthesis with a non-regular distribution of interferometer baselines," *Astronomy and Astrophysics Supplement Series*, vol. 15, p. 417, 1974.

[12] J. Tsao and B. D. Steinberg, "Reduction of sidelobe and speckle artifacts in microwave imaging: The CLEAN technique," *IEEE Transactions on Antennas and Propagation*, vol. 36, no. 4, pp. 543-556, 1988.

[13] J. M. Schmitt, "Restoration of optical coherence images of living tissue using the CLEAN algorithm," *journal of Biomedical Optics*, vol. 3, no. 1, pp. 66-75, 1998.

[14] J. M. Tucker-Schwartz, K. R. Beavers, W. W. Sit, A. T. Shah, C. L. Duvall, and M. C. Skala, "In vivo imaging of nanoparticle delivery and tumor microvasculature with multimodal optical coherence tomography," *Biomedical optics express*, vol. 5, no. 6, pp. 1731-1743, 2014.

[15] A. L. Oldenburg, F. J.-J. Toublan, K. S. Suslick, A. Wei, and S. A. Boppart, "Magnetomotive contrast for in vivo optical coherence tomography," *Optics Express*, vol. 13, no. 17, pp. 6597-6614, 2005.

[16] T. van Kampen, "Optical properties of hair," *Masters project, January*, vol. 1, 1997.

[17] M. Landsman, G. Kwant, G. Mook, and W. Zijlstra, "Light-absorbing properties, stability, and spectral stabilization of indocyanine green," *Journal of applied physiology,* vol. 40, no. 4, pp. 575-583, 1976.
[18] I. Technical, *Quantum Silicones Sheet, QSil Available at http://quantumsilicones.com//02/qsil-216*. 2012.
[19] G. Liu, H. Lin, X. Tang, K. Bergler, and X. Wang, "Characterization of thermal transport in one-dimensional solid materials," *Journal of visualized experiments: JoVE,* no. 83, 2014.
[20] A. Norris, J. Degroot Jr., F. Nishida, U. Pernisz, N. Kuahibiki, and T. Ogawa, "Silicone Materials for Optical Applications.," Available: http://www.dowcorning.com.cn/zh_CN/content/publishedlit/75-1007-01_single.pfd
[21] A. L. Oldenburg, M. N. Hansen, D. A. Zweifel, A. Wei, and S. A. Boppart, "Plasmon-resonant gold nanorods as low backscattering albedo contrast agents," *Optics Express,* vol. 14, no. 15, pp. 6724-6738, 2006.

CHAPTER 4

In vivo photothermal optical coherence tomography of endogenous and exogenous contrast agents in the eye

M. Lapierre-Landry, A. Y. Gordon, J. S. Penn, and M. C. Skala, "In vivo photothermal optical coherence tomography of endogenous and exogenous contrast agents in the eye," *Scientific reports*, vol. 7, p. 9228, 2017.

4.1 Abstract

Optical coherence tomography (OCT) has become a standard-of-care in retinal imaging. OCT allows non-invasive imaging of the tissue structure but lacks specificity to contrast agents that could be used for *in vivo* molecular imaging. Photothermal OCT (PT-OCT) is a functional OCT-based technique that has been developed to detect absorbers in a sample. We demonstrate *in vivo* PT-OCT in the eye for the first time on both endogenous (melanin) and exogenous (gold nanorods) absorbers. Pigmented mice and albino mice (n = 6 eyes) were used to isolate the photothermal signal from the melanin in the retina. Pigmented mice with laser-induced choroidal neovascularization lesions (n=7 eyes) were also imaged after a systemic injection of gold nanorods to observe their passive accumulation in the retina. This experiment demonstrates the feasibility of PT-OCT to image the distribution of both endogenous and exogenous absorbers in the mouse retina.

4.2 Introduction

Optical coherence tomography (OCT) is a standard-of-care retinal imaging technique in the clinic, and is widely used to study retinal diseases in pre-clinical research[1]. In patients, OCT can diagnose and monitor diseases such as age-related macular degeneration (AMD)[2], diabetic retinopathy[3] and glaucoma[4]. In animal models, OCT is used to investigate new retinal therapies and understand disease progression[5, 6]. Quantitative diagnostic applications have been developed based on the segmentation and measured thickness of the different layers of the retina as seen on OCT[7]. However, automated segmentation can be difficult or inaccurate when layers are severely disturbed, such as in cases of

neovascularization (i.e., wet age-related macular degeneration) or detachment/displacement of the retinal pigment epithelium (i.e., drusen)[8].

Functional information could be used not only to increase the contrast of certain layers of the retina on OCT images and facilitate segmentation, but also to provide new disease markers, and develop new drug carriers. OCT in its traditional form is a poor candidate for molecular imaging because of its source of contrast, scattering due to variations in index of refraction, which does not significantly change between small molecules (e.g. antibodies, most fluorescent dyes). Contrast agents can be used with OCT to increase the backscattered signal in regions of interest[9] but the detection specificity of these contrast agents is poor against a scattering background[10] such as a neovascular lesion in AMD models. We thus propose photothermal OCT (PT-OCT) to image endogenous and exogenous absorbers in the eye, effectively adding new sources of contrast to structural OCT.

In this study, we used PT-OCT to image melanin and gold nanorods in the mouse eye. Sensitivity to an endogenous contrast agent is particularly useful in the eye, since few probes are FDA approved (namely indocyanine green), and contrast delivery is limited by the blood-retinal barrier. In pigmented animals, melanin is naturally present in the retinal pigment epithelium (RPE) and choroid, two layers of the retina, and its concentration and distribution can be indicative of different disease states, such as melanoma and age-related macular degeneration[11]. Increased contrast from melanin could also facilitate automatic segmentation of the RPE. Since melanin is an absorber in the near-infrared, detection with PT-OCT can be done directly, without the need for additional tags or dyes.

New exogenous contrast agents are being developed and non-invasive imaging would be particularly useful to assess their potential for *in vivo* applications. Gold nanoparticles have been investigated as possible contrast agents and drug carriers for the eye[5, 12-17]. There is a need for *in vivo* testing of those new particles to understand toxicity and biodistribution, but also because *ex situ* methods can cause particle aggregation artifacts[18]. However, current standards of quantifying biodistribution of gold nanoparticles, namely instrumental neutron activation analysis (INAA) and inductively coupled

plasma mass spectrometry (ICP-MS), are labor intensive and destructive to the sample[19]. Thus, a new imaging method to non-invasively detect gold nanoparticles in the eye would bring complimentary information to the current *ex vivo* methods.

Herein, we demonstrate PT-OCT in the eye for the first time, as a non-invasive OCT-based method to detect endogenous (melanin) and exogenous (gold nanorods) contrast agents, respectively, in the retinal pigment epithelium and in choroidal neovascular lesions.

4.3 Results

4.3.1 PT-OCT imaging of melanin in the retina

Pigmented mice (C57BL/6, n=6 eyes) and albino mice (BALB/c, n=6 eyes) with unperturbed retina (no lesions) and no contrast agent injection were imaged using PT-OCT to isolate the photothermal signal from melanin. OCT and PT-OCT images were acquired while the mice were kept under anesthesia. As seen in Fig. 4.1a, a strong photothermal signal was detected from the RPE and choroid of the pigmented mice, while no signal above the noise floor was detected in the albino mice. The PT-OCT signal is quantified as the change in optical path length, in units of nanometers. The signal is proportional to absorber concentration, photothermal laser power, and varies between contrast agents with different absorption coefficients. In this experiment, a high signal is interpreted as a high concentration of melanin. We have found a significant difference ($p<0.01$, Mann-Whitney U test) between the two experimental groups. An example B-scan for a pigmented mouse retina (Fig. 4.1b) and an albino mouse retina (Fig. 4.1c) is also shown. The location of the PT-OCT signal in depth is in accordance with the location of the RPE. This strongly indicates that melanin in the RPE can be detected with PT-OCT.

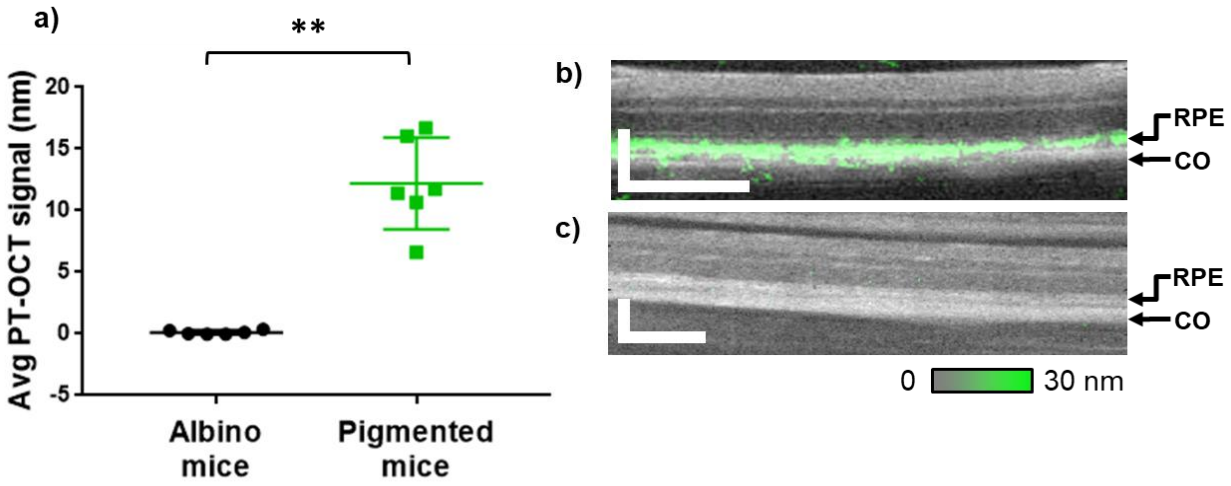

Fig. 4.1. *In vivo* PT-OCT of melanin. (A) Average PT-OCT signal from the retina for albino mice (no melanin) and pigmented mice (melanin) cohorts (n=6 eyes per group). Photothermal laser power at 8 mW. Mean with standard deviation shown. **p<0.01. (B) Example OCT B-scan of a pigmented mouse retina (grayscale) with PT-OCT signal overlaid (green). (C) Example OCT B-scan of an albino mouse retina (grayscale) with PT-OCT signal overlaid (green, no signal visible). The OCT images show fewer retinal layers than in a typical OCT B-scan of a human retina because of the smaller dimensions of a mouse retina and the axial resolution of standard 860nm OCT systems, which are also used for human retina imaging. The PT-OCT signal represents the change in optical path length, in units of nm. Scale bar: 100μm. RPE: retinal pigment epithelium. CO: choroid.

OCT-based imaging of melanin could have potential applications in medicine independently from studies centered on gold nanoparticles, since it could serve as an endogenous contrast agent. For this reason, we measured the average photothermal signal intensity from melanin across multiple mice at different photothermal laser powers (see Fig. 4.2). As seen in Fig. 4.2a, the intensity of the PT-OCT signal from the RPE, but also from the rest of the retina increases as the photothermal laser power increases. To better understand how the PT-OCT signal is distributed with depth in the retina, the average PT-OCT signal for one example eye can also be seen for different photothermal laser powers in Fig. 4.2b. The width of the peak produced by the melanin layer in the RPE does not seem to change with the photothermal laser power ($p>0.05$, Mann-Whitney U test, full width at half maximum). However, the magnitude of the signal from the RPE increases as the photothermal laser power increases, as expected.

Most biological tissues have a small absorption coefficient in the near-infrared (optical window), but at high powers, heat propagating outward from the RPE combined with absorption by the tissue layers above the RPE and the choroid below (and additionally phase accumulation[20]) can create a non-negligible background signal. As seen in Fig. 4.2c, the mean background signal (excluding the signal from the RPE) rises as the photothermal power increases. Inversely, the peak-to-background ratio (maximum signal value inside the RPE over background) decreases as the photothermal power increases. This strongly suggests that in further studies, PT-OCT of melanin in the eye should be performed at low laser powers (preferably

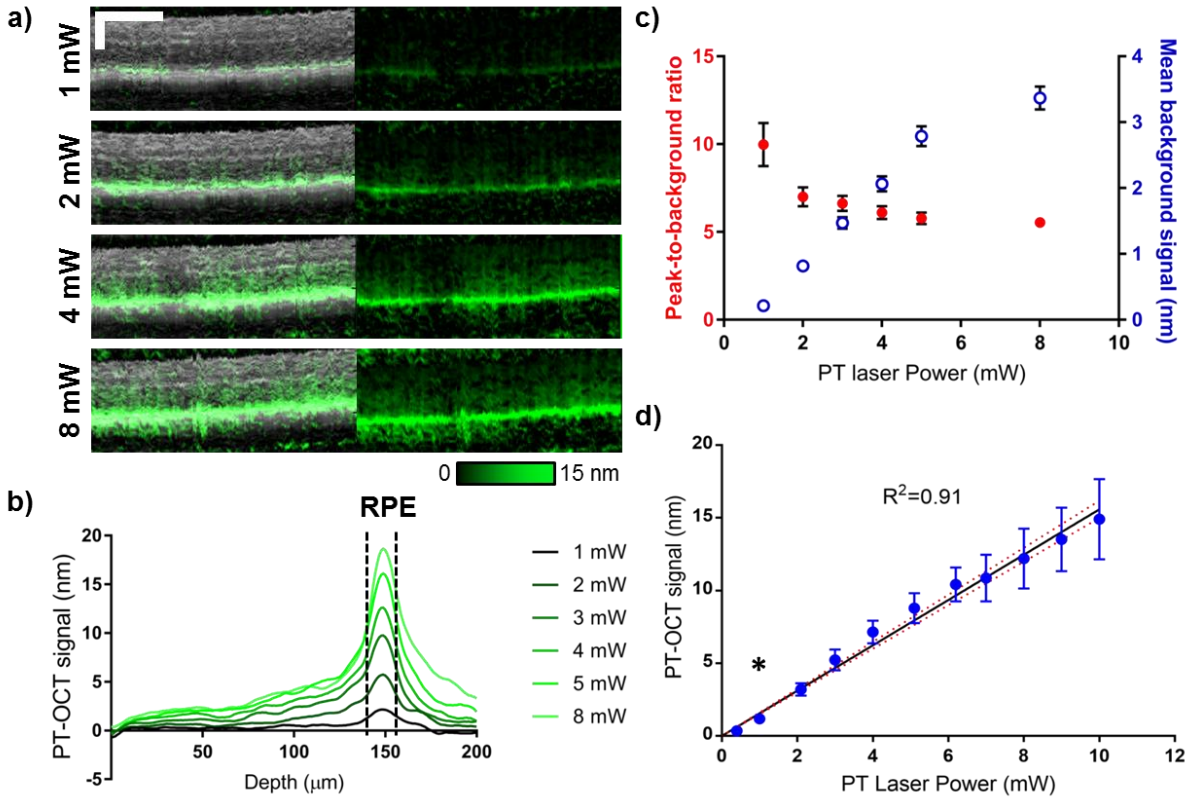

Fig. 4.2. ***In vivo*** **PT-OCT of melanin for different photothermal laser powers.** (A) Example OCT B-scans (grayscale, left) of a pigmented mouse retina with corresponding PT-OCT signal (overlaid in green on the left, signal alone on the right) collected for different photothermal laser powers (1-8 mW). Scale bar: 100 μm. (B) Average PT-OCT signal for one B-scan (400 A-scans) collected at different photothermal laser powers (same eye as presented in (A)). The width at half-maximum of the signal peaks (dashed black lines) corresponds to the location of the RPE in depth. (C) Mean background signal (excludes the dashed region from (B)) and peak-to-background ratio for one example eye at different photothermal laser powers. Error bar: standard error. (D) Mean PT-OCT signal as a function of photothermal laser power for n=6 eyes. Error bar: standard deviation. Linear fit y=1.56x with 95%CI on the fit (red dashed). R^2=0.91. *p<0.05 between 1mW and 0.4mW (Mann-Whitney U test).

1mW or less). This would decrease the overall heating in the retina, decrease the background signal, increase the peak-to-background ratio, and this could be accomplished without degrading the effective axial resolution. Additionally, a power of 1mW for a quickly scanned, low numerical aperture beam such as the photothermal laser is comparable in wavelength and power to routine OCT imaging in rodents[21].

As a validation of our method, the PT-OCT signal of melanin was measured and averaged for n=6 eyes for a wide-range of laser powers (0-10mW). As predicted by theory[20, 22], the increase in signal is linear with power increase (Fig. 4.2d; R^2=0.91). No PT-OCT signal was detected with photothermal laser powers lower than 0.5mW, including when the laser was turned off (0mW). There was a statistically significant increase between the PT-OCT signal acquired at 0.4mW (no signal) and the PT-OCT signal acquired at 1mW. This was observed across multiple mice with variable amounts of melanin in their retina.

4.3.2 PT-OCT imaging of gold nanorods in the retina

Pigmented mice (C57BL/6) underwent laser photocoagulation of the retina to create choroidal neovascular lesions. This is commonly referred to as the laser-induced choroidal neovascularization (LCNV) model, which has been widely used to study wet age-related macular degeneration[23, 24]. The lesions developed for five days after laser photocoagulation, and then fundoscopy was performed to observe

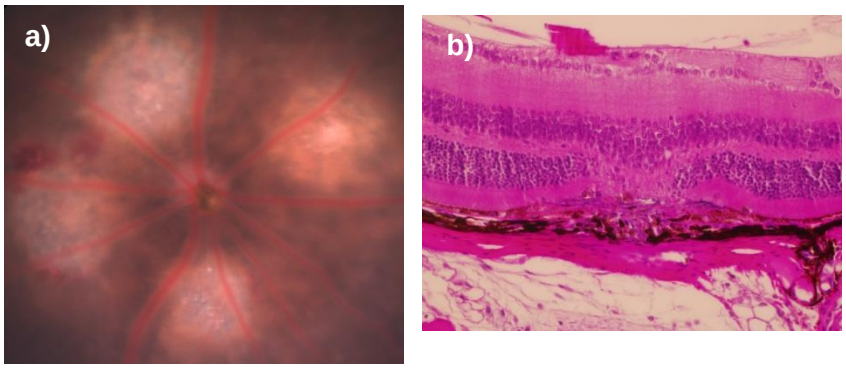

Fig. 4.3. Laser induced choroidal neovascularization (LCNV) lesion five days after laser photocoagulation. (A) Fundoscopy image showing four lesions around the optic nerve head. Scale bar: 400μm. (B) Hematoxylin and eosin (H&E) stained section of an LCNV lesion. Melanin is seen in brown.

the lesions. A typical lesion at five days after photocoagulation can be seen in Fig. 4.3. The mice were then injected via the tail vein with either polyethylene glycol (PEG)-coated gold nanorods or saline (control

group). Over time, the gold nanorods were expected to passively accumulate in the LCNV lesions, similarly to the way gold nanoparticles accumulate passively in tumors because of the enhanced permeability and retention (EPR) effect[16, 25, 26]. Six hours after injection, OCT and PT-OCT images were acquired while the mice were maintained under anesthesia. In each group, n=7 eyes were imaged with a photothermal laser power of 8mW. It was expected that the low concentration of the gold nanorods in the lesion would produce a smaller PT-OCT signal than the melanin in the RPE and choroid. It was thus necessary to use a higher photothermal laser power (8mW) to reliably detect the gold nanorods at physiologically relevant

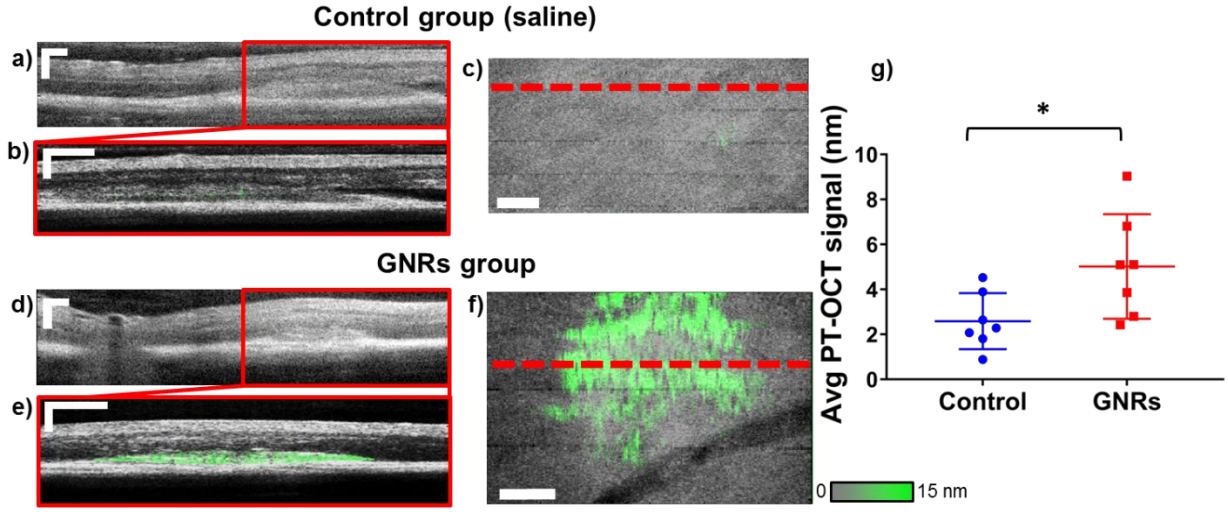

Fig. 4.4. *In vivo* PT-OCT of gold nanoparticles. (A, D) OCT B-scan of the retina showing an LCNV lesion (boxed area) in, respectively, a mouse of the control group and a mouse of the gold nanorods group. (B, E) OCT B-scan of the LCNV lesion (grayscale) with PT-OCT signal overlaid (green) in, respectively, a mouse of the control group and a mouse of the gold nanorods group. (C, F) 2D *en face* mean projection of the OCT (grayscale) and PT-OCT (green) data volume in a control mouse and a mouse injected with gold nanorods. The location of the B-scan shown on the left are indicated by the red dashed line. Scale bar 100μm. (G) Average PT-OCT signal normalized to the volume of the LCNV lesion for n=7 eyes per group. Mean with standard deviation shown. *p<0.05.

concentrations. An OCT B-scan of the retina can be seen for both experimental groups in Fig. 4.4a and 4.4d, with the LCNV lesion identified by the red boxed area. A PT-OCT scan was taken of the boxed area, which can be seen overlaid in green on top of the corresponding OCT B-scan (grayscale) in Fig. 4.4b and 4.4e (the control mouse has minimal PT-OCT signal). An *en face* image of the lesion is shown in Fig. 4.4c

and 4.4f, with the OCT signal in grayscale and the PT-OCT signal in green. The location of the B-scan shown on the previous panels is indicated by the dashed red line.

The average PT-OCT signal per pixel of the LCNV lesion for each experimental group is shown on Fig. 4.4g. We have found a statistically significant difference ($p<0.05$, Mann-Whitney U test) between the two experimental groups. This leads us to conclude that the increase in PT-OCT signal is due to the detection of gold nanorods present in the lesion. The control group is shown to have a non-zero PT-OCT signal, which is due to melanin in the RPE. As seen in Fig. 4.2c (blue series) the expected mean background signal (when excluding the RPE) is approximately 3.4nm for a photothermal laser power of 8mW. This result matches the levels of PT-OCT signal detected in the LCNV lesions in the control group, where the RPE is also excluded (Fig. 4.4g, control). The gold nanorods thus significantly increase the PT-OCT signal in the LCNV lesions above the expected background signal caused by melanin at this photothermal laser power level.

4.4 Discussion

PT-OCT is an emerging technique that adds functional contrast to traditional OCT imaging. It has been demonstrated *in vitro*[27], *ex vivo*[28] and *in vivo*[22] in the past on contrast agents such as gold nanoparticles[25] and melanin[29]. However, this was the first time that PT-OCT was demonstrated in the eye, even though OCT is commonly used for retinal imaging in eye research and is a standard of care in ophthalmology[1].

In this study, we first performed PT-OCT on cohorts of pigmented and albino mice to isolate the photothermal signal from melanin. We obtained a statistically significant increase in photothermal signal in pigmented mice, and the signal was located in depth at a retinal layer corresponding to the RPE and choroid. It was also observed that a photothermal laser power as low as 1mW would be sufficient, and even preferable, for PT-OCT studies of melanin distribution in the retina. This is a laser power that is routinely used in animal OCT studies without damage to the retina[21]. The detection of melanin using PT-OCT

could be important in the future since it is a naturally present contrast agent in the retina and its concentration and distribution across the retina are indicative of different disease states. For example, melanin variation across the retina is observed in melanoma and age-related macular degeneration[11]. Melanin distribution could be compared to OCT intensity image and OCT angiography without the need for contrast agents or image registration. Additionally, relative concentrations of melanin across the retina could be quantified since the PT-OCT signal is directly proportional to the concentration of absorbers[22]. Even though the RPE is known to be highly back-scattering[30], which increases the OCT signal, this change in signal is non-specific and difficult to mathematically relate to melanin concentration. PT-OCT could be an important complementary tool to understand specifically how melanin is distributed in the retina in three dimensions.

In the second part of this study, we used PT-OCT to detect the presence of gold nanorods after systemic injection of the contrast agent and passive accumulation in choroidal neovascular lesions. We detected a statistically significant increase in PT-OCT signal in the LCNV lesions in the experimental group that had been injected with gold nanorods, as compared to the control group which had levels of background signal compatible with what was detected during the melanin study. To our knowledge, this is the first time that an accumulation of gold nanorods in a neovascular lesion of the eye is detected *in vivo* using an OCT-based technology. It is usually difficult to distinguish the scattering gold nanorods against a highly scattering background, such as a lesion, from a traditional OCT intensity image[10]. However, PT-OCT can lock-in to the known frequency of the thermal oscillations created by the heated gold nanorods even when they are embedded in scattering tissue *in vivo*, as in this study.

Moving forward, *in vivo* detection of melanin in the eye using PT-OCT would allow for a dye-free, OCT-based method to detect and quantify melanin distribution in the eye. This method could be readily adopted by researchers currently studying the retina for both basic science applications, and the evaluation of new diagnostic and treatment methods. In turn, *in vivo* detection of gold nanorods in the eye using PT-OCT opens the door to molecular imaging using functionalized gold nanorods, and *in vivo* studies to

characterize the biodistribution of targeted gold nanorods in the eye. For example, intravitreal injections of gold nanoparticles have been investigated inhibition of vascular endothelial growth factor (VEGF) in the eye[5], but no studies have evaluated their potential following systemic injections. PT-OCT would provide *in vivo* information about the distribution of gold nanoparticles in the eye and offer complimentary information to the current standards, INAA and ICP-MS, which both require *ex vivo* samples and are labor intensive.

In conclusion, we have demonstrated PT-OCT in the eye for the first time and have detected a signal from an endogenous contrast agent, melanin, and an exogenous contrast agent, gold nanorods, *in vivo* in mice.

4.5 Methods

4.5.1 Gold nanorod synthesis

Carboxyl-functionalized polyethylene glycol (PEG)-coated-gold nanorods with peak absorption of 750 nm (diameter: 10nm, length: 35nm) were purchased from Nanopartz (C12-10/750-TC-50, Loveland, USA). To achieve functionalization we utilized 1-Ethyl-3-(3-dimethylaminopropyl) carbodiimide (EDC)-mediated crosslinking of the carboxyl moiety attached to the polymer surface to a primary amine of purified rat IgG antibody[31]. This reaction occurred in the presence of N-hydroxysulfosuccinimide (sulfo-NHS) in order to increase its efficiency. Specifically, 10^{12} GNRs were allowed to react for 2 hours at room temperature with EDC and s-NHS at a 10x and 25x respective concentration relative to the surface carboxyl groups in 1mL of DI water. The solution was then centrifuged at 18,000g for 45 minutes and the nanorods resuspended in DI water 3 times prior to the addition of a 50-fold molar overconcentration of purified rat IgG antibody. This mixture was allowed to react for 2 hours at room temperature. We then purified the functional nanorods via three additional rounds of centrifugation at 18,000g for 45 minutes followed by resuspension in isotonic PBS prior to intravenous injection. Since the gold nanorods were untargeted, a purified rat IgG antibody (Thermo Fisher Scientific, Waltham, USA) with no known reactivity to murine

antigens was used. Unreacted antibody was purified in order to assess the yield of the coupling reaction, which was approximately 20 percent.

4.5.2 Animal preparation and imaging

All procedures adhered to rules governing animal experimentation issued by Vanderbilt University Animal Care and Use and all experimental protocols were approved by the Vanderbilt Institutional Animal Care and Use Committee. Albino (BALB/c) and wild-type (C57BL/6) mice aged 8-10 weeks were used for these experiments. No randomization was used to separate wild-type mice between control and gold nanorods injected groups. The number of eyes imaged was chosen based on previous *in vivo* PT-OCT experiments[25] and previous experiments using the LCNV model[10]. For all procedures, animals were anesthetized using isoflurane administration (2-5% in air) via nose cone. Pupils were dilated with phenylephrine (2.5%) and atropine sulfate (1%). Proparacaine (0.5%) was applied for corneal anesthesia. GenTeal lubricant eye gel (Alcon, Hünenberg, Switzerland) was applied to prevent corneal dryness. For the C57BL/6 mice used in the laser-induced choroidal neovascularization model[24], laser photocoagulation was performed using a laser system (Carl Zeiss Meditec, Jena, Germany) with a solid-state laser (Coherent, Santa Clara, CA) at 532nm, 100mW power, 0.1 second pulse duration, and 100μm spot size. Four lesions placed concentrically about the optic nerve head were created in each eye, carefully avoiding major blood vessels. Five days following lasering, white-light fundoscopy was performed using a Micron III (Phoenix Research Laboratories, Pleasanton, USA), in order to assess lesions. PT-OCT imaging was performed on the same day. Gold nanorods were administered via tail-vein injection 6 hours prior to PT-OCT imaging for the gold nanorods experimental group, and saline was administered in the same way to the control group. Each injection contained 100μL of gold nanorods solution at 1.66nM (100μL injection of saline for control). PT-OCT was performed for one lesion per eye while the mouse was under anesthesia. An electric heating blanket with temperature feedback probe was used to maintain the body temperature of the animal during imaging. For the melanin detection study, all eyes imaged were included in the analysis.

For the gold nanorods study, eyes with an LCNV lesion of total area >40,000 pixels were included to insure greater uniformity between replicates.

4.5.3 Instrumentation and signal analysis

A spectral domain OCT system (Bioptigen Inc, 10 kHz acquisition rate) was modified for PT-OCT imaging. Using a 50:50 fiber coupler, the light from a super luminescent diode (Superlum, λ_0=860 nm, 40 nm bandwidth) was combined to the light of a Titanium:Sapphire laser (Coherent, λ=750 nm) that was amplitude-modulated (square wave, f_0=500 Hz, 50% duty cycle) using an acousto-optic modulator (AOM, Brimrose). The light was then split between the reference and sample arm of the system using the 50:50 fiber coupler. A circulator (AC Photonics) was used to direct the backscattered light to a 2048 pixels CCD, and a filter was used to block λ<800nm light to reach the detector. The SLD power at the sample was 2mW and the Ti:Saph power to the sample was varied between 0-10mW for the melanin experiment, and fixed at 8mW for the gold nanorods experiment. A telecentric lens for mice retinal imaging (Bioptigen) was used to focus the light. The resulting system had an 8.1μm axial resolution in air and approximately 6μm in the retina[32]. For each PT-OCT A-scan, 700 repeated temporal OCT A-scans (M-mode imaging) were acquired. After image acquisition, the data was analyzed using MATLAB. The data was first resampled from wavelength to wavenumber, dispersion corrected[33] and background subtracted. A Chirp-Z transform was used to convert the wavenumber dimension into spatial domain. At each depth over the 700 repeated A-scans, the first temporal derivative of the phase data was found. It was observed that 700 repeated A-scans lead to good signal sensitivity (~0.5nm) and that a higher number of repeated A-scans did not further improve the sensitivity. A Fourier transform was used to convert the phase oscillations from the time domain to the frequency domain and the peak corresponding to the Ti:Saph modulation frequency (500 Hz) was identified. The amplitude of the peak was taken to be the PT-OCT signal intensity and the amplitude away from the peak was taken to be the noise floor. Final images were constructed by subtracting the noise floor from the signal intensity. The resulting PT-OCT signal is expressed as a change in optical path length, in units of nanometers. The optical path length variations are caused by the local changes in

index of refraction and elastic expansions of the tissue due to the cyclical variations in temperature. A more detailed description of PT-OCT signal and of the data-processing algorithm is found in Tucker-Schwartz et al.[22].

4.5.4 Image correction protocol

To determine if PT-OCT is able to detect gold nanorods accumulating in LCNV lesions after a systemic injection, the RPE and choroid had to be excluded from our image analysis for the subsequent experiments. This was done so that variations across eyes in melanin distribution would not affect the PT-OCT signal detected in the gold nanorods experiment. Illustrations of the image analysis process can be seen in Fig. 4.5.

First the OCT and PT-OCT B-scans that were acquired simultaneously are corrected for breathing artifacts (Fig 4.5a-d). An algorithm adapted from Guizar-Sicairos *et al.*[34] is used to translate independently each OCT A-scan in depth so they align best with the geometry of the retina and the effects of breathing are removed. The algorithm uses a standard OCT volume scan acquired earlier during the experiment (fast acquisition, no oversampling over time, no breathing artifact) as a reference image. The

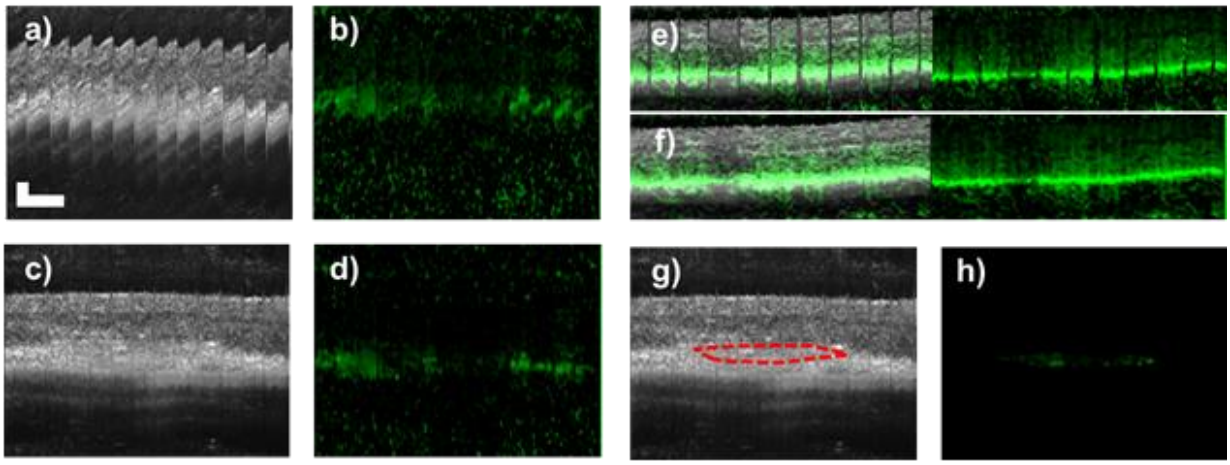

Fig. 4.5. Image correction protocol. (A) OCT B-scan with breathing artifacts and (B) corresponding PT-OCT B-scan. (C) OCT B-scan and (D) corresponding PT-OCT B-scan after breathing artifact correction using image registration. (E) OCT and PT-OCT B-scan with missing A-scans due to breathing artifact. (F) OCT and PT-OCT B-scan after artifact correction using one-dimensional linear interpolation. (G) Manual selection of the LCNV lesion based on the OCT corrected image. (H) Resulting masked PTOCT signal. Scale bar: 100μm.

same vertical offset used to correct an individual A-scan on the OCT image is applied to the corresponding A-scan on the PT-OCT image, effectively correcting it too. This reduces the up and down motion of the breathing artifacts but does not re-establish missing A-scans due to breathing (see Fig. 4.5e). One-dimensional linear interpolation is used to correct those regions (see Fig. 4.5f).

Once the breathing artifacts have been corrected, the LCNV lesion is selected manually on each OCT B-scan based on the tissue structure (Fig. 4.5g). The selected regions of each PT-OCT scan (Fig. 4.5h) were used for the remaining analysis. The experimental group was known to the user during manual selection (no blinding) but the selection was done based on the tissue structure shown on the OCT B-scan alone, without any PT-OCT signal shown. The PT-OCT signal was calculated only after all manual selection had been performed for all experimental groups.

4.5.5 Damage to the retina

Based on the photothermal laser wavelength (750nm), illumination time (2ms per sample location) and power (up to 8mW), it was determined that there was a risk of thermal damage to the retina if the temperature rose by 10°C or more at any time during our experiment[35]. The temperature distribution was modeled[20] based on the experimental A-scans that we have obtained at high laser powers, and it was determined that at no point during the experiment was the retina at 10°C or more above basal temperature. The photothermal laser is pulsed (100fs) and considered quasi-CW for the purpose of the experiment. In phantoms, we have not observed a deterioration of the photothermal signal during repeated exposition of melanin phantoms or gold nanorods phantoms to the photothermal laser (tested with powers up to 40mW). For this reason, we do not expect any significant damages to the melanin or the gold nanorods by the pulsed laser. It is possible for the pulse laser to have caused mechanical damages to the retina, but none was observed in an OCT B-scan of the mouse retina post-experiment. We are not aware of a pathway leading to photochemical damage at the cellular or molecular levels for a sample exposed to near infrared light[35]. By themselves, gold nanorods have not shown signs of toxicity to the retina[16, 36]. Thus we do not expect

that permanent retinal damage was caused during the course of this experiment, but more studies would be required.

4.5.6 Significance test

Statistical significance for the increase in PT-OCT signal between pigmented and albino mice (Fig. 4.1) was based on the P-value (p=0.0022) obtained from a two-tailed Mann-Whitney U test. The Mann-Whitney U test is the non-parametric equivalent to the Student's t-test. A non-parametric test was used because of the low number of samples (n = 6 eyes from three different mice in each experimental group). Other assumptions of the Mann-Whitney U test were met. Statistical significance for the increase in PT-OCT signal between 1mW and 0mW groups (Fig. 4.2d) and between control and mice injected with gold nanorods (Fig. 4.4) was also determined using a two-tailed Mann-Whitney U test. Respective p-values of p=0.0087 and 0.0262 were obtained. For the difference between 1mw and 0mW, n=6 eyes from 3 different mice were used. For the comparison between gold nanorods and control groups, n=7 eyes were used from 4 different mice in each experimental group.

4.6 Acknowledgements

We thank Jason R. Craft and Imam Uddin for their help with animal handling and preparation. This study was supported by the following grants: NIH/NCI R01 CA205101, R01 CA185747, NSF CBET-1554027, NIH/NEI R01 EY023639-02, R01 EY023397-03 and R01 EY07533 (JSP), The Carl Marshall Reeves & Mildred Almen Reeves Foundation, Inc., and an Unrestricted Grant from Research to Prevent Blindness, Inc. (JSP)

4.7 References

[1] A. M. Zysk, F. T. Nguyen, A. L. Oldenburg, D. L. Marks, and S. A. Boppart, "Optical coherence tomography: a review of clinical development from bench to bedside," *Journal of biomedical optics,* vol. 12, no. 5, pp. 051403-051403, 2007.

[2] Y. Kanagasingam, A. Bhuiyan, M. D. Abràmoff, R. T. Smith, L. Goldschmidt, and T. Y. Wong, "Progress on retinal image analysis for age related macular degeneration," *Progress in retinal and eye research,* vol. 38, pp. 20-42, 2014.

[3] C. V. Regatieri, L. Branchini, J. Carmody, J. G. Fujimoto, and J. S. Duker, "Choroidal thickness in patients with diabetic retinopathy analyzed by spectral-domain optical coherence tomography," *Retina,* vol. 32, no. 3, p. 563, 2012.
[4] I. I. Bussel, G. Wollstein, and J. S. Schuman, "OCT for glaucoma diagnosis, screening and detection of glaucoma progression," *British Journal of Ophthalmology,* vol. 98, pp. 15-19, 2014.
[5] J. H. Kim, M. H. Kim, D. H. Jo, Y. S. Yu, T. G. Lee, and J. H. Kim, "The inhibition of retinal neovascularization by gold nanoparticles via suppression of VEGFR-2 activation," *Biomaterials,* vol. 32, no. 7, pp. 1865-1871, 2011.
[6] K. H. Kim *et al.*, "Monitoring mouse retinal degeneration with high-resolution spectral-domain optical coherence tomography," *Journal of vision,* vol. 8, no. 1, pp. 17-17, 2008.
[7] S. J. Chiu, J. A. Izatt, R. V. O'Connell, K. P. Winter, C. A. Toth, and S. Farsiu, "Validated automatic segmentation of AMD pathology including drusen and geographic atrophy in SD-OCT images," *Investigative ophthalmology & visual science,* vol. 53, no. 1, p. 53, 2012.
[8] E. Götzinger *et al.*, "Retinal pigment epithelium segmentation by polarization sensitive optical coherence tomography," *Optics express,* vol. 16, no. 21, 2008.
[9] A. M. Gobin, M. H. Lee, N. J. Halas, W. D. James, R. A. Drezek, and J. L. West, "Near-infrared resonant nanoshells for combined optical imaging and photothermal cancer therapy," *Nano letters,* vol. 7, no. 7, pp. 1929-1934, 2007.
[10] D. Sen *et al.*, "High-resolution contrast-enhanced optical coherence tomography in mice retinae," *Journal of biomedical optics,* vol. 21, no. 6, pp. 066002-066002, 2016.
[11] V. L. Bonilha, "Age and disease-related structural changes in the retinal pigment epithelium," *Clin Ophthalmol,* vol. 2, no. 2, pp. 413-424, 2008.
[12] Y. Diebold and M. Calonge, "Applications of nanoparticles in ophthalmology," *Progress in retinal and eye research,* vol. 29, no. 6, pp. 596-609, 2010.
[13] A. Zerda *et al.*, "Optical coherence contrast imaging using gold nanorods in living mice eyes," *Clinical & experimental ophthalmology,* vol. 43, no. 4, pp. 358-366, 2015.
[14] M. G. Sandrian *et al.*, " Inflammatory response to intravitreal injection of gold nanorods," *British Journal of Ophthalmology,* vol. 96, no. 12, pp. 1522-1529, 2012.
[15] A. Hayashi, A. Naseri, M. E. Pennesi, and E. de Juan Jr, "Subretinal delivery of immunoglobulin G with gold nanoparticles in the rabbit eye," *Japanese journal of ophthalmology,* vol. 53, no. 3, pp. 249-256, 2009.
[16] J. H. Kim, J. H. Kim, K. W. Kim, M. H. Kim, and Y. S. Yu, "Intravenously administered gold nanoparticles pass through the blood-retinal barrier depending on the particle size, and induce no retinal toxicity " *Nanotechnology,* vol. 20, no. 50, p. 505101, 2009.
[17] A. C. Amrite, H. F. Edelhauser, S. R. Singh, and U. B. Kompella, "Effect of circulation on the disposition and ocular tissue distribution of 20 nm nanoparticles after periocular administration," *Molecular vision,* vol. 14, pp. 150-160, 2008.
[18] D. W. Grainger, "Nanotoxicity assessment: all small talk?," *Advanced drug delivery reviews,* vol. 61, no. 6, p. 419, 2009.
[19] N. Khlebtsov and L. Dykman, "Biodistribution and toxicity of engineered gold nanoparticles: a review of in vitro and in vivo studies," *Chemical Society Reviews,* vol. 40, no. 3, pp. 1647-1671, 2011.
[20] M. Lapierre-Landry, J. M. Tucker-Schwartz, and M. C. Skala, " Depth-resolved analytical model and correction algorithm for photothermal optical coherence tomography," *Biomedical Optics Express,* vol. 7, no. 7, pp. 2607-2622, 2016.
[21] K. H. Kim *et al.*, "Monitoring mouse retinal degeneration with high-resolution spectral-domain optical coherence tomography," *Journal of vision,* vol. 8, no. 1, p. 17, 2008.
[22] J. M. Tucker-Schwartz, T. A. Meyer, C. A. Patil, C. L. Duvall, and M. C. Skala, "In vivo photothermal optical coherence tomography of gold nanorods contrast agents," *Biomedical Optics Express,* vol. 3, no. 11, pp. 2882-2895, 2012.

[23] M. E. Pennesi, M. Neuringer, and R. J. Courtney, "Animal models of age related macular degeneration," *Molecular aspects of medicine,* vol. 33, no. 4, pp. 487-509, 2012.
[24] A. Giani *et al.*, "In vivo evaluation of laser-induced choroidal neovascularization using spectral-domain optical coherence tomography," *Investigative ophthalmology & visual science,* vol. 52, no. 6, pp. 3880-3887, 2011.
[25] J. M. Tucker-Schwartz, K. R. Beavers, W. W. Sit, A. T. Shah, C. L. Duvall, and M. C. Skala, "In vivo imaging of nanoparticles delivery and tumor microvasculature with multimodal optical coherence tomography," *Biomedical optics express,* vol. 5 no. 6, p. 1731, 2014.
[26] H. Kimura, T. Yasukawa, Y. Tabata, and Y. Ogura, "Drug targeting to choroidal neovascularization," *Advanced drug delivery reviews,* vol. 52, no. 1, pp. 79-91, 2001.
[27] M. C. Skala, M. J. Crow, A. Wax, and J. A. Izatt, "Photothermal optical coherence tomography of epidermal growth factor receptor in live cells using immunotargeted gold nanospheres," *Nano letters,* vol. 8, pp. 3461-3467, 2008.
[28] C. Zhou *et al.*, "Photothermal optical coherence tomography in ex vivo human breast tissues using gold nanoshells," *Optics letters,* vol. 35, pp. 700-702, 2010.
[29] S. Makita and Y. Yasuno, "In vivo photothermal optical coherence tomography for non-invasive imaging of endogenous absorption agents " *Biomedical optics express,* vol. 6, no. 5, pp. 1707-1725, 2015.
[30] W. Drexler, U. Morgner, R. K. Ghanta, F. X. Kärtner, J. S. Schuman, and J. G. Fujimoto, "Ultrahigh-resolution ophthalmic optical coherence tomography," *Nature medicine,* vol. 7, no. 4, pp. 502-507, 2001.
[31] G. T. Hermanson, in *Bioconjugate techniques*London: Elsevier/AP, 2013, pp. 557-560.
[32] "On the refractive index of the retina," *Acta Physiologica Scandinavica,* vol. 13, no. 1-2, pp. 130-149, 1947.
[33] M. Wojtkowski, V. J. Srinivasan, T. H. Ko, J. G. Fujimoto, A. Kowalczyk, and J. S. Duker, "Ultrahigh-resolution, high-speed, Fourier domain optical coherence tomography and methods for dispersion compensation," *Optics express,* vol. 12, no. 11, pp. 2404-2422, 2004.
[34] M. Guizar-Sicairos, S. T. Thurman, and J. R. Fienup, "Efficient subpixel image registration algorithms," *Optics Letters,* vol. 33, pp. 156-158, 2008.
[35] R. D. Glickman, "Phototoxicity to the retina: mechanisms of damage," *International Journal of Toxicology,* vol. 21, no. 6, pp. 473-490, 2002.
[36] S. J. Bakri, J. S. Pulido, P. Mukherjee, R. J. Marler, and D. Mukhopadhyay, "Absence of histologic retinal toxicity of intravitreal nanogold in a rabbit model," *Retina,* vol. 28, no. 1, pp. 147-149, 2008.

CHAPTER 5

Imaging melanin distribution in the zebrafish retina using photothermal optical coherence tomography

M. Lapierre-Landry, A. L. Huckenpahler, B. A. Link, R. F. Collery, J. Carroll, M. C. Skala, "Imaging melanin distribution in the zebrafish using photothermal optical coherence tomography," *Translational Vision Science and Technology*, 2018.

5.1 Abstract

This project demonstrates and validates that photothermal optical coherence tomography (PT-OCT) can image melanin in the retinal pigment epithelium (RPE) and can observe light-driven melanosome translocation in the zebrafish retina. A commercial spectral domain OCT system was modified to perform both OCT and PT-OCT. Four adult tyrosinase-mosaic zebrafish with varying levels of melanin expression across their retina were imaged and the PT-OCT signal for pigmented and non-pigmented regions were compared. Wild type dark-adapted (n=11 fish) and light-adapted (n=10 fish) zebrafish were also imaged with OCT and PT-OCT. Longitudinal reflectivity and absorption profiles were generated from B-scans to compare the melanin distribution between the two groups. A significant increase in PT-OCT signal ($P<0.0001$, Student's t-test) was observed in pigmented regions of interest (ROI) compared to non-pigmented ROIs in the tyrosinase-mosaic zebrafish, which confirms the PT-OCT signal is specific to melanin in the eye. A significant increase in PT-OCT signal intensity ($P<0.0001$, Student's t-test) was also detected in light-adapted wild-type zebrafish group compared to the dark-adapted group. Additionally, light-adapted zebrafish display more distinct melanin banding patterns than dark-adapted zebrafish in PT-OCT B-scans. In conclusion, PT-OCT can detect different levels of melanin absorption and characterize pigment distribution in the zebrafish retina, including intracellular changes due to light-driven melanosome translocation within the RPE. PT-OCT could quantify changes in pigmentation that occur in retinal diseases. The functional information provided by PT-OCT may also enable a better understanding of the anatomical features within conventional OCT images.

5.2 Introduction

Optical coherence tomography (OCT) is a standard imaging technique that provides high resolution, depth-resolved images of different tissue layers without the need for contrast agents. It is used both in clinical and research settings to non-invasively detect, monitor, and study multiple eye conditions *in vivo*, either in patients or animal models[1]. As OCT becomes more widely used to monitor retinal diseases, it is important to correctly identify the anatomic features that correspond to OCT image features for the human retina and multiple animal models[2]. Previous efforts to label OCT image features have relied on comparisons to histology[2-4]. However, the relative thickness and appearance of retinal layers is not always conserved between histology and OCT images, which complicates the labeling process[2]. Additionally, the main source of contrast in OCT is tissue backscattering, a property that cannot be directly compared to cell morphology in fixed samples. As a result, there is still controversy regarding the proper labeling of some retinal structures on OCT scans, particularly the bands associated with the photoreceptors and retinal pigment epithelium (RPE)[4, 5].

One of the major scattering sources in the retina is melanin, which is located in the RPE and choroid. Retinal melanin varies with age and between individuals, and pigmentation changes are also associated with diseases such as age-related macular degeneration (AMD)[6] and retinitis pigmentosa[7]. In AMD, hyperpigmentation which may be due to RPE cells dysfunction, followed by hypopigmentation due to RPE cells loss are observed in geographic atrophy. These pigmentation changes in the RPE are thought to happen before dysfunction and death of the photoreceptors, and thus could be predictive of disease progression[6, 8]. Melanin is a major contributor to the appearance of the OCT RPE band, and by extension the surrounding bands corresponding to the photoreceptors and Bruch's membrane[9, 10]. An independent, validated method to image the melanin would allow researchers to quantify changes in pigmentation in the RPE and better understand how melanin affects OCT images, which could lead to a better understanding of diseases for researchers and better diagnosis and monitoring tools for clinicians.

Multiple imaging techniques have been developed to detect retinal melanin. Near-infrared autofluorescence (excitation at 787nm) can be used to detect melanin in the RPE and choroid but is limited to 2D *en face* imaging, and quantifying melanin in these images is not currently possible[11-13]. Photoacoustic microscopy (PAM) has also been used to image and quantify the distribution of melanin in the RPE and choroid[14]. Due to its low axial resolution PAM has mostly been used to create 2D *en face* images, but recent improvements have been made to distinguish the RPE from the choroid and produce depth-resolved images[15]. Functional OCT techniques such as polarization-sensitive (PS-OCT)[16] and photothermal OCT (PT-OCT)[17, 18] have also been used to detect retinal melanin. Since they are based on the OCT signal, both modalities can produce 3D images of the retinal melanin distribution with axial and transverse resolution similar to OCT. Additionally, these images of melanin distribution are automatically co-registered to corresponding OCT intensity images showing retinal morphology. However, PS-OCT and PT-OCT use different contrast mechanisms. PS-OCT measures the depolarization of backscattered light and has been used to detect the presence of melanin in patients[19] and animal models[20], and to segment to RPE[21]. However, the degree of polarization uniformity measured with PS-OCT depends on the scattering properties of the sample, especially the size and shape of pigment granules, and does not decrease uniformly with respect to melanin concentration especially at high melanin concentrations[22]. This limits the ability of PS-OCT for quantitative measurements. Alternatively, PT-OCT detects melanin based on its absorption coefficient. PT-OCT could be used to directly image and quantify retinal melanin to disambiguate the OCT signal in regions of the retina such as the RPE where melanin is present.

In this study, PT-OCT was used to image the zebrafish eye for the first time. Zebrafish have a cone-rich retina which can be imaged with OCT[10, 23, 24]. Many genetically modified lines are also available[25]. Genetically modified zebrafish in which pigment synthesis is disrupted resulting in cells either expressing or not expressing melanin (“tyrosinase-mosaic”)[10] were used to image variations in pigmentation within the same eye. Additionally, melanosome translocation within the RPE cells due to

light- or dark-adaptation is a well-known phenomenon in wild-type zebrafish[26]. This specific and highly repeatable perturbation was used to image sub-cellular changes in pigment distribution. In summary, we demonstrate that the PT-OCT signal is specific to melanin and sensitive to different pigmentation levels and distribution in the zebrafish retina.

5.3 Methods

5.3.1 Instrumentation and signal analysis

A commercial spectral domain OCT system (Bioptigen, Durham, NC, Envisu R-2200, λ=860nm, 93nm bandwidth, 36kHz acquisition rate) was modified to perform PT-OCT imaging. A diode laser (Coherent Inc., Santa Clara, CA, λ=685nm) was added to the light path to provide photothermal excitation using a 50:50 fiber coupler. The diode laser was amplitude-modulated internally following a square wave of frequency f_0=500Hz, 50% duty cycle. From the 50:50 coupler the light was directed into the reference and sample arm. A wideband optical circulator (AC Photonics, Santa Clara, CA) was used to send the backscattered light to a spectrometer and 2048 pixels CCD. The OCT light source originally had a power of 0.7mW at the sample, but after the addition of the circulator, the power at the sample was reduced to 0.47mW. The peak power of the photothermal laser was varied between 0 and 4.3mW at the sample depending on the experiment. A mouse retina lens (Bioptigen) was used to focus the light onto the zebrafish retina. Data was acquired using the InVivoVue 2.4 software. Each PT-OCT A-scan was composed of 700 repeated scans over time (M-scan), with 400 A-scans per B-scan. A PT-OCT B-scan took approximately 7s to acquire. OCT volume scans and OCT line scans were also acquired for each eye. OCT volume scans were nominally 1.2mm x 1.2mm (500 A-scans/B-scans, 500 B-scans) and OCT line scans were nominally 1.2mm (400 A-scans/B-scan, 50 averaged B-scans). Both scan types were scaled according to the protocol in Huckenpahler *et al*[23].

Image analysis was performed following data collection using a custom MATLAB code previously described in Tucker-Schwartz *et al*[27]. The raw data was first resampled from wavelength to wavenumber,

dispersion corrected[28] and background subtracted. A Chirp-Z transform was then used to obtain the OCT magnitude and the phase signal as a function of depth. The time derivative of the phase signal over 700 M-scans was then taken at each depth, and a Fourier transform was performed to transition the phase signal from the time domain to the frequency domain. The PT-OCT peak signal is defined as the magnitude of the Fourier transformed phase signal at f_0=500Hz, which is the photothermal laser modulation frequency. The PT-OCT noise signal is defined as the average signal from 250-400Hz and 600-750Hz. The PT-OCT signal is taken to be the noise signal subtracted from the peak signal and is expressed in units of nanometers of optical path length change due to the increased temperature.

5.3.2 Zebrafish

Zebrafish studies were approved by the Institutional Animal Care and Use Committee at the Medical College of Wisconsin and conducted in accordance with the ARVO Statement for the Use of Animals in Ophthalmic and Vision Research. One-year-old adult wild-type (WT) and tyrosinase-mosaic zebrafish were used in this study. Tyrosinase-mosaic fish were created by injecting WT zebrafish embryos with CRISPR/Cas9 reagents targeting the *tyr* locus to cause mosaic gene inactivation and disruption of melanin synthesis as described in Wilk *et al*[10]. To determine if the PT-OCT signal is specific to melanin and observe how the PT-OCT signal changes as a function of the photothermal laser power, four mosaic zebrafish were imaged with OCT and PT-OCT while under anesthesia (Tricaine), using photothermal laser powers of 0, 1.8, 2.6 and 4.3mW. To study the melanosome translocation due to light, two WT light-adapted and two WT dark-adapted fish were first imaged as preliminary data. This experiment was then repeated with n=10 light-adapted zebrafish and n=11 dark-adapted zebrafish. The light-adapted fish were exposed to normal ambient light starting at 7am and imaged four hours later. Dark-adapted fish were protected from light overnight until the following day, when they were imaged in a dark room.

En face OCT images of the RPE were created by segmenting the RPE layer and averaging the OCT signal following an algorithm described in Huckenpahler *et al*[23]. OCT B-scans were created by averaging the OCT intensity signal from each PT-OCT B-scan (700 repeated A-scans at each pixel). Longitudinal

reflectivity profiles (LRP) were created by averaging the OCT signal using MATLAB over a 20-400 neighboring A-scans. Similarly, longitudinal absorption profiles (LAP) were created for the same regions by averaging the PT-OCT signal over neighboring A-scans. A median filter was used to reduce the noise of the OCT and PT-OCT images before creating the longitudinal profiles. In the case of the LRP and LAP created by averaging 400 A-scans, an image registration algorithm[29] was also used to align the retina over the entire B-scan before creating the longitudinal profiles.

5.3.3 Histology

The zebrafish were decapitated immediately after imaging while still under anesthesia and after gill movement had stopped. The heads were fixed in 4% paraformaldehyde overnight. Light and dark-adapted zebrafish had the eyes dissected from the head and embedded in paraffin for H&E histology. Tyrosinase-mosaic zebrafish had the eyes dissected from the head and the anterior segment removed prior to imaging the scleral aspect of the intact eye cup as in Wilk *et al*[10].

5.3.4 Statistical analysis

Statistical comparisons were done using Prism (GraphPad, La Jolla, CA). In all cases, an F-test was used to determine if the variances of two experimental groups were equal. A two-tailed, Student's t-test with unequal variance was used to compare the PT-OCT signal from pigmented and non-pigmented ROIs of the retina in mosaic zebrafish. Linear fits were also performed to determine if the PT-OCT signal in a given ROI was increasing linearly as a function of photothermal laser power. The origin y=0 was fixed for each fit since no PT-OCT signal should be detected when the photothermal laser is off (0mW). Three criteria were used to determine the quality of the fit and if the PT-OCT signal was proportional to laser power: the slope, the coefficient of determination, and the sum of squared errors. First, fits with a slope smaller than -0.1 were rejected since a positive relationship is predicted by theory[27]. Second, the coefficient of determination R^2 and the sum of squared residuals (SSR) were obtained as followed:

$$SSR = \sum_i (y_i - f_i)^2 \quad (5.1)$$

$$R^2 = 1 - \frac{SSR}{\sum_i (y_i - \bar{y})^2} \quad (5.2)$$

where y_i are the experimental PT-OCT values, f_i are the values predicted by the linear fit, and $\bar{y}$ is the mean experimental value. As seen in Eq. 5.2, R^2 is not an appropriate measure of the quality of the fit in cases where the PT-OCT signal remains zero as the power increases, which is expected if no pigment is present in the ROI ($y_i - \bar{y} \approx 0$). For this reason, the quality of the fit was determined to be acceptable if $R^2>0.5$, or SSR<1 in cases where $R^2<0.5$.

In the second part of this study, a two-tailed Student's t-test with equal variance was used to compare the average PT-OCT signal from dark-adapted fish (n=11) and light-adapted fish (n=10). A Student's t-test with equal variance was also used to compare the power spectrum amplitude of the dark-adapted zebrafish and light-adapted zebrafish at two spatial frequencies ($1/\Delta x_1$ = 1/23.6μm, $1/\Delta x_2$ = 1/11.8μm).

5.4 Results

5.4.1 PT-OCT signal in the RPE is specific to melanin

OCT and PT-OCT scans were acquired in all tyrosinase-mosaic fish. Pigmented and non-pigmented regions were identified based on the *en face* OCT image of the RPE, where pigmented regions had a higher OCT signal intensity compared to non-pigmented regions, as demonstrated in Wilk *et al*[10]. An example *en face* OCT image can be seen in Fig. 5.1a. To confirm the location of the pigmented and non-pigmented regions, the *en face* OCT image was compared to an *ex vivo* posterior view of the eyecup (Fig. 5.1b), which shows identical pigmentation patterns. Two example B-scans from the same eye can be seen in Fig. 5.1c where the PT-OCT signal has been overlaid onto the OCT signal. In this case, both PT-OCT B-scans were

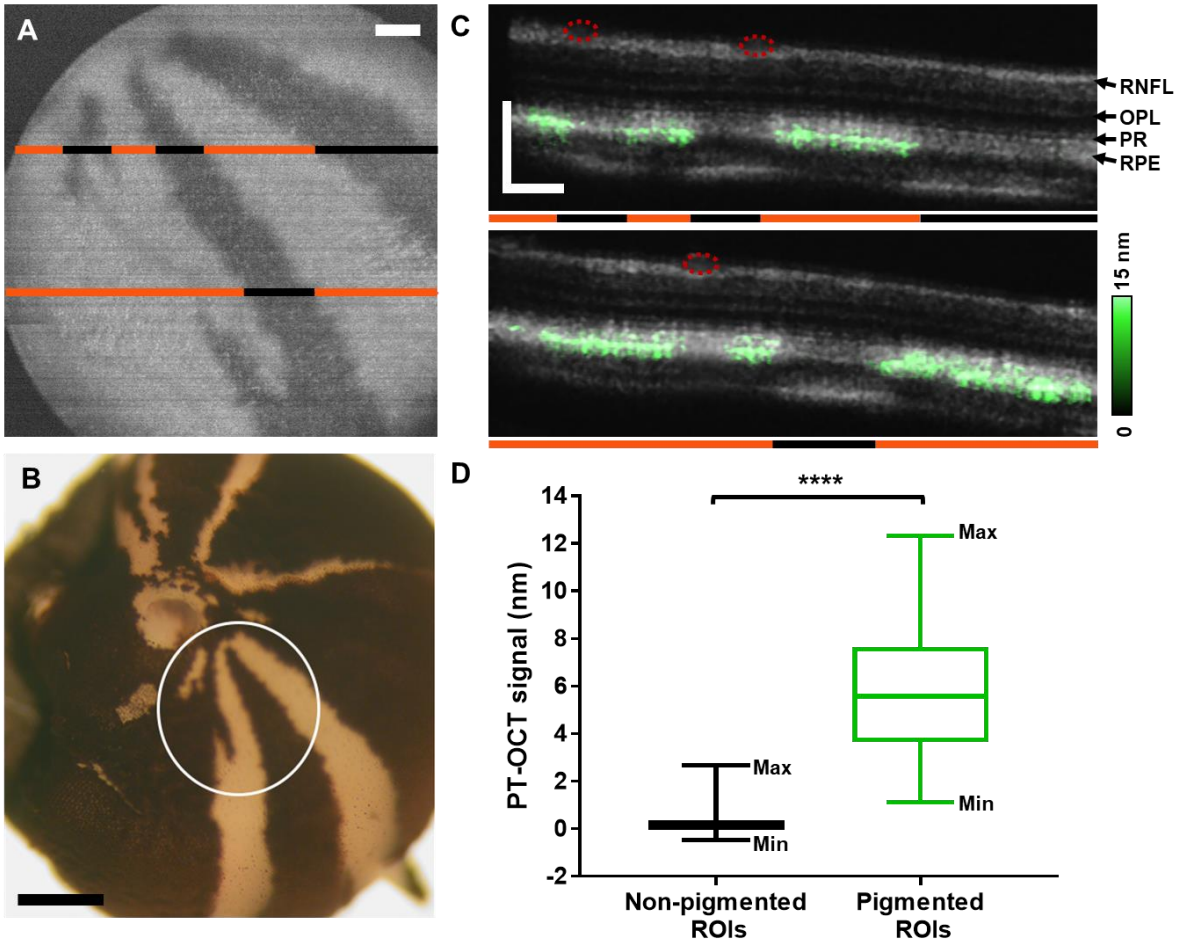

Fig. 5.1. PT-OCT of melanin in tyrosinase-mosaic zebrafish. (A) En face OCT image of the RPE showing the pigmentation pattern. Areas of pigment are hyperreflective (white) while non-pigmented areas are hyporeflective (dark). (B) Posterior view of the eye cup. White circle indicates field-of-view shown in (A) where areas of pigment are dark and non-pigmented areas are white. (C) OCT (gray) and PT-OCT (green, overlaid) B-scans of the retina. The location of the B-scans is indicated by the lines in (A). Orange lines denote pigmented areas and black lines denote non-pigmented areas. Red circles indicate presence of blood vessels. (D) Average PT-OCT signal for all non-pigmented and pigmented ROIs across n=5 eyes from 4 zebrafish. Each ROI is 10 A-scans wide. Whiskers on the box plot show minimum and maximum values for each distribution. ****P<0.0001 Student's t-test. RNFL, retinal nerve fiber layer; OPL, outer plexiform layer; PR, photoreceptors; RPE, retinal pigment epithelium. Scale bar: 100μm for OCT and 500μm for histology.

acquired using 2.85mW of photothermal laser power. The PT-OCT signal is localized to the band corresponding to the RPE and is only present in pigmented sections of the retina (orange lines, Figs. 5.1a, 5.1c). No PT-OCT signal is detected in non-pigmented regions (black lines, Figs. 5.1a, 5.1c), or regions of the retina below blood vessels (red circles, Fig. 5.1c). For all eyes (n=4 eyes from 4 fish), B-scans acquired using 4.3mW of photothermal laser power were divided in ROIs consisting of 10 neighboring A-scans. The average PT-OCT intensity was calculated for each ROI, and the ROI was classified as "pigmented" or "non-

pigmented" based on the OCT *en face* and OCT B-scan images. Blood vessels degrade the OCT phase signal, resulting in poor signal-to-noise ratio (SNR<1) and poor phase stability. Blood vessels can be identified based on morphology in OCT B-scans and *en face* views and as regions of negative PT-OCT signal (<-1nm) in PT-OCT B-scans. No PT-OCT signal can be reliably detected from regions below blood vessels since noise dominates over signal. ROIs below blood vessels were thus not included in this analysis. As seen in Fig. 5.1d, the PT-OCT signal in pigmented ROIs is significantly higher than for non-pigmented ROIs across all eyes ($P < 0.0001$, Student's t-test, n = 53 non-pigmented and n = 150 pigmented ROIs). The non-pigmented ROIs have an average signal of 0.23 ± 0.53nm (mean ± standard deviation), while the pigmented ROIs have an average signal of 5.71 ± 2.50nm. This significant increase in signal intensity demonstrates that PT-OCT is sensitive and specific to melanin expression in the zebrafish eye.

The distribution of PT-OCT signal in the pigmented ROIs has a high standard deviation (2.50nm) that does not match the phase stability of our system (<1nm). We hypothesize that the high variance in PT-OCT signal over all pigmented ROIs is not the result of a high uncertainty on the measurements, but likely a large range of absorption coefficients throughout the retina. Previous studies have confirmed that the PT-OCT signal is linearly proportional to the photothermal laser power and the local absorption coefficient of the sample[27]. Two perpendicular B-scans were thus acquired in each tyrosinase-mosaic eye at multiple photothermal laser powers to verify this linearity. As seen in Fig. 5.2a, no PT-OCT signal is detected when the photothermal laser is off. However, PT-OCT signal can be seen when the photothermal laser is set to 1.8mW and increases when the laser is set to higher powers (2.6mW and 4.3mW). As predicted by theory, the average PT-OCT signal increases linearly as a function of photothermal laser power for each ROI consisting of 10 averaged A-scans (Fig. 5.2b). Following the same model of the PT-OCT signal[27], the slope of the linear fit should be proportional to the melanin absorption in each ROI. High melanin absorption leads to a large slope (ROI #3, Fig. 5.2b), while non-pigmented areas have slopes equal or almost equal to zero (ROI #2, Fig. 5.2b). A melanin absorption value corresponding to the slope can thus be assigned to each ROI as seen in Fig. 5.2c. The melanin absorption values are normalized based on the highest slope

obtained in each eye. ROIs where the PT-OCT signal does not increase linearly nor remain stable as a function of power (R^2<0.5 and SSR>1, or slope<-0.1) are considered to not behave as predicted by theory, and thus no information about the melanin absorption can be inferred. These ROIs usually coincide with blood vessels, as seen in Fig. 5.2c. Melanin absorption values are displayed for four different eyes in Fig. 5.2d. Regions of low melanin absorption coincide with non-pigmented (dark) regions, while pigmented (light) regions have a large range of melanin absorption values. This experiment demonstrates the potential for quantitative imaging of melanin levels using PT-OCT.

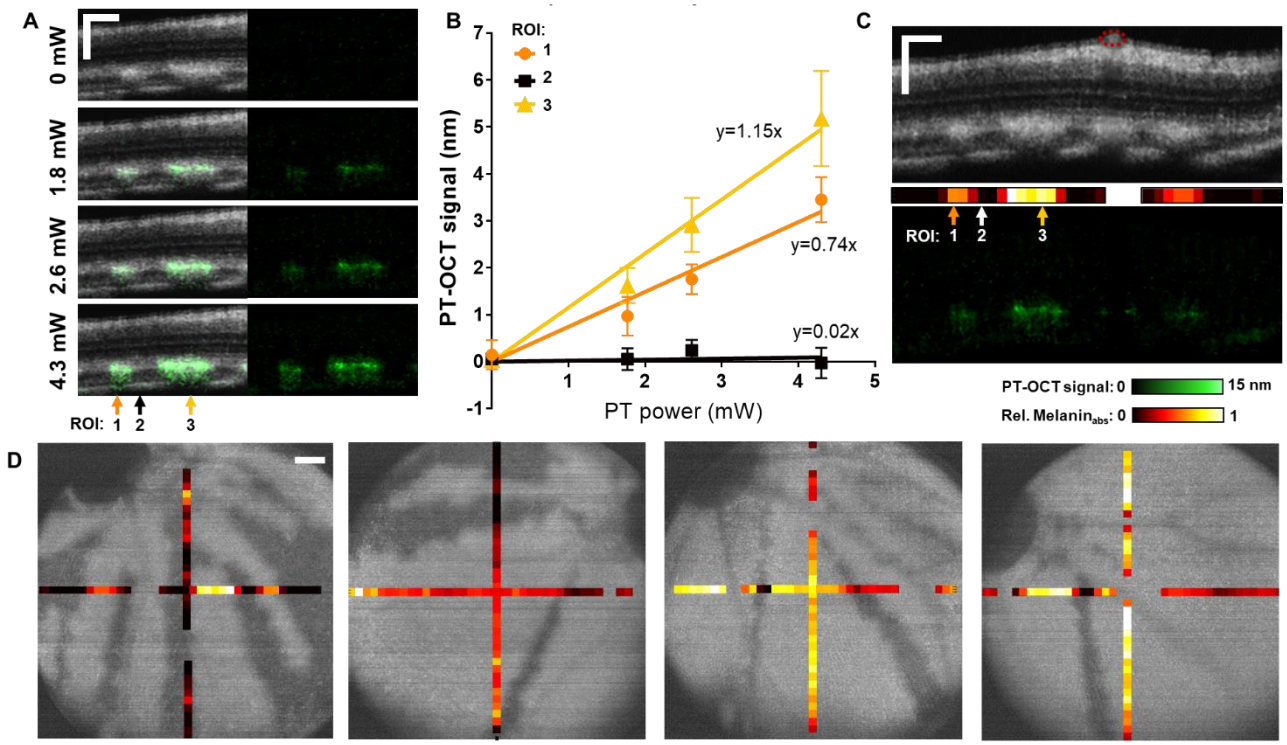

Fig. 5.2. PT-OCT signal of melanin increases linearly with power and is indicative of melanin concentration. (A) OCT B-scans (grayscale, left) of a tyrosinase-mosaic zebrafish retina with corresponding PT-OCT signal (overlaid in green on the left, signal alone on the right) collected at the same location for different photothermal laser powers (0-4.3 mW). Example ROIs #1, 2, and 3 indicated by arrows. Each ROI is composed of 10 adjacent A-scans. (B) Average PT-OCT signal for each ROI as a function of photothermal laser power. Error bars: standard error across 10 adjacent A-scans. Linear fits for each ROI #1, 2, and 3 with equations y=0.74x (R^2=0.96, SSR=0.24), y=0.02x (R^2=-0.35, SSR=0.05) and y=1.15x (R^2=0.98, SSR=0.23) respectively. (C) OCT B-scan (top), melanin absorption bar corresponding to the slopes extracted in (B) (middle) and corresponding PT-OCT B-scan (bottom), with location of ROIs indicated by arrows. Red circles indicate blood vessels. (D) Melanin absorption bar overlaid onto *en face* OCT images of the RPE for four different eyes. Melanin absorption is normalized for each eye. ROIs where the PT-OCT signal did not behave as predicted by theory (slope<-0.1, R^2<0.5 and SSR>1) are excluded for the melanin absorption (empty space). Scale bar: 100µm.

5.4.2 PT-OCT is sensitive to melanosome translocation

To visualize the axial distribution of melanin in the retina and to characterize the effect of melanin on the OCT signal, the PT-OCT signal as a function of depth was compared to the OCT signal at the same locations. OCT (Figs. 5.3a-c) and PT-OCT (Figs. 5.3d-f) B-scans were obtained in different zebrafish, and LRP and LAP (Figs. 5.3h-i) were computed by averaging 20 adjacent A-scans for each ROI (#1 and #2). From the LAP of the tyrosinase-mosaic zebrafish in Fig. 5.3h (green), some low background PT-OCT signal can be seen in the non-pigmented ROI (ROI #1, left) with a strong increase in PT-OCT signal due to melanin in the pigmented region (ROI #2, right). Additionally, the central PT-OCT peak corresponds to the RPE as

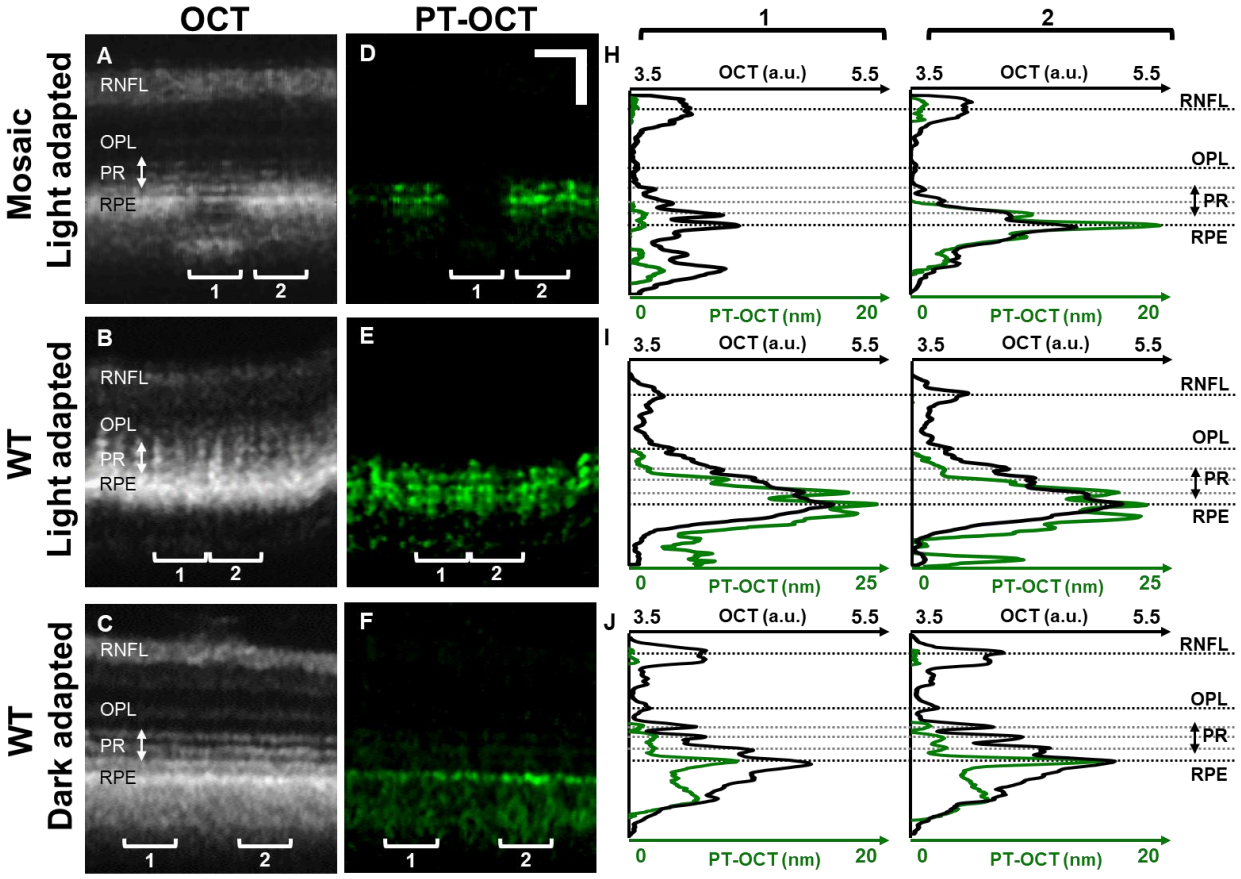

Fig 5.3. OCT and PT-OCT signal in the zebrafish retina as a function of depth. OCT (A, B, C) and PT-OCT (D, E, F) B-scans of light-adapted tyrosinase-mosaic zebrafish (top), wild-type light-adapted zebrafish (middle) and wild-type dark-adapted zebrafish (bottom) with longitudinal reflectivity profiles, or LRP (OCT, black) and longitudinal absorption profile, or LAP (PT-OCT, green) for each ROI (H, I, J) #1 (left) and 2 (right). Each ROI is averaged over 20 adjacent A-scans. In (H), ROI #1 is non-pigmented and ROI #2 is pigmented. RNFL, retinal nerve fiber layer; OPL, outer plexiform layer; PR, photoreceptors; RPE, retinal pigment epithelium. Scale bar: 50μm.

seen in the OCT image. There is also a second smaller PT-OCT peak at the junction between the photoreceptor layer and the RPE, and a third PT-OCT peak inside the RPE. Peaks of such intensities were not present in the non-pigmented region.

A WT light-adapted zebrafish was imaged (Figs. 5.3b, e, i) under the same conditions during a separate experiment, and a similar three-peak pattern can be seen in the PT-OCT signal (Fig. 5.3e, green), with the central peak of the LAP corresponding to the RPE and the anterior-most peak corresponding to the junction of the photoreceptors and RPE layer. This pattern was consistent and did not change with proximity to the optic nerve head.

Melanosome translocation within the RPE under different light conditions is a known phenomenon in zebrafish[26]. Under light-adaptation, melanosomes should migrate to the anterior part of the RPE cells, between the individual cone outer segments, and under dark-adaptation, the melanosomes should be segregated in the basal part of the RPE cells, further away from the cones. The previous experiment was repeated on a WT zebrafish that was dark-adapted for three hours. Our hypothesis was that under dark-adaptation, the melanosomes should be confined to the basal RPE and should not overlap with the photoreceptors. As seen in Figs. 5.3c and 5.3f, the PT-OCT signal peak obtained in the dark-adapted zebrafish corresponds to the RPE. The LAP (Fig. 5.3j) shows a single peak without side peaks, contrary to what is seen in the light-adapted zebrafish (Fig. 5.3h-i). For this experiment, the tyrosinase-mosaic zebrafish (Fig. 5.3a, d, h) was imaged with 4.72mW of photothermal laser power, while the WT light-adapted zebrafish and the WT dark-adapted zebrafish were image with respective powers of 2.61mW and 2.85mW, thus the PT-OCT signal amplitude could not be compared between zebrafish for this experiment.

The melanosome translocation experiment was repeated in 10 WT light-adapted zebrafish and eleven WT dark-adapted zebrafish of the same age (Fig. 5.4) to confirm the results seen in the preliminary data (Fig. 5.3). All zebrafish were imaged on the same day with the same photothermal laser power (2.07mW). The light-adapted zebrafish reliably display a three-band pattern (Fig. 5.4a) seen in previous experiments while the dark-adapted zebrafish do not have such pattern (Fig. 5.4b). LRPs and LAPs were created by averaging the entire OCT and PT-OCT B-scan (400 A-scans) for each zebrafish (Fig. 5.4c-d). B-scans without major blood vessels were chosen in each eye to optimize phase stability and the PT-OCT signal quality over the entire B-scan. As in the preliminary results, three peaks are seen in the PT-OCT signal for all light-adapted zebrafish (see five example zebrafish in Fig. 5.4c) where the central peak corresponds to the RPE and the anterior-most peak overlaps with a photoreceptor band. This pattern was not seen in any of the dark-adapted zebrafish (see five examples in Fig. 5.4d) where the PT-OCT signal is

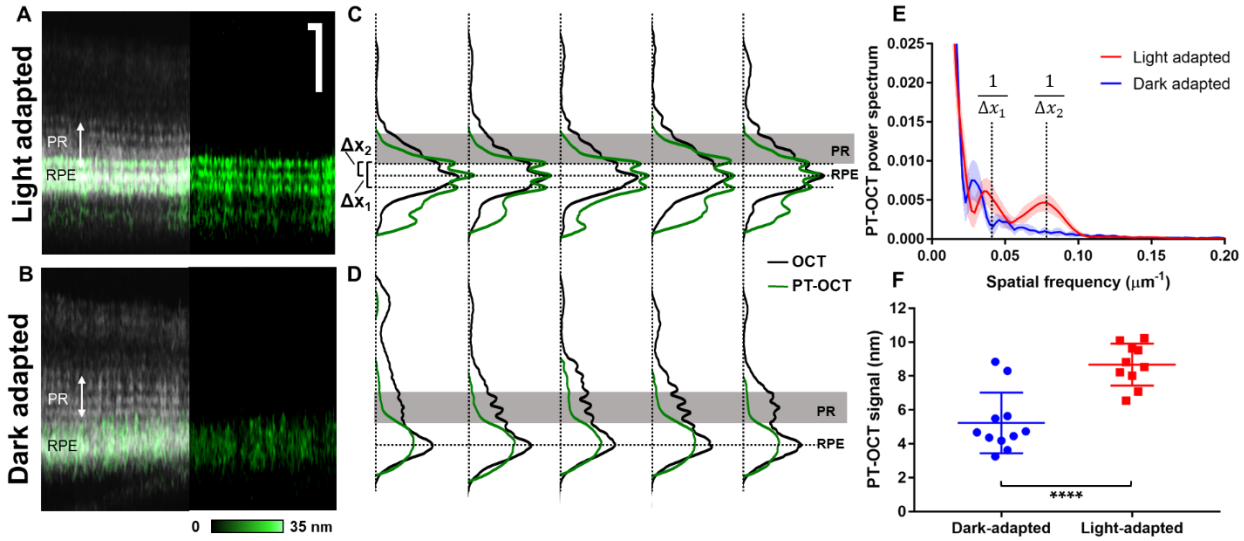

Fig. 5.4. PT-OCT signal in light-adapted and dark-adapted wild-type zebrafish. (A) OCT and PT-OCT B-scan of a light-adapted and (B) dark-adapted zebrafish (PT-OCT signal overlaid in green onto the OCT signal on the left, PT-OCT alone on the right). Scale bar: 50 μm. (C) LRP (OCT, black) and LAP (PT-OCT, green) for 5 light-adapted zebrafish and (D) five dark-adapted zebrafish. Horizontal dash lines correspond to the PT-OCT intensity peaks. Solid grey area indicates photoreceptor layer (PR). Δx_1 and Δx_2 indicates distances between PT-OCT peaks in the light-adapted zebrafish. RPE: Retinal pigment epithelium. (E) PT-OCT power spectrum obtained from the ten light-adapted (red) and eleven dark-adapted (blue) zebrafish. Solid line: mean; shaded region: standard deviation. The spatial frequencies corresponding to $1/\Delta x_1$ and $1/\Delta x_2$ are indicated. (F) Average PT-OCT signal per eye for all dark-adapted (blue) and light-adapted zebrafish (red). Error bars: standard deviation. ****P<0.0001 Student's t-test.

limited to the RPE and is composed of a single peak. A Fourier transform of the LAPs seen in Figs. 5.4c and 5.4d was performed to analyze the spatial frequency distribution (Fig. 5.4e) for all 21 zebrafish. Two regions of spatial frequency are significantly different between the light-adapted group and the dark-adapted group, which correspond to the distance between the anterior-most and posterior-most absorption bands ($\Delta x_1 = 23.6\mu m$), and between the anterior-most and middle bands ($\Delta x_2 = 11.8\mu m$) in light-adapted zebrafish (Fig. 5.4e). This spatial frequency analysis quantitatively highlights the differences in PT-OCT depth profiles between the light- and dark-adapted groups ($P=0.0001$ at $1/\Delta x_1$ and $P<0.0001$ at $1/\Delta x_2$, Student's t-test). Additionally, the average PT-OCT signal intensity per B-scan was calculated for both experimental groups (Fig. 5.4f). A significantly higher PT-OCT signal was detected in the light-adapted group compared to the dark-adapted group ($P<0.0001$, Student's t-test), which indicates higher melanin absorption in light-adapted zebrafish.

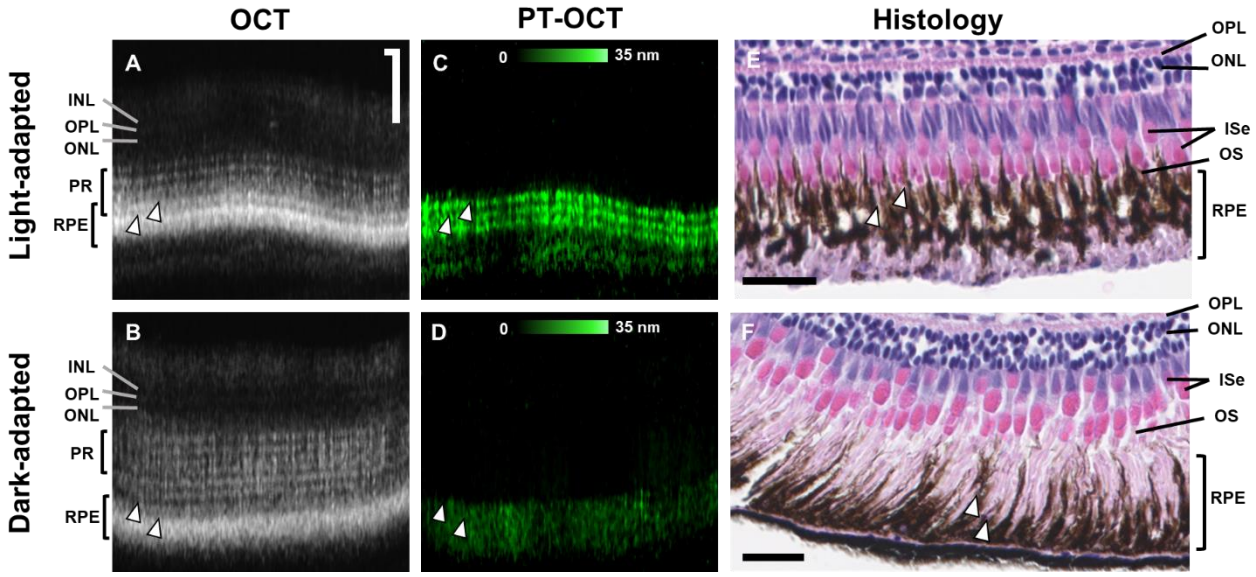

Fig 5.5. Melanosome migration observed in histology sections. (A, B) OCT and (C, D) corresponding PT-OCT B-scans with (E, F) corresponding H&E histology sections from the same animal for both light-adapted (A, C, E) and dark-adapted (B, D, F) zebrafish. White arrow heads indicate different structures where melanin is present (co-registered between images A & C, and B & D, approximate location for images E & F). Scale bar: 50 μm for OCT and PT-OCT images, 25 μm for histology. INL, inner nuclear layer; OPL, outer plexiform layer; ONL, outer nuclear layer; PR, photoreceptors; ISe, inner segment ellipsoid zone; OS, photoreceptor outer segment; RPE, retinal pigment epithelium.

Histology was performed on the zebrafish eyes to confirm melanosome translocation between the light and dark-adapted groups. Example OCT B-scans can be seen in Fig. 5.5a for the light-adapted

zebrafish and Fig.5.5b for the dark-adapted zebrafish, with corresponding PT-OCT B-scans in Figs. 5.5c and 5.5d. As seen previously the three-band pattern is present in the PT-OCT image of the light-adapted zebrafish (Fig. 5.5c), but not in the dark-adapted zebrafish (Fig. 5.5d). Histology was performed on the same zebrafish after imaging, and the corresponding histology sections are shown in Figs. 5.5e and 5.5f. As expected, the melanosomes in the light-adapted zebrafish have accumulated in the anterior part of the RPE cells and are surrounding the outer segments of the photoreceptors (Fig.5.5e, OS). There are almost no melanosomes left in the posterior part of the RPE cells, where nuclei are visible. In comparison, the melanosomes in the dark-adapted zebrafish have migrated to the basal part of the RPE cells, further away from the photoreceptors (Fig. 5.5f), which is expected in dark-adapted zebrafish[26]. These results confirm that melanosome translocation occurred as previously documented, and that our light-adapted group and dark-adapted group have different melanin distributions within the RPE. From this study, we conclude that PT-OCT is sensitive to differences in melanin distribution and absorption between light-adapted and dark-adapted zebrafish.

5.5 Discussion

PT-OCT is a functional OCT technique that detects optical absorbers such as gold nanoparticles[30] or indocyanine green[31] and has recently been demonstrated in the eye for the first time[32]. In this study, we used PT-OCT to image the distribution of melanin in the zebrafish retina. Melanin is naturally present in the RPE, and changes in retinal pigmentation are observed in multiple eye conditions, such as AMD,[6] albinism[33], and retinitis pigmentosa[34]. PT-OCT could provide a valuable imaging technique to quantify the distribution of melanin in the retina across different patients/diseases.

For this experiment, we first validated that the PT-OCT signal was specific to melanin by imaging tyrosinase-mosaic zebrafish. In the past, PT-OCT of melanin in the eye had only been tested by comparing WT mice to albino mice imaged during separate experiments[32]. Thus, the current study provided a more robust validation of PT-OCT sensitivity to melanin within a single retina. We further demonstrated that the

PT-OCT signal for pigmented ROIs increases linearly with laser power, as predicted by theory. Thus, the high variance in PT-OCT signal over all pigmented ROIs does not appear to be the result of a high uncertainty on the measurements, but likely a large range of absorption coefficients throughout the retina. This result indicates that PT-OCT could be used to quantify changes in melanin concentration within the eye.

Next, we characterized changes in melanin distribution as a function of depth within the retina. The most noticeable feature observed in the PT-OCT signal is the three-band pattern that was reliably seen in light-adapted zebrafish across different experiments, zebrafish cohorts (WT and tyrosinase-mosaic), and photothermal laser powers. This three-band pattern was never seen in dark-adapted fish. We also detected an increase in PT-OCT signal intensity in the light-adapted zebrafish group compared to the dark-adapted group even though dark-adaptation alone is unlikely to cause changes in total melanin amounts and both groups were imaged at the same time of the day[35]. In the zebrafish, light-based melanosome migration is thought to control the exposure of the photoreceptors to incoming light[26]. During light-adaptation melanosomes surround the photoreceptors to absorb some of the excessive incoming light and reduce bleaching, while during dark-adaptation the opposite situation takes place and melanosomes migrate away from the photoreceptors to maximize their exposure to light. The same behavior was seen in our PT-OCT measurements: during light-adaptation, more light was absorbed by the melanin and converted into heat, which increased the PT-OCT signal, while during dark-adaptation, more light was absorbed by the photoreceptors and less melanin absorption occurred from the remaining light, leading to a decrease in PT-OCT signal. However, it is not known if aggregation of melanosomes could also affect the absorption properties of melanin and change the PT-OCT signal between the light-adapted and dark-adapted groups. In comparison, a similar study by Zhang *et al*[9]. used OCT to observe melanosome translocation in the RPE of frogs and observed an increase in OCT intensity with dark-adaptation. This was due to the aggregation of the highly scattering melanosomes in the apical part of the RPE cells. This demonstrates that PT-OCT measurements provide complimentary information to OCT by using a different contrast

mechanism. Overall, both the changes in PT-OCT signal appearance and intensity indicate that PT-OCT is sensitive to intracellular changes in pigmentation. In the future, PT-OCT could be used to examine other models of retinal disease involving changes in pigmentation[36].

Comparing the OCT/PT-OCT signal to histology could lead to a better understanding of the anatomic features that lead to specific bands in the OCT signal. For example, in animal models with retinomotor movements, researchers could compare histology to the OCT and PT-OCT signal to better determine the origin of the outer retinal bands. In this study, the histology section of the light-adapted zebrafish shows some cone outer segments surrounded by melanin (Fig. 5.4e). In the corresponding OCT/PT-OCT image, the anterior-most band of the three-band PT-OCT pattern overlaps with one of the OCT photoreceptor bands, which could help localize the origin of the OCT bands. In comparison, the melanosomes in the dark-adapted zebrafish are segregated in the basal outer part of the RPE cells and do not overlap with any photoreceptors, which results in an absence of band-like features in the PT-OCT signal.

There are however limitations to this study. More comparative anatomy is needed before findings from the zebrafish can be generalized to humans. Additionally, shadowing and phase accumulation are two artifacts present in the PT-OCT signal[37, 38], which will affect the signal intensity as a function of depth. For this reason, it is difficult to precisely quantify the distribution of melanin as a function of depth, and artifacts can be seen on some images (such as Fig. 5.3f where significant shadowing is seen below the RPE). In terms of experimental parameters, the photothermal laser power will have to be reduced in future studies to comply with ANSI standards (approximately 0.5mW maximum permissible exposure at λ=685nm, compared to 1.8mW used in this study). To translate this technique to human retinal imaging, scanning times will also have to be reduced, which could be accomplished by reducing the number of repeated A-scans acquired for each pixel and increasing the amplitude-modulation frequency of the photothermal laser.

In summary, we have demonstrated PT-OCT in the zebrafish eye for the first time. We have validated that the PT-OCT signal is specific to melanin. We have characterized changes in the PT-OCT signal based on light-driven melanosome translocation within RPE cells. Additionally, we have compared

PT-OCT images to histology sections, which inform how different features of the OCT signal are interpreted. PT-OCT could be applied to the wide array of zebrafish models and other models of retinal disease to facilitate mechanistic studies or identify early diagnostic features of disease. In addition, PT-OCT could be used to monitor response to drugs that aim to correct defective melanin biosynthesis.

5.6 Acknowledgements

The authors would like to thank Suresh Kumar, Samantha Servi, and Christine Duris for their assistance with this study, and Barbara Blodi for helpful discussions. This work was supported in part by the National Center for Advancing Translational Sciences of the National Institutes of Health (NIH) under award numbers UL1TR001436 and TL1TR001437, by the National Eye Institute of the NIH under award numbers R01EY016060, P30EY001931, and F30EY0277706 and by the National Institute of General Medical Sciences of the NIH under award number T32GM080202. Additional support was provided by the Alcon Research Institute and the Foundation Fighting Blindness PPA-0617-0718.

5.7 References

[1] J. Fujimoto and E. Swanson, "The development, commercialization, and impact of optical coherence tomography," *Investigative ophthalmology & visual science,* vol. 57, no. 9, pp. OCT1-OCT13, 2016.

[2] G. Staurenghi, S. Sadda, U. Chakravarthy, and R. F. Spaide, "Proposed lexicon for anatomic landmarks in normal posterior segment spectral-domain optical coherence tomography: the IN• OCT consensus," *Ophthalmology,* vol. 121, no. 8, pp. 1572-1578, 2014.

[3] E. M. Anger *et al.*, "Ultrahigh resolution optical coherence tomography of the monkey fovea. Identification of retinal sublayers by correlation with semithin histology sections," *Experimental eye research,* vol. 78, no. 6, pp. 1117-1125, 2004.

[4] R. F. Spaide and C. A. Curcio, "Anatomical correlates to the bands seen in the outer retina by optical coherence tomography: literature review and model," *Retina,* vol. 31, no. 8, p. 1609, 2011.

[5] R. S. Jonnal, O. P. Kocaoglu, R. J. Zawadzki, S.-H. Lee, J. S. Werner, and D. T. Miller, "The cellular origins of the outer retinal bands in optical coherence tomography images," *Investigative ophthalmology & visual science,* vol. 55, no. 12, pp. 7904-7918, 2014.

[6] I. Bhutto and G. Lutty, "Understanding age-related macular degeneration (AMD): relationships between the photoreceptor/retinal pigment epithelium/Bruch's membrane/choriocapillaris complex," *Molecular aspects of medicine,* vol. 33, no. 4, pp. 295-317, 2012.

[7] U. Kellner, S. Kellner, B. H. Weber, B. Fiebig, S. Weinitz, and K. Ruether, "Lipofuscin-and melanin-related fundus autofluorescence visualize different retinal pigment epithelial alterations in patients with retinitis pigmentosa," *Eye,* vol. 23, no. 6, p. 1349, 2009.

[8] M. L. Klein *et al.*, "Retinal precursors and the development of geographic atrophy in age-related macular degeneration," *Ophthalmology,* vol. 115, no. 6, pp. 1026-1031, 2008.
[9] Q.-X. Zhang, R.-W. Lu, J. D. Messinger, C. A. Curcio, V. Guarcello, and X.-C. Yao, "In vivo optical coherence tomography of light-driven melanosome translocation in retinal pigment epithelium," *Scientific reports,* vol. 3, 2013.
[10] M. A. Wilk, A. L. Huckenpahler, R. F. Collery, B. A. Link, and J. Carroll, "The Effect of Retinal Melanin on Optical Coherence Tomography Images," *Translational Vision Science & Technology,* vol. 6, no. 2, pp. 8-8, 2017.
[11] C. N. Keilhauer and F. o. C. Delori, "Near-Infrared Autofluorescence Imaging of the Fundus: Visualization of Ocular Melanin," vol. 47, no. 8, pp. 3556-3564, 2006.
[12] T. Duncker, M. R. Tabacaru, W. Lee, S. H. Tsang, J. R. Sparrow, and V. C. Greenstein, "Comparison of near-infrared and short-wavelength autofluorescence in retinitis pigmentosa," *Investigative ophthalmology & visual science,* vol. 54, no. 1, pp. 585-591, 2013.
[13] S. Yoshitake *et al.*, "Qualitative and quantitative characteristics of near-infrared autofluorescence in diabetic macular edema," *Ophthalmology,* vol. 121, no. 5, pp. 1036-1044, 2014.
[14] X. Zhang, C. A. Puliafito, S. Jiao, and H. F. Zhang, "Simultaneous in vivo imaging of melanin and lipofuscin in the retina with photoacoustic ophthalmoscopy and autofluorescence imaging," *Journal of biomedical optics,* vol. 16, no. 8, p. 080504, 2011.
[15] X. Shu, H. Li, B. Dong, C. Sun, and H. F. Zhang, "Quantifying melanin concentration in retinal pigment epithelium using broadband photoacoustic microscopy," *Biomedical optics express,* vol. 8, no. 6, pp. 2851-2865, 2017.
[16] J. F. De Boer, T. E. Milner, M. J. van Gemert, and J. S. Nelson, "Two-dimensional birefringence imaging in biological tissue by polarization-sensitive optical coherence tomography," *Optics letters,* vol. 22, no. 12, pp. 934-936, 1997.
[17] D. C. Adler, S. W. Huang, R. Huber, and J. G. Fujimoto, "Photothermal detection of gold nanoparticles using phase-sensitive optical coherence tomography," *Optics Express,* vol. 16, no. 7 SRC - GoogleScholar, pp. 4376-4393, 2008.
[18] M. C. Skala, M. J. Crow, A. Wax, and J. A. Izatt, "Photothermal optical coherence tomography of epidermal growth factor receptor in live cells using immunotargeted gold nanospheres," *Nano letters,* vol. 8, no. 10, pp. 3461-3467, 2008.
[19] M. Pircher, C. K. Hitzenberger, and U. Schmidt-Erfurth, "Polarization sensitive optical coherence tomography in the human eye," *Progress in retinal and eye research,* vol. 30, no. 6, pp. 431-451, 2011.
[20] B. Baumann *et al.*, "Melanin pigmentation in rat eyes: in vivo imaging by polarization-sensitive optical coherence tomography and comparison to histology," *Investigative ophthalmology & visual science,* vol. 56, no. 12, pp. 7462-7472, 2015.
[21] E. Götzinger *et al.*, "Retinal pigment epithelium segmentation by polarization sensitive optical coherence tomography," *Optics express,* vol. 16, no. 21, pp. 16410-16422, 2008.
[22] B. Baumann, "Polarization sensitive optical coherence tomography of melanin provides intrinsic contrast based on depolarization," *Biomedical optics express,* vol. 3, no. 7 SRC - GoogleScholar, pp. 1670-1683, 2012.
[23] A. L. Huckenpahler *et al.*, "Imaging the adult zebrafish cone mosaic using optical coherence tomography," *Visual Neuroscience,* vol. 33, 2016.
[24] T. J. Bailey, D. H. Davis, J. E. Vance, and D. R. Hyde, "Spectral-Domain Optical Coherence Tomography as a Noninvasive Method to Assess Damaged and Regenerating Adult Zebrafish RetinasSD-OCT of Light-Damaged Zebrafish Retinas," *Investigative ophthalmology & visual science,* vol. 53, no. 6, pp. 3126-3138, 2012.
[25] D. G. Howe *et al.*, "The Zebrafish model organism database: new support for human disease models, mutation details, gene expression phenotypes and searching," *Nucleic acids research,* vol. 45, no. D1, pp. D758-D768, 2016.

[26] C. Hodel, S. C. Neuhauss, and O. Biehlmaier, "Time course and development of light adaptation processes in the outer zebrafish retina," *The Anatomical Record,* vol. 288, no. 6, pp. 653-662, 2006.
[27] J. Tucker-Schwartz, T. Meyer, C. Patil, C. Duvall, and M. Skala, "In vivo photothermal optical coherence tomography of gold nanorod contrast agents," *Biomedical optics express,* vol. 3, no. 11, pp. 2881-2895, 2012.
[28] M. Wojtkowski, V. J. Srinivasan, T. H. Ko, J. G. Fujimoto, A. Kowalczyk, and J. S. Duker, "Ultrahigh-resolution, high-speed, Fourier domain optical coherence tomography and methods for dispersion compensation," *Optics express,* vol. 12, no. 11, pp. 2404-2422, 2004.
[29] M. Guizar-Sicairos, S. T. Thurman, and J. R. Fienup, "Efficient subpixel image registration algorithms," *Optics letters,* vol. 33, no. 2, pp. 156-158, 2008.
[30] Y. Jung, R. Reif, Y. Zeng, and R. K. Wang, "Three-dimensional high-resolution imaging of gold nanorods uptake in sentinel lymph nodes," *Nano letters,* vol. 11, no. 7, pp. 2938-2943, 2011.
[31] J. M. Tucker-Schwartz, M. Lapierre-Landry, C. A. Patil, and M. C. Skala, "Photothermal optical lock-in optical coherence tomography for in vivo imaging," *Biomedical optics express,* vol. 6, no. 6, pp. 2268-2282, 2015.
[32] M. Lapierre-Landry, A. Y. Gordon, J. S. Penn, and M. C. Skala, "In vivo photothermal optical coherence tomography of endogenous and exogenous contrast agents in the eye," *Scientific reports,* vol. 7, p. 9228, 2017.
[33] C. G. Summers, "Albinism: classification, clinical characteristics, and recent findings," *Optometry and Vision Science,* vol. 86, no. 6, pp. 659-662, 2009.
[34] A. T. Fahim, S. P. Daiger, and R. G. Weleber, "Nonsyndromic retinitis pigmentosa overview," 2017.
[35] Y. Li, G. Li, H. Wang, J. Du, and J. Yan, "Analysis of a gene regulatory cascade mediating circadian rhythm in zebrafish," *PLoS computational biology,* vol. 9, no. 2, p. e1002940, 2013.
[36] B. A. Link and R. F. Collery, "Zebrafish models of retinal disease," *Annual review of vision science,* vol. 1, pp. 125-153, 2015.
[37] M. Lapierre-Landry, J. M. Tucker-Schwartz, and M. C. Skala, "Depth-resolved analytical model and correction algorithm for photothermal optical coherence tomography," *Biomedical optics express,* vol. 7, no. 7, pp. 2607-2622, 2016.
[38] G. Guan, R. Reif, Z. Huang, and R. K. Wang, "Depth profiling of photothermal compound concentrations using phase sensitive optical coherence tomography," *Journal of biomedical optics,* vol. 16, no. 12, pp. 126003-1260039, 2011.

CHAPTER 6

Photothermal optical coherence tomography of indocyanine green in *ex vivo* eyes

M. Lapierre-Landry, T. B. Connor, J. Carroll, Y. K. Tao, and M. C. Skala, "Photothermal optical coherence tomography of indocyanine green in ex vivo eyes," *Optics letters,* vol. 43, no. 11, pp. 2470-2473, 2018.

6.1 Abstract

Indocyanine green (ICG) is routinely used during surgery to stain the inner limiting membrane (ILM) and provide contrast on white light surgical microscopy. While translation of optical coherence tomography (OCT) for intraoperative imaging during ophthalmic surgery has enhanced visualization, the ILM remains difficult to distinguish from underlying retinal structures and ICG does not provide additional OCT contrast. We present photothermal optical coherence tomography (PT-OCT) for high-specificity detection of ICG on retinal OCT images. We demonstrate our technique by performing an ILM peel in *ex vivo* eyes using low ICG concentrations and laser powers. These results establish the feasibility of PT-OCT for intraoperative guidance during retinal surgery.

6.2 Introduction

The inner limiting membrane (ILM) is a thin, transparent membrane that forms a boundary between the vitreous and retinal nerve fiber layer. Surgical peeling of the ILM benefits post-operative outcomes in patients with macular hole, epiretinal membrane, and some forms of chronic diabetic macular edema[1]. Exogenous dyes, such as indocyanine green (ICG), are routinely used to preferentially stain the transparent ILM and enhance contrast under white light microscopy[2-4]. Optical coherence tomography (OCT) for intraoperative imaging during ophthalmic surgery has enabled real-time, depth-resolved visualization of retinal structures and instrument-tissue interactions without the need for exogenous contrast[5-8]. However, the ILM is difficult to distinguish from the underlying retina on OCT images, which limits the utility of OCT to guide ILM peeling procedures.

While ICG is used because it preferentially stains the ILM[2], OCT does not have a contrast mechanism to detect ICG and identify the ILM. Any increase in OCT signal intensity due to ICG is nonspecific and cannot be reliably detected. Furthermore, studies have observed retinal phototoxicity at clinical concentrations of ICG (0.6-5mg/cc)[9, 10], which further highlights the need for high sensitivity detection of ICG during ophthalmic surgery.

Molecular OCT[11] is a functional extension of OCT that adds molecular contrast, and includes modalities such as spectroscopic[12], pump-probe[13], magnetomotive[14] and photothermal OCT[15, 16]. These techniques could provide specific detection of the ICG-stained ILM within the OCT field-of-view. However, to our knowledge no molecular OCT technique has been used to detect ICG in the eye.

We propose photothermal OCT (PT-OCT) to specifically detect the ICG-stained ILM. As previously demonstrated[17], the PT-OCT signal is quantitative and proportional to variables such as absorber concentration and photothermal laser power, as seen in the following equation:

$$PTOCT \propto \Delta T = \frac{P_0 \mu_a}{4\alpha\pi\rho c} \ln\left(1 + \frac{t_L \alpha}{w(z)^2 / 8}\right) \qquad (6.1)$$

where ΔT is the change in temperature, P_0 is the photothermal laser power at the sample, μ_a is the absorption coefficient, α is the thermal diffusivity, ρ is the density of the sample, c is the specific heat, t_L is the laser exposure time, and $w(z)$ is the $1/e^2$ beam radius as a function of depth, z.

In the past, PT-OCT has mostly been used to detect gold nanoparticles in phantoms[15], cells[18] and bulk tissue[19]. PT-OCT has also been used to detect high concentrations of ICG (>0.5mg/cc) *ex vivo* in phantoms[20] and *in vivo* in the mouse ear[21] using high photothermal laser powers (70-80mW). Additionally, PT-OCT has been demonstrated *in vivo* in the mouse eye to detect melanin and gold nanorods[22]. In this letter, we demonstrate PT-OCT of ICG in phantoms at low ICG concentrations (0.08-0.6mg/cc) and using low photothermal laser powers (0.4-3mW, ANSI maximum exposure ~0.5mW[23]). We also demonstrate PT-OCT of ICG in cadaveric pig eyes to identify the ILM and perform an ILM peel.

6.3 Methods

A commercial spectral domain OCT (Bioptigen, λ=860nm, 93nm bandwidth, 36kHz acquisition rate) was modified to perform PT-OCT. A diode laser (Coherent, λ=685nm, f_0=500Hz amplitude-modulation, square wave, 50% duty cycle) was added to the light path via a 50:50 coupler to provide photothermal excitation. A circulator (AC Photonics) was also added to re-direct the OCT signal from the sample to the spectrometer. Excitation at 685nm corresponds to the absorption peak of ICG at high concentrations in water[24]. The OCT superluminescent diode originally had a power of 0.7mW at the sample, but the addition of the circulator reduced the power to 0.470mW at the sample. The photothermal laser had a power between 0-3.12mW at the sample depending on the experiment. B-scans were acquired across 2.5mm with 400 pixels, each consisting of 700 repeated A-scans (M-scan). Each B-scan took approximately 7s to acquire. PT-OCT data processing was performed after data acquisition as previously described using a custom MATLAB code[17]. In summary, the data was first resampled from wavelength to wavenumber, dispersion corrected[25], and background subtracted. A Chirp-Z transform was used to convert the wavenumber dimension into spatial domain and obtain the OCT intensity and phase signal. For each pixel in depth over the 700 M-scans, the first temporal derivative of the phase data was calculated. A Fourier transform was used to convert the phase oscillations from the time domain to the frequency domain and allowed identification of the peak corresponding to the photothermal modulation frequency (f_0=500 Hz). The amplitude of the peak was taken to be the PT-OCT signal intensity as seen in Eq.6.2[17]:

$$PTOCT(z) = \frac{|p(z, f_0)|\lambda}{4\pi^2 f_0 n \Delta t} \qquad (6.2)$$

where p is the phase frequency spectrum, f_0 is the laser modulation frequency, λ is the OCT central wavelength, n is the index of refraction of the tissue, and Δt is the acquisition time for one A-scan. The resulting PT-OCT signal is in units of nanometers and represents the induced optical path length change. In addition to the peak amplitude, the mean amplitude away from the peak (250-400Hz, 600-750Hz) was

defined as the noise floor. Final images were constructed by subtracting the noise floor from the signal intensity. The PT-CLEAN algorithm was then applied to reduce the effect of shadowing[26].

A constant 0.5nm noise at a frequency between 503-505Hz was present in all negative controls, phantoms, and tissue. This created a beat frequency in all positive controls, both in phantoms and tissue. Thus, a 0.5nm constant signal at 503-505Hz was subtracted from all images for all samples to improve visualization.

Phantoms were made from 1μL of ICG diluted in saline at concentrations 0.08, 0.16, 0.20, 0.31, 0.39, and 0.62mg/cc placed on colored label tape and imaged immediately. Samples were imaged with the photothermal laser power set at 0 (laser off), 0.48, 0.59, 0.80, 1.0, 1.2, 1.7, 2.3 and 3.4mW measured at the sample.

Freshly-excised cadaveric pig eyes were obtained for imaging (~6 hours after death). To help separate the anterior hyaloid membrane from the lens, air (0.5cc) was injected into the vitreous cavity through the sclera via a 30G needle 2 mm posterior to the temporal limbus. The air bubble was left for 10-30 minutes. A 15° blade was used to make an incision at the corneoscleral limbus, and then enlarged by curved Stevens scissors to completely remove the cornea. A lens loop and muscle hook were used to remove the crystalline lens. A syringe with an 18G flat-end fill needle was used to engage vitreous with aspiration, lift in anteriorly and then severe its attachments with Wescott scissors. This aspiration technique was able to engage and separate the posterior hyaloid membrane from the retinal surface. The retinal surface was then dried with a Weck-Cel sponge applied to the optic nerve head.

ICG was diluted at concentrations of 0.25mg/cc and 0.5mg/cc in saline and kept wrapped in foil until application (<15 minutes) to reduce photobleaching. The ICG was applied to the ILM for one minute. The retina was then rinsed with saline and all liquid above the ILM was removed using Weck-Cel sponges applied to the optic nerve head. The retina was then imaged with PT-OCT.

To validate that the ICG was specifically staining the ILM, an ILM-peel was performed on one *ex vivo* pig eye. The eye was prepared as previously described and stained with 0.25mg/cc ICG for one minute before being rinsed with saline and dried with a Weck-Cel sponge. A section of the ILM was then peeled using 23G Eckardt-style ILM forceps under a white light surgical microscope.

6.4 Results

The average PT-OCT signal obtained in phantoms as a function of photothermal laser power can be seen in Fig.6.1a for different ICG concentrations and a saline control (0mg/cc). In accordance to theory (Eq.6.1), the PT-OCT signal increases linearly with the photothermal laser power (R^2>0.98) for samples with low ICG concentration (<0.3mg/cc). Samples with higher concentrations (0.31-0.62mg/cc) cannot be considered optically transparent ($P(z) \neq P_0$) and thus do not follow Eq.6.1. The non-linear increase in PT-OCT signal is likely caused by shadowing (due to the high absorption coefficient)[27] and re-absorption of

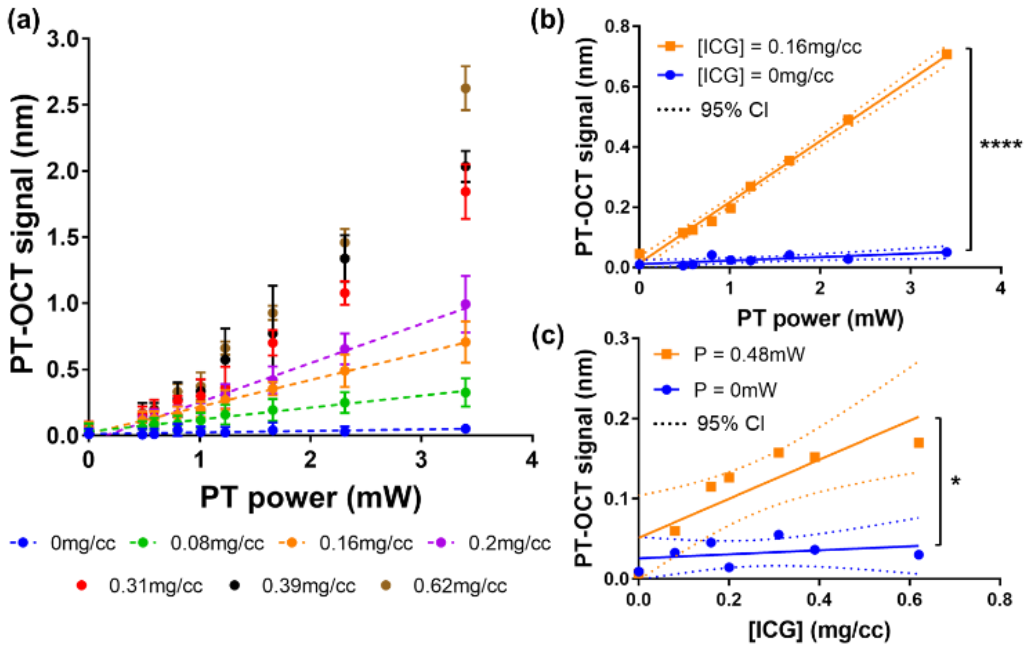

Fig. 6.1. Average PT-OCT signal as a function of photothermal laser power (A) for all ICG phantom concentrations. Dashed lines: linear fit for low concentration samples. Error bar: standard deviation over one B-scan. (B) PT-OCT signal for 0.16mg/cc of ICG (orange) in comparison to saline (blue) as a function of laser power. (C) PT-OCT signal as a function of ICG concentration using 0.48mW (orange) or 0mW (blue) of laser power. Linear fit (solid lines), with 95% confidence interval (dotted lines). *p<0.05, ****p<0.001 difference between slopes.

emitted photons[28]. The absorption coefficient of ICG is not always linearly proportional to ICG concentration[24], but the PT-OCT signal does generally increase with ICG concentration.

To determine the lowest detectable ICG concentration, the slope of each linear fit for the ICG samples in Fig.6.1a was compared to the slope of the saline sample. As seen in Fig. 6.1b, the slope of the 0.16mg/cc ICG sample (slope = 0.203 ± 0.006) was significantly different from the slope of the saline sample (slope = 0.012 ± 0.004) ($p<0.001$, ANCOVA[29]). Similarly, to determine the lowest usable photothermal laser power, the average PT-OCT signal as a function of ICG concentration was plotted for each laser power, and a linear fit was performed. As seen in Fig. 6.1c, the slope of the distribution acquired at 0.48mW (slope = 0.24 ± 0.06) is significantly different from the slope of the distribution acquired with the laser off (slope = 0.02 ± 0.03) ($p<0.05$, ANCOVA[29]). The 0.08mg/cc sample was not different from control when imaged at 0.48mW.

For our control, the PT-OCT signal of the saline sample (Fig. 6.1b, blue) increases by a very small amount as a function of photothermal laser power (slope = 0.012 ± 0.004), which could be due to light absorption by the saline or tape. The PT-OCT signal does not increase as a function of ICG concentration

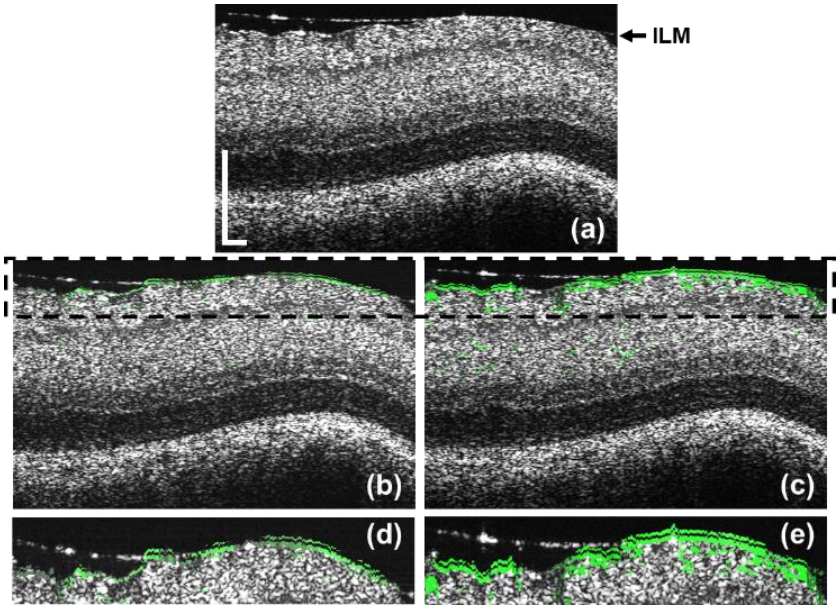

Fig. 6.2. PT-OCT of an *ex vivo* porcine retina after the ILM was stained with 0.5mg/cc of ICG. (A) OCT (gray) and (B) corresponding PT-OCT B-scans (overlaid in green) using 0.89mW or (C) 3.12mW of photothermal laser power. Magnified view of boxed area in (D) and (E). Scale bar: 200 µm.

(Fig. 6.1c, blue) when the laser is turned off (slope = 0.02 ± 0.03). No photobleaching of ICG was detected over one A-scan, and B-scans were taken at different sample locations to minimize photobleaching. Based on these results, we conclude that PT-OCT is sensitive to ICG concentrations as low as 0.16mg/cc while using photothermal laser powers as low as 0.48mW in phantoms.

PT-OCT B-scans were acquired in *ex vivo* pig eyes to better demonstrate our technique. OCT (Fig. 6.2a) and corresponding PT-OCT B-scans (Figs. 6.2b-c) of the retina are shown after application of 0.5mg/cc of ICG. The photothermal laser was set to 0.89mW for Fig. 6.2b and PT-OCT signal can be seen at a location consistent with the ILM (magnified in Fig. 6.2d). The same location on the retina was also imaged with PT-OCT at a higher laser power (3.12mW, Fig. 6.2c, magnified in 6.2e) to confirm the presence of PT-OCT signal all along the ILM. For comparison, no PT-OCT signal was detected when the PT-OCT B-scan of a retina at 3.12mW without ICG application was acquired (data not shown). This confirms that PT-OCT can detect the ICG-stained ILM at low laser powers.

An ILM peel was performed in one eye after 0.25mg/cc ICG application to demonstrate that the ICG only dyes the ILM. In the clinic, this procedure would normally be performed under a white light

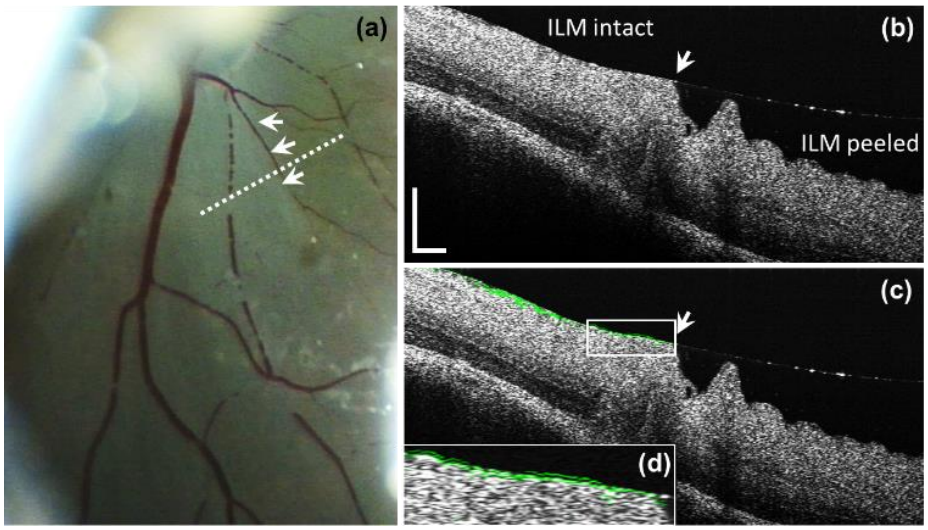

Fig. 6.3. PT-OCT of an ILM-peel in *ex vivo* pig eye. (A) White light image from the surgical microscope showing boundary between the intact ILM dyed with 0.25mg/cc ICG and the peeled ILM (arrows) with the B-scan location (dashed line). (B) OCT (gray) and (C) corresponding PT-OCT B-scan (green) showing a cross-section of the retina with intact ILM and after it was peeled (arrows at boundary). (D) Magnified view of boxed area in (C). Scale bar: 200µm.

surgical microscope, where ICG is used to increase the contrast between the ILM and the retina. An image acquired using the microscope camera after ICG application and ILM peel can be seen in Fig. 6.3a. The boundary between the area where the ILM was peeled and the area where the ILM is intact is indicated by the white arrows. The ICG concentration used is low compared to the concentrations traditionally used in surgery for this procedure (0.5-5mg/cc), which explains the very low contrast between ILM and non-ILM regions in this image when visualized under white light. PT-OCT B-scans perpendicular to the boundary were acquired, and an example OCT (white dashed line) and corresponding PT-OCT B-scans can be seen in Fig. 6.3b-c. The PT-OCT B-scan was acquired with a photothermal laser power of 3.12mW. A clear PT-OCT signal can be seen where the ILM was left intact (Fig. 6.3d), while no PT-OCT signal above noise floor can be seen in the region where the ILM was peeled. Presence and absence of ILM was determined based on the surgeon's feedback and the morphology of the retina as seen in the OCT scan (Fig. 6.3b).

6.5 Discussion

OCT is being incorporated into the surgical suite to provide depth-resolved visualization of instrument-tissue interaction during retinal surgery[8]. Peeling the ILM is one such procedure where OCT provides crucial information to the surgeon. To increase the contrast between the ILM and other layers of the retina, surgeons routinely use dyes such as ICG[1], that specifically binds to the ILM [2]. However, OCT lacks a contrast mechanism to detect ICG, and the high concentrations of ICG that are used in surgery may be associated with phototoxicity. In this study, we demonstrated that PT-OCT can detect low concentrations of ICG used to stain the ILM in *ex vivo* pig eyes. This is the first time a molecular OCT technique has been used to specifically detect ICG in the eye.

In the first part of this study, we tested the sensitivity of PT-OCT to low concentrations of ICG at low photothermal laser powers. In the past, PT-OCT was performed at high photothermal laser powers (70-80mW)[20, 21] to increase the signal intensity when using ICG as a contrast agent. The ANSI maximum permissible exposure for a laser at 685nm for a 7s scan is approximately 0.5mW[23]. In this paper, we

demonstrate in phantoms that PT-OCT is sensitive to ICG at a clinically relevant laser power (0.48mW) and low concentrations of the dye (0.16mg/cc), which should reduce potential phototoxicity.

In the second part of this study, we detected the presence of ICG on the ILM of cadaveric pig eyes using PT-OCT. For this experiment, the cornea, lens and vitreous were removed to expose the ILM. In human patients, the vitreous can be removed and replaced with saline while keeping the cornea and lens in place and without damaging the ILM. The ICG can then be injected into the eye to stain the ILM. However, in pigs the vitreous is strongly attached to the ILM, preventing both a normal vitrectomy or an ICG injection in a whole cadaveric eye[30]. For that reason, we gently removed the vitreous with Weck-Cel sponges to avoid any damage to the ILM or the retina before ICG application and imaging. In the future, this experiment could be repeated in a *in vivo* pig model, where a traditional vitrectomy and ICG injection could be performed before PT-OCT imaging. This would more closely resemble the clinical surgical procedure.

Finally, we performed an ILM peel in a cadaveric pig eye to confirm our hypothesis that ICG specifically stained the ILM, and that peeling the ILM would remove all PT-OCT signal due to the ICG. In the images obtained during this experiment, a clear PT-OCT signal can be seen where the ILM is intact, and no PT-OCT signal above the noise floor is present where the ILM has been peeled, confirming our hypothesis. This also clearly demonstrates how ICG combined with PT-OCT imaging would improve contrast of the ILM for intraoperative OCT guidance.

In the future, strategies to reduce PT-OCT imaging times will be evaluated to increase the B-scan rate and acquire volume scans. Reducing the number of repeated A-scans per pixel would increase imaging speed, especially if combined with a faster photothermal modulation frequency. For example, 200 repeated A-scans instead of 700 would reduce the acquisition time to 2s, which is the same acquisition time as a Doppler scan on our Bioptigen system.

In conclusion, we detected clinically low concentrations of ICG (<0.25mg/cc) using PT-OCT at low photothermal laser powers (<0.5mW). Additionally, we performed an ILM peel in *ex vivo* pig eyes to

demonstrate that the PT-OCT signal is specific to the ICG-stained ILM. These preliminary results show the potential of PT-OCT for clinical use in the eye.

6.6 Acknowledgements

We thank Daniel A. Gil for the helpful discussions. We also thank Christine Skumatz and Alison L. Huckenpahler for their help while conducting these experiments. This work was sponsored in part by the following: National Institute of Health (NIH) (R01 CA205101, R01 CA1857447, R01 CA211082, P30EY001931); Stand Up to Cancer (SU2C-AACR-IG-08-16, Sharp Award); Department of Defense (DOD) (W81XWH-13-1-0194); National Science Foundation (NSF) (CBET-1642287); The Mary Kay Foundation (067-16); Alcon Research Institute.

6.7 References

[1] F. Semeraro, F. Morescalchi, S. Duse, E. Gambicorti, A. Russo, and C. Costagliola, "Current trends about inner limiting membrane peeling in surgery for epiretinal membranes," *Journal of ophthalmology*, vol. 2015, 2015.

[2] A. Gandorfer, E. M. Messmer, M. W. Ulbig, and A. Kampik, "Indocyanine green selectively stains the internal limiting membrane," *American journal of ophthalmology*, vol. 131, no. 3, pp. 387-388, 2001.

[3] P. Stalmans, R. Parys-Vanginderdeuren, R. De Vos, and E. Feron, "ICG staining of the inner limiting membrane facilitates its removal during surgery for macular holes and puckers," *Bull Soc Belge Ophtalmol*, vol. 281, no. 21, p. e6, 2001.

[4] A. K. Kwok, T. Y. Lai, D. T. Yew, and W. W. Li, "Internal limiting membrane staining with various concentrations of indocyanine green dye under air in macular surgeries," *American journal of ophthalmology*, vol. 136, no. 2, pp. 223-230, 2003.

[5] Y. K. Tao, J. P. Ehlers, C. A. Toth, and J. A. Izatt, "Intraoperative spectral domain optical coherence tomography for vitreoretinal surgery," *Optics letters*, vol. 35, no. 20, pp. 3315-3317, 2010.

[6] S. Binder, C. I. Falkner-Radler, C. Hauger, H. Matz, and C. Glittenberg, "Feasibility of intrasurgical spectral-domain optical coherence tomography," *Retina*, vol. 31, no. 7, pp. 1332-1336, 2011.

[7] J. P. Ehlers *et al.*, "Determination of feasibility and utility of microscope-integrated optical coherence tomography during ophthalmic surgery: the DISCOVER Study RESCAN Results," *JAMA ophthalmology*, vol. 133, no. 10, pp. 1124-1132, 2015.

[8] O. M. Carrasco-Zevallos *et al.*, "Review of intraoperative optical coherence tomography: technology and applications," *Biomedical Optics Express*, vol. 8, no. 3, pp. 1607-1637, 2017.

[9] M. Murata, S. Shimizu, S. Horiuchi, and S. Sato, "The effect of indocyanine green on cultured retinal glial cells," *Retina*, vol. 25, no. 1, pp. 75-80, 2005.

[10] P. Saikia *et al.*, "Safety testing of indocyanine green in an ex vivo porcine retina model," *Investigative ophthalmology & visual science*, vol. 47, no. 11, pp. 4998-5003, 2006.

[11] A. L. Oldenburg, B. E. Applegate, J. M. Tucker-Schwartz, M. C. Skala, J. Kim, and S. A. Boppart, "Molecular optical coherence tomography contrast enhancement and imaging," *Optical Coherence Tomography: Technology and Applications,* pp. 1429-1454, 2015.
[12] U. Morgner *et al.*, "Spectroscopic optical coherence tomography," *Optics letters,* vol. 25, no. 2, pp. 111-113, 2000.
[13] K. D. Rao, M. A. Choma, S. Yazdanfar, A. M. Rollins, and J. A. Izatt, "Molecular contrast in optical coherence tomography by use of a pump–probe technique," *Optics letters,* vol. 28, no. 5, pp. 340-342, 2003.
[14] A. L. Oldenburg, F. J.-J. Toublan, K. S. Suslick, A. Wei, and S. A. Boppart, "Magnetomotive contrast for in vivo optical coherence tomography," *Optics Express,* vol. 13, no. 17, pp. 6597-6614, 2005.
[15] D. C. Adler, S. W. Huang, R. Huber, and J. G. Fujimoto, "Photothermal detection of gold nanoparticles using phase-sensitive optical coherence tomography," *Optics Express,* vol. 16, no. 7 SRC - GoogleScholar, pp. 4376-4393, 2008.
[16] M. C. Skala, M. J. Crow, A. Wax, and J. A. Izatt, "Photothermal optical coherence tomography of epidermal growth factor receptor in live cells using immunotargeted gold nanospheres," *Nano letters,* vol. 8, no. 10, pp. 3461-3467, 2008.
[17] J. Tucker-Schwartz, T. Meyer, C. Patil, C. Duvall, and M. Skala, "In vivo photothermal optical coherence tomography of gold nanorod contrast agents," *Biomedical optics express,* vol. 3, no. 11, pp. 2881-2895, 2012.
[18] C. Pache *et al.*, "Fast three-dimensional imaging of gold nanoparticles in living cells with photothermal optical lock-in Optical Coherence Microscopy," *Optics express,* vol. 20, no. 19, pp. 21385-21399, 2012.
[19] Y. Jung, R. Reif, Y. Zeng, and R. K. Wang, "Three-dimensional high-resolution imaging of gold nanorods uptake in sentinel lymph nodes," *Nano letters,* vol. 11, no. 7, pp. 2938-2943, 2011.
[20] H. M. Subhash, H. Xie, J. W. Smith, and O. J. McCarty, "Optical detection of indocyanine green encapsulated biocompatible poly (lactic-co-glycolic) acid nanoparticles with photothermal optical coherence tomography," *Optics letters,* vol. 37, no. 5, pp. 981-983, 2012.
[21] J. M. Tucker-Schwartz, M. Lapierre-Landry, C. A. Patil, and M. C. Skala, "Photothermal optical lock-in optical coherence tomography for in vivo imaging," *Biomedical optics express,* vol. 6, no. 6, pp. 2268-2282, 2015.
[22] M. Lapierre-Landry, A. Y. Gordon, J. S. Penn, and M. C. Skala, "In vivo photothermal optical coherence tomography of endogenous and exogenous contrast agents in the eye," *Scientific reports,* vol. 7, p. 9228, 2017.
[23] (2014). *American National Standards Institute for Safe Use of Lasers (ANSI/UL).*
[24] M. Landsman, G. Kwant, G. Mook, and W. Zijlstra, "Light-absorbing properties, stability, and spectral stabilization of indocyanine green," *Journal of applied physiology,* vol. 40, no. 4, pp. 575-583, 1976.
[25] M. Wojtkowski, V. J. Srinivasan, T. H. Ko, J. G. Fujimoto, A. Kowalczyk, and J. S. Duker, "Ultrahigh-resolution, high-speed, Fourier domain optical coherence tomography and methods for dispersion compensation," *Optics express,* vol. 12, no. 11, pp. 2404-2422, 2004.
[26] M. Lapierre-Landry, J. M. Tucker-Schwartz, and M. C. Skala, "Depth-resolved analytical model and correction algorithm for photothermal optical coherence tomography," *Biomedical optics express,* vol. 7, no. 7, pp. 2607-2622, 2016.
[27] C. Hu, F. E. Muller-Karger, and R. G. Zepp, "Absorbance, absorption coefficient, and apparent quantum yield: A comment on common ambiguity in the use of these optical concepts," *Limnology and Oceanography,* vol. 47, no. 4, pp. 1261-1267, 2002.
[28] B. Yuan, N. Chen, and Q. Zhu, "Emission and absorption properties of indocyanine green in Intralipid solution," *Journal of biomedical optics,* vol. 9, no. 3, pp. 497-504, 2004.
[29] J. H. Zar, "Comparing simple linear regression equations," *Biostatistical analysis,* vol. 2, pp. 292-305, 1984.

[30] S. Pastor-Idoate *et al.*, "Ultrastructural and histopathologic findings after pars plana vitrectomy with a new hypersonic vitrector system. Qualitative preliminary assessment," *PloS one,* vol. 12, no. 4, p. e0173883, 2017.

CHAPTER 7

Conclusions and Future Directions

7.1 Summary and conclusions

The primary goal of this dissertation is to demonstrate the potential of PT-OCT as a novel eye imaging technology, both for pre-clinical and clinical applications. Imaging plays an important role in understanding, diagnosing, and treating eye diseases. OCT in particular provides three-dimensional, high resolution images of the anterior and posterior segments of the eye and has become a standard imaging technique in clinical and research settings. Functional OCT techniques such as OCT angiography have been developed to extract additional information about the tissue from the OCT signal. Functional OCT methods have many advantages over other ophthalmic imaging techniques when used in combination with OCT: they do not require the patient or animal to be moved to a different instrument, they produce images that are perfectly co-registered to the OCT intensity images, they have similar resolution and imaging depth as OCT, and the learning process toward image acquisition is easier for clinicians and researchers already familiar with OCT.

In this dissertation, we demonstrate PT-OCT in the eye for the first time. PT-OCT is a functional OCT technique that detects absorbers in the OCT field-of-view. The OCT signal intensity is based on the presence of scatterers in the sample, and thus the PT-OCT signal provides complimentary information about absorbers in the sample. To this day, there are no other clinical eye imaging technique that specifically detect absorbers. In particular, absorbers such as melanin and gold nanoparticles are difficult to quantify by any means *in vivo* and are difficult to distinguish from other sources of scattering on OCT images. Other contrast agents such as indocyanine green are used in the clinic but are not visible on OCT intensity images. In this dissertation, images of melanin, gold nanorods, and indocyanine green were acquired in different animal models to demonstrate the potential of PT-OCT as an eye imaging technique.

Chapter 2 provides relevant background information to the work described in this dissertation. First, the role of pre-clinical and clinical eye imaging is discussed. AMD is used as an example since pigmentation changes are observed at different stages of the disease and gold nanoparticles have been investigated to treat some of its symptoms. Intraoperative imaging is also discussed since indocyanine green is commonly used in macular surgery. Following this first section, a detailed description of the most common eye imaging techniques is given, with special emphasis on their field-of-view, resolution and contrast mechanism. Amongst those, techniques that can detect retinal melanin are mentioned. Finally, different functional OCT techniques are described with a special focus on work performed in the eye, and previous publications on PT-OCT are reviewed.

Chapter 3 addresses Aim 1 by detailing a theoretical model that predicts the PT-OCT signal with depth. A theoretical model for PT-OCT can provide a better understanding of the different parameters affecting the signal, which can guide instrument design and imaging parameters choice. The model is separated in two parts. First the increase in temperature, the tissue expansion, and the changes in refractive index are modeled, leading to a change in optical path length. Second, the change in optical path length is detected as a change in the OCT phase signal, noise is added to the OCT signal, and the PT-OCT signal is calculated from the change in phase. The theoretical signal generated as such can then be directly compared to experimental data. To validate this model, theoretical signals for different samples and imaging parameters were generated and compared to the corresponding experimental signals acquired under the same conditions. In the second part of Chapter 3, an algorithm to correct imaging artifacts is presented using one of the outputs of the theoretical model. Those artifacts (phase accumulation and shadowing) severely degrade the PT-OCT signal in the axial dimension. To this day, only one correction algorithm has been proposed[1] but it assumes mostly homogeneous samples. The PT-CLEAN algorithm presented in this dissertation corrects for both artifacts without assumptions about the sample composition or the distribution of absorbers. In this chapter, the algorithm is demonstrated in phantoms and *in vivo* in a tumor model. Later in Chapter 6 (Aim 3), the PT-CLEAN algorithm is used to correct the signal acquired from

the inner limiting membrane in *ex vivo* pig eyes. An artifact-free image is necessary to properly interpret PT-OCT B-scans, and thus the PT-CLEAN algorithm is essential for applications of PT-OCT in the eye.

Chapter 4 addresses Aim 2 by imaging gold nanorods and melanin *in vivo* in a mouse eye model. A laser-induced choroidal neovascularization model is used to create lesions in the mice eyes and observe how gold nanorods accumulate in the retina following a systemic injection through the tail vein. An increase in PT-OCT signal is observed in the experimental group injected with gold nanorods compared to control. This is an important result since there are no standard method to image gold nanoparticles *in vivo*, and another functional OCT method (enhanced-backscattering OCT) had previously lacked the sensitivity required to detect gold nanorods against the scattering background of a neovascular lesion[2]. In a separate experiment, wild-type animals (pigmented) are compared to albino animals (non-pigmented) to identify the signal from melanin. A strong PT-OCT signal is observed in the RPE of the wild-type animals, but no signal is detected in the albino animals. This experiment is the first demonstration of PT-OCT in the eye, and both exogenous and endogenous contrast agents were detected *in vivo*.

In Chapter 5, a follow-up study is performed in zebrafish to image melanin and further pursue Aim 2. There is an interest in gaining a better understanding of the RPE[3] and of the effect of melanin on the OCT signal[4]. Imaging melanin with PT-OCT does not require any exogenous contrast agents, which simplifies the study and reduces the risks of toxicity to the animal compared to imaging gold nanorods. A tyrosinase-mosaic zebrafish model with pigmented and non-pigmented regions of the retina within each eye is used to provide a strong validation of the specificity of the PT-OCT signal to melanin. Additionally, dark-adapted and light-adapted zebrafish are imaged to observe the effect of melanosomes translocation on the PT-OCT signal. In light-adapted zebrafish, three horizontal bands are observed in the PT-OCT signal, corresponding to the RPE and the junction between the RPE and photoreceptors. In comparison, a single signal band is observed in all dark-adapted zebrafish. Histology confirms that melanosomes have migrated to the apical region of the RPE cells during dark-adaptation. This study confirms that the PT-OCT signal is specific to melanin in the zebrafish eye and that the technique is sensitive to intracellular melanosomes

translocation from within the RPE. This study also demonstrates the potential of PT-OCT as an eye imaging tool at the pre-clinical level to study melanin biosynthesis and migration.

Chapter 6 addresses Aim 3 by imaging the inner limiting membrane (ILM) of *ex vivo* pig eyes after staining the membrane with indocyanine green. Intraoperative OCT is being developed to provide depth-visualization and guide instrument-tissue interactions during macular surgeries. An ILM-peel is one such procedure where intraoperative OCT can inform a surgeon on the position of their tools compared to the retina. The ILM being a thin and transparent membrane, surgeons may sometimes stain it with indocyanine green (ICG) to increase contrast under a white-light surgical microscope. However, OCT does not have the same contrast mechanism and cannot detect ICG. In this study, PT-OCT of ICG is performed in a mock ILM peel surgical procedure using *ex vivo* pig eyes and sub-clinical concentrations of ICG. First, the sensitivity of PT-OCT to low concentrations of ICG at clinically acceptable photothermal laser powers is demonstrated in phantoms. Then an ILM-peel is performed to test the specificity of the PT-OCT signal to ICG and to the ILM. The PT-CLEAN algorithm developed in Chapter 3 (Aim 1) is used to reduce the effect of shadowing on all PT-OCT images. This study is the first time a clinical application of PT-OCT is investigated.

This dissertation highlights PT-OCT as a novel retinal imaging technique. PT-OCT is an attractive instrument for the many researchers and clinicians who already use OCT on a regular basis to obtain high-resolution, volumetric images of the eye. It is also a unique instrument that can detect optical absorbers and perform quantitative imaging. As demonstrated in this dissertation, PT-OCT is sensitive to many types of contrast agents, such as gold nanoparticles, clinically relevant small molecule dyes and pigments naturally present in the eye. Similar to OCT, PT-OCT can also be performed in many animal models to study different diseases. It is a versatile technique with potential applications both in pre-clinical and clinical research.

7.2 Future directions

<u>Increased acquisition and processing speed</u>

Translation of PT-OCT to the clinic is impeded by the long acquisition time for each PT-OCT scan. On an instrument such as the one used in Chapter 5 and 6 (36kHz A-scan acquisition rate) with the same scan pattern used for those experiments (700 M-scans/A-scan, 400A-scans/B-scan), each PT-OCT B-scan takes approximately 7 seconds to acquire. These long acquisition times make volumetric acquisition in animals or patients impractical. Methods to reduce acquisition time should be investigated. Reducing the number of M-scans per A-scan has been tested down to 300 M-scans which could reduce the acquisition time by half. The amplitude-modulation frequency (set at 500Hz in this dissertation but has been tested up to 725Hz), could also be increased to reduce scan times. When imaging melanin in the RPE, the amplitude-modulation frequency could be increased to 1.5kHz since the RPE is a thin membrane that thus rapidly reaches new temperatures due to heat diffusion (due to diffusion, a 10μm thick membrane would reach equilibrium in 0.6ms). Additionally, the photothermal beam diameter could be reduced, which would cause a faster increase in temperature in the tissue for the same laser power. A faster increase in temperature due to increased amplitude-modulation frequency or smaller beam diameter would allow for faster acquisition of multiple heating cycles, which would decrease overall scan-times while maintaining high SNR. Changing the PT-OCT instrumentation could be necessary to improve the acquisition speed even more and allow for volumetric imaging. Full-field PT-OCT has been attempted before[5] but was not performed *in vivo* or in the eye. Line-field OCT could also be attempted[6]. Using a line-field OCT with a B-scan acquisition rate of 1kHz as described in Barrick *et al.*[6], 30 temperature oscillations at 300Hz could be recorded in 0.1s per B-scan, which would enable volumetric imaging. Thermo-elastic OCT, which is similar to PT-OCT in terms of source of contrast and detection methods, also has the potential for faster acquisition speeds if new pulsed lasers are developed[7].

Depending on which approach is the most successful in terms of increasing acquisition speeds, it may be necessary to also accelerate processing speeds. Currently, each B-scan (700 M-scans/A-scan, 400A-scans/B-scan) takes approximately 8 minutes to process from raw data to final image on MATLAB on a

CPU. This is mainly a result of the many Fourier transforms involved in PT-OCT processing. A parallel computing (GPU) approach could be implemented to accelerate this step.

Improved theoretical model

In Chapter 3, a theoretical model of PT-OCT is described using a solution to the bio-heat conduction equation that assumes a small beam diameter as compared to the absorption depth (see Eq. 3.2, 3.3). However, this assumption does not hold true in many thin layers of the eye, such as the ILM and RPE. An updated version of the theoretical model should use better thermal diffusion modeling to take this situation into account and better understand heat diffusion in the different layers of the retina. Chapter 3 also describes a theoretical PT-OCT signal where the change in phase in a given A-scan cannot decrease with depth (see Eq. 3.4 and 3.5, Fig. 3.5). However as seen in Chapter 5, images acquired in zebrafish display PT-OCT "bands" where the signal repeatedly decrease and increase with depth (see Figs. 5.3, 5.4 and 5.5). This behavior is not accounted for by the theoretical model. As a result, the effect of phase accumulation and shadowing on those bands is not understood and the relative signal intensity for each band cannot be calculated. A better theoretical understanding of the PT-OCT signal is needed to take into account such situations. One possible explanation is that there are sudden decreases in phase sensitivity between each band, which locally reduces the PT-OCT signal until the signal increases again in the next band. However, this hypothesis needs further testing.

Pre-clinical studies of melanin migration and biosynthesis

As demonstrated in Chapter 5, the PT-OCT signal in the zebrafish eye is specific to melanin and sensitive to melanosome translocation within the RPE cells. In further studies, the origin of the three bands seen in light-adapted zebrafish could be identified with careful comparison to histology. As an example, it is unclear if the OCT photoreceptor bands correspond to the inner segment/outer segment junction (see Fig. 5.5) or the inner segment ellipsoid zone. Such a differentiation is also unclear in humans[8, 9]. Zebrafish of different ages could be used to monitor the development of the RPE and to determine how different

conditions affect light-induced pigment migration. Additionally, PT-OCT could be used to study zebrafish knockouts where melanosome translocation is impeded. PT-OCT could also be performed in other animal models such as the 13-lined ground squirrel. In a ground squirrel model of retinal detachment, unidentified scattering debris have been observed within the retina and it is hypothesized that they could be parts of RPE cells or melanosomes. PT-OCT could confirm if those debris contain melanin. Imaging pigment biosynthesis is also of interest in animal models of albinism. PT-OCT would provide quantitative, *in vivo* images of melanin without the need for exogenous contrast agents to better characterize such animal models.

Clinical translation of PT-OCT

Detecting the ILM stained with indocyanine green as described in Chapter 6 is a possible clinical application of PT-OCT. However, this study was performed *ex vivo* in pig eyes. Replicating these results *in vivo* in the pig or another animal model would be a first step toward demonstrating the feasibility of this procedure. Performing such a study *in vivo* would also allow for a more realistic procedure for the vitrectomy (whole eye) and indocyanine green staining. Such a procedure was not possible *ex vivo* where the front part of the eye and vitreous had to be removed without damaging the ILM.

Additionally, PT-OCT has never been performed in the human eye, which is an important step toward clinical translation either as a technique to detect ICG or melanin. Before human imaging is possible, more studies need to be done to test the safety of PT-OCT imaging. First, melanin imaging in animal models using low photothermal laser power (<0.5mW as per ANSI guidelines) needs to be demonstrated. Tests would need to be performed in *ex vivo* human eyes since melanin concentration in the RPE can vary from one species to the next and melanin concentration has a direct effect on the PT-OCT signal. Measurements at different amplitude-modulation frequencies would also need to be tested since the shorter laser exposure times could lead to lower temperature increase and thus lower PT-OCT signal. Histological studies would need to be performed to look at short-term and long-term damage in eyes after PT-OCT imaging at different laser powers, beam size and exposure times[10]. For *in vivo* human imaging, a clinical system would have

to be modified to perform PT-OCT imaging. High acquisition speed and fast data processing should be prioritized when building such a system for effective clinical imaging in humans.

7.3 Contribution to the field and societal impact

Contribution to Biophotonics

This dissertation includes several contributions to the field of biophotonics including the first *in vivo* demonstration of PT-OCT in the eye. Previous PT-OCT studies have mostly been performed in phantoms, cells or in tissue *ex vivo*. Of the few studies performed *in vivo*, only one looked at passive accumulation of gold nanorods following a systemic injection, and this study was performed in a tumor xenograft mouse model[11]. In one of the studies presented in this dissertation (Chapter 4), PT-OCT signal from untargeted gold nanorods was detected *in vivo* in neovascular lesions in multiple mice eyes (n=7) after a systemic injection. A previous study from another group had used enhanced-backscattering OCT to detect gold nanorods in neovascular lesions of the eye but was not sensitive enough to distinguish the scattering gold nanorods against the scattering background of the neovascular lesion[12]. Our study was thus the first time gold nanorods were detected in a neovascular lesions of the eye using an OCT-based method.

Only one *in vivo* PT-OCT study had previously imaged melanin. In this study, a mole on the skin of a volunteer's arm was imaged and no depth-resolved structure was seen[13]. In two of the studies presented in this dissertation (Chapter 4 and 5), melanin located in the RPE was detected. First, melanin was detected in mice eyes (n=20 eyes across all experimental groups), then it was detected in zebrafish eyes (n=28 eyes across all experimental groups). In the zebrafish eye, a three-band structure was detected in the RPE and photoreceptor layers in all light-adapted zebrafish, while a single band located within the RPE was visible in all dark-adapted zebrafish. The distance between bands in the three-band structure was also constant across all light-adapted zebrafish. This type of structure had previously never been seen in PT-OCT images of melanin.

Two studies had previously detected indocyanine green using PT-OCT, but both of these studies used high photothermal laser power (70-80mW) and high concentrations of the dye (>0.5mg/cc)[14, 15]. Our study (Chapter 6) used photothermal laser powers down to 0.48mW, which is two orders of magnitude lower than previously done, and concentrations of ICG from 0.16mg/cc to 0.5mg/cc, which is lower than what is normally used in the clinic to stain the ILM. This is the first time PT-OCT was performed with laser powers under the ANSI guidelines (0.5mW)[16]. Additionally, the PT-OCT signal increases with depth, and we imaged the ILM which is only a few micrometers thick. Our sample was thus thinner than the phantoms[14] and lymphatic vessels[15] in which indocyanine green had previously been detected. With all three factors combined 1) the use of low concentrations of indocyanine green, 2) low photothermal laser powers and 3) imaging a thin structure, we have shown a significant improvement in the detection abilities of PT-OCT.

Finally, this dissertation includes a description of the PT-CLEAN algorithm (Chapter 3), which is the first correction algorithm for phase accumulation and shadowing that can be used for heterogenous samples and *in vivo* images. A study had previously taken the derivative of the PT-OCT signal as a function of depth to reduce phase accumulation and shadowing[1]. However, this method decreases the SNR of the resulting image, makes assumptions about the shape of the PT-OCT signal as a function of depth, and does not preserve the units of the PT-OCT signal. In comparison, the PT-CLEAN algorithm proposed in this dissertation preserves the units of change in optical path length and the SNR of the signal. It also does not require assumptions about the shape of the PT-OCT signal, the distribution of absorbers, or the composition of the sample. It is therefore appropriate for complex, heterogeneous samples, and was the first algorithm of its kind to be applied to *in vivo* PT-OCT B-scans. By reducing the effect of shadowing, the PT-CLEAN effectively improves the axial resolution of PT-OCT. The artifact correction algorithm also improves the usability of PT-OCT images. When imaging the ILM stained with indocyanine green in Chapter 6, the raw PT-OCT images showed signal starting at the ILM and a shadow covering the whole retina down to the RPE. Only with the application of the PT-CLEAN algorithm was it possible to recognize the ILM on PT-

OCT B-scans as the thin tissue layer seen on OCT B-scans or histology sections. The PT-CLEAN algorithm thus makes PT-OCT images easier to interpret and to compare to the structure seen on OCT B-scans.

Overall, this dissertation presents PT-OCT as a new molecular OCT technique that adds contrast to OCT using indocyanine green, gold nanoparticles, melanin or other optical absorbers. In the future, PT-OCT could be used similarly to polarization-sensitive OCT or optical coherence elastography to provide functional information that compliments the structural OCT images in living tissues.

Contributions to Ophthalmology

In this dissertation, PT-OCT was used to image the eye, which opens the door to future applications of this technique in eye and vision research. PT-OCT enables quantitative imaging of absorbers in the eye, a need which is not addressed by other standard eye imaging techniques such as fundus, SLO or OCT. Quantitative imaging of melanin could have applications in AMD[3], albinism[17], and retinitis pigmentosa[18] research and clinical care. For example, in dry AMD, hyperpigmentation is first seen in the RPE, probably because of a dysfunction of the RPE cells, followed by hypopigmentation due to RPE cell death[3]. It is thought that dysfunction in the RPE happens before dysfunction and death of the photoreceptors and could thus be predictive of disease progression[19, 20]. PT-OCT could thus be used at the pre-clinical level to better understand the role of the RPE in dry AMD and to quantify small changes in pigmentations over time. If changes in RPE pigmentations are found to be predictive of the progression of dry AMD, PT-OCT could potentially be used as an imaging tool to quantify pigmentation changes in patients and guide treatment.

PT-OCT has the advantage of producing images that are perfectly co-registered with OCT images. In this dissertation, bands of melanin were visible in the light-adapted zebrafish eye even though such as structure was not discernable on the corresponding OCT images (Chapter 5). A better understanding of the effect of melanin on the OCT signal could help disambiguate the OCT signal in the region surrounding the RPE[4, 21] and lead to a better identification of the different anatomical structures seen on OCT B-scans.

In the future, PT-OCT could be used in combination with histology in different animal models to inform how OCT images are interpreted, especially in diseases where the structure and the pigmentation of the RPE are affected. Eventually, PT-OCT could also be used for the same purpose in human subjects where histology cannot be performed.

PT-OCT enables *in vivo* detection of gold nanoparticles, which could enable longitudinal studies on gold nanoparticle pharmacokinetics and toxicity in the eye. Gold nanoparticles have been investigated as drug delivery vehicles and contrast agents in the eye[22]. However, little is known about accumulation, clearance and the effect of size, shape, and targeting[23]. As a result, gold nanoparticles have not yet been approved by the FDA for use in patients[24]. In this study, volumetric images showing the structure of the retina and distribution of gold nanoparticles in neovascular lesions were acquired (Chapter 4). PT-OCT is not destructive to the sample nor is it as labor intensive as other techniques such as instrumental neutron activation analysis (INAA) and inductively coupled plasma mass spectrometry (ICP-MS). PT-OCT could thus accelerate the translation of new gold nanoparticles from the laboratory to the clinic for eye applications.

Intraoperative OCT has now been integrated into surgical microscopes and surgical instruments to provide depth-resolved images during macular surgery. However, OCT is not sensitive to indocyanine green, a dye commonly used to increase the contrast of the ILM. Additionally, there are some concerns regarding the phototoxicity of indocyanine green at concentrations >0.6mg/cc[25, 26], which are commonly used in the clinic. In our study (Chapter 6), we demonstrate that PT-OCT is sensitive to concentrations of indocyanine green as low as 0.16mg/cc. Our data also demonstrate that the PT-OCT signal is specific to the ILM stained with indocyanine green, which could not be seen using only OCT. PT-OCT could thus be integrated into intraoperative OCT systems and enable lower concentrations of indocyanine green to be used during macular surgery, which could reduce the risks of phototoxicity during ILM peeling.

In summary, this dissertation presents PT-OCT as a novel tool for quantitative molecular eye imaging, which could have applications in studying diseases such as dry AMD, developing new treatments modalities such as gold nanoparticles, and performing surgeries such as ILM peeling.

7.4 References

[1] G. Guan, R. Reif, Z. Huang, and R. K. Wang, "Depth profiling of photothermal compound concentrations using phase sensitive optical coherence tomography," *Journal of biomedical optics,* vol. 16, no. 12, pp. 126003-1260039, 2011.

[2] D. Sen *et al.*, "High-resolution contrast-enhanced optical coherence tomography in mice retinae," *Journal of biomedical optics,* vol. 21, no. 6, pp. 066002-066002, 2016.

[3] I. Bhutto and G. Lutty, "Understanding age-related macular degeneration (AMD): relationships between the photoreceptor/retinal pigment epithelium/Bruch's membrane/choriocapillaris complex," *Molecular aspects of medicine,* vol. 33, no. 4, pp. 295-317, 2012.

[4] M. A. Wilk, A. L. Huckenpahler, R. F. Collery, B. A. Link, and J. Carroll, "The Effect of Retinal Melanin on Optical Coherence Tomography Images," *Translational Vision Science & Technology,* vol. 6, no. 2, pp. 8-8, 2017.

[5] A. Nahas, M. Varna, E. Fort, and A. C. Boccara, "Detection of plasmonic nanoparticles with full field-OCT: optical and photothermal detection," *Biomedical optics express,* vol. 5, no. 10, pp. 3541-3546, 2014.

[6] J. Barrick, A. Doblas, M. R. Gardner, P. R. Sears, L. E. Ostrowski, and A. L. Oldenburg, "High-speed and high-sensitivity parallel spectral-domain optical coherence tomography using a supercontinuum light source," *Optics letters,* vol. 41, no. 24, pp. 5620-5623, 2016.

[7] T. Wang *et al.*, "Thermo-elastic optical coherence tomography," *Optics letters,* vol. 42, no. 17, pp. 3466-3469, 2017.

[8] R. S. Jonnal, O. P. Kocaoglu, R. J. Zawadzki, S.-H. Lee, J. S. Werner, and D. T. Miller, "The cellular origins of the outer retinal bands in optical coherence tomography images," *Investigative ophthalmology & visual science,* vol. 55, no. 12, pp. 7904-7918, 2014.

[9] R. F. Spaide and C. A. Curcio, "Anatomical correlates to the bands seen in the outer retina by optical coherence tomography: literature review and model," *Retina,* vol. 31, no. 8, p. 1609, 2011.

[10] R. D. Glickman, "Phototoxicity to the retina: mechanisms of damage," *International Journal of Toxicology,* vol. 21, no. 6, pp. 473-490, 2002.

[11] J. M. Tucker-Schwartz, K. R. Beavers, W. W. Sit, A. T. Shah, C. L. Duvall, and M. C. Skala, "In vivo imaging of nanoparticle delivery and tumor microvasculature with multimodal optical coherence tomography," *Biomedical optics express,* vol. 5, no. 6, pp. 1731-1743, 2014.

[12] D. Sen *et al.*, "High-resolution contrast-enhanced optical coherence tomography in mice retinae," *Journal of biomedical optics,* vol. 21, no. 6, pp. 066002-066002, 2016.

[13] S. Makita and Y. Yasuno, "In vivo photothermal optical coherence tomography for non-invasive imaging of endogenous absorption agents," *Biomedical optics express,* vol. 6, no. 5, pp. 1707-1725, 2015.

[14] H. M. Subhash, H. Xie, J. W. Smith, and O. J. McCarty, "Optical detection of indocyanine green encapsulated biocompatible poly (lactic-co-glycolic) acid nanoparticles with photothermal optical coherence tomography," *Optics letters,* vol. 37, no. 5, pp. 981-983, 2012.

[15] J. M. Tucker-Schwartz, M. Lapierre-Landry, C. A. Patil, and M. C. Skala, "Photothermal optical lock-in optical coherence tomography for in vivo imaging," *Biomedical optics express,* vol. 6, no. 6, pp. 2268-2282, 2015.

[16] (2014). *American National Standards Institute for Safe Use of Lasers (ANSI/UL)*.
[17] C. G. Summers, "Albinism: classification, clinical characteristics, and recent findings," *Optometry and Vision Science,* vol. 86, no. 6, pp. 659-662, 2009.
[18] A. T. Fahim, S. P. Daiger, and R. G. Weleber, "Nonsyndromic retinitis pigmentosa overview," 2017.
[19] M. L. Klein *et al.*, "Retinal precursors and the development of geographic atrophy in age-related macular degeneration," *Ophthalmology,* vol. 115, no. 6, pp. 1026-1031, 2008.
[20] D. S. McLeod *et al.*, "Relationship between RPE and choriocapillaris in age-related macular degeneration," vol. 50, no. 10, pp. 4982-4991, 2009.
[21] Q.-X. Zhang, R.-W. Lu, J. D. Messinger, C. A. Curcio, V. Guarcello, and X.-C. Yao, "In vivo optical coherence tomography of light-driven melanosome translocation in retinal pigment epithelium," *Scientific reports,* vol. 3, 2013.
[22] Y. Diebold and M. Calonge, "Applications of nanoparticles in ophthalmology," *Progress in retinal and eye research,* vol. 29, no. 6, pp. 596-609, 2010.
[23] J. H. Kim, J. H. Kim, K. W. Kim, M. H. Kim, and Y. S. Yu, "Intravenously administered gold nanoparticles pass through the blood-retinal barrier depending on the particle size, and induce no retinal toxicity " *Nanotechnology,* vol. 20, no. 50, p. 505101, 2009.
[24] C. L. Ventola, "Progress in Nanomedicine: Approved and Investigational Nanodrugs," *Pharmacy and Therapeutics,* vol. 42, no. 12, p. 742, 2017.
[25] M. Murata, S. Shimizu, S. Horiuchi, and S. Sato, "The effect of indocyanine green on cultured retinal glial cells," *Retina,* vol. 25, no. 1, pp. 75-80, 2005.
[26] P. Saikia *et al.*, "Safety testing of indocyanine green in an ex vivo porcine retina model," *Investigative ophthalmology & visual science,* vol. 47, no. 11, pp. 4998-5003, 2006.